Self-assembly in colloidal hard-sphere systems

Cover: A cartoon of the self-assembly of a binary crystal.

PhD thesis, Utrecht University, the Netherlands, January 2011.
A digital version of this thesis is available at http://www.colloid.nl

Self-assembly in colloidal hard-sphere systems

Zelforganisatie in systemen van colloïdale harde bollen

(met een samenvatting in het Nederlands)

Proefschrift

ter verkrijging van de graad van doctor aan de Universiteit Utrecht op gezag van de rector magnificus, prof. dr. J.C. Stoof, ingevolge het besluit van het college voor promoties in het openbaar te verdedigen op maandag 31 januari 2011 des middags te 4.15 uur

door

Laura Christine Filion

geboren op 11 december 1979 te Sydney, Canada.

Promotor: Prof. dr. ir. M. Dijkstra

This research was supported by the High Potential Programme of Utrecht University.

... to my parents

Contents

1

Introduction

1.1 Colloids

Colloidal systems consist of small particles (colloids) of one substance suspended in another and are ubiquitous in everyday life. Many foods are examples of colloidal systems, including e.g. salad dressing, butter, and mayonnaise. Paints, toothpaste, and creams are other examples of colloidal systems. These systems can be composed of small solid particles suspended in a liquid or gas, for instance the fat droplets and protein clusters suspended in a water-like liquid which we call milk, or the solid particles suspended in air which we call smoke. A colloidal system can also consist of liquid droplets suspended in another liquid, such as oil droplets suspended in water or foams composed of a gas phase suspended in a liquid or solid. This leads to the question: what do these systems have in common? One answer to this question can be found by looking at the length scales: the small particles in a colloidal system typically have at least one dimension in the range of 1 nm to 1 μm. However, the underlying connection between colloidal systems is not so much related to the size of suspended particles, but rather to the dynamics of the colloids themselves: colloidal particles exhibit Brownian motion.

The observation of Brownian motion dates back to 1827 when Robert Brown noticed that pollen grains suspended in water appeared to move in random directions. Subsequently, in the early 20th century Albert Einstein and William Sutherland explained this behaviour as an interaction between the fluid molecules and the pollen grains [1, 2]. Fluid molecules themselves are in a constant state of motion due to thermal fluctuations. When a colloid is suspended in a fluid, it experiences collisions from the fluid molecules which results (at every instant in time) in a net force on the particle. The direction of this net force is random, and as a result, if the particle is sufficiently small it performs a random walk through the fluid, i.e. Brownian motion.

When a number of colloids are suspended in a fluid, in addition to interacting with the fluid, the colloids can also interact with each other. As a result, a colloidal system exhibits phase behaviour very similar to that of atomic systems. Specifically, the random motion of the colloidal particles, allows them to explore phase space and to self-assemble, leading to e.g. gas, liquid, solid, and glassy phases. This exploration of phase space and self-assembly is effectively a colloidal analogue to the phase behaviour seen in atomic and molecular systems.

The importance of this self-assembly is twofold. First, the self-assembly of colloidal particles opens up the possibility of designing advanced materials for various applications such as electro-optical devices [3–5]. These devices often make use of the fact that the lattice spacing in colloidal systems can be such that visible light is diffracted. (A natural example of this are the beautiful colours of gem opals which consist of a regular array of silica particles on a colloidal scale [6, 7].) Second, colloidal systems are ideal systems for modelling the behaviour in atomic and molecular systems. In contrast to their atomic and molecular counterparts, colloidal particles are typically large enough, and slow enough, to be observed via conventional optical techniques, such as light microscopy. Hence, dynamical processes such as nucleation which are very difficult to study in atomic and molecular systems can be addressed in colloidal systems.

1.2 Interactions

Recent advances in particle synthesis has yielded a huge variety of colloidal and nanoparticle building blocks [8]. In addition to spherical and rod-like particles, anisotropic particles which resemble cubes, pyramids, branched structures, and molecules have been synthesized. Additionally, new systems can be constructed by patterning the surface of such particles resulting in anisotropy of the particle-particle interactions. Furthermore, the self-assembly of the particles can be modified by changing the properties of the solvent; for instance, the addition of salt can screen charges on the colloids [9]. External fields such as electric fields can also be used to drive the system.

However, in this thesis we mainly restrict ourselves to colloidal systems which can be modelled simply by hard spheres. While this may seem like a huge simplification, there are a number of systems which are well modelled by hard spheres. In particular, a typical colloidal system consists of spherical silica or PMMA particles coated with a polymer brush. The effective interactions between the colloids in this system consist of a hard-core repulsion, a steric interaction associated with the polymer chains, Van der Waals forces, and electrostatic forces due to charges in the solvent or on the particles. To minimize the attractive Van der Waals forces which would drive the system to aggregate, in most experimental systems the colloids are suspended in a medium with a similar refractive index which minimizes the Van der Waals interactions. Additionally, the steric stabilizer (repulsion) on the surface helps to prevent the particles from getting close enough to each other for the Van der Waals forces to play an important role. The electrostatic forces can also be screened so that the resulting colloid-colloid electrostatic interaction is minimal. Hence, the resulting interaction between the particles can frequently be approximated as a hard-core interaction between the spherical cores of the particles.

1.3 Hard spheres

Most of this thesis examines properties of hard-sphere systems. In particular, we study the equilibrium phase behaviour and nucleation processes in such systems. Here we give an overview of the phase behaviour seen in monodisperse hard spheres and binary hard-sphere mixtures.

1.3.1 Monodisperse hard spheres

Monodisperse hard spheres are one of the simplest colloidal model systems. One of the theoretical advantages of studying the phase behaviour in systems which interact solely via a hard-core interaction is that temperature does not play a role and as a result the phase behaviour depends simply on the volume fraction of the system. Specifically, in a hard-core system the Boltzmann weight $\exp(-\beta U)$ is zero for all non-overlapping configurations and 1 otherwise, making T irrelevant.

It was more than 50 years ago that Wood and Jacobson [10], and Alder and Wainwright [11] demonstrated for the first time the fluid-to-crystal freezing transition in hard spheres. The freezing in this simple system is an example of an entropy driven phase transition. The freezing and melting packing fractions of this system were determined in 1968 by Hoover and Ree [12] to be $\eta_F = 0.494$ and $\eta_M = 0.545$. The stable solid phase turns out to be based on one of the close-packed structures for hard spheres, namely the face-centered-cubic lattice. The phase behaviour of this system was also examined experimentally. Pusey and Van Megen showed that suspensions of poly(methylmethacrylate) coated by thin brushes of a flexible polymer could act like hard spheres. Specifically, as a function of packing fraction, they found a fluid phase, a coexistence region between the fluid and solid, a solid region, and a glass region.

The nucleation rate for hard sphere has also been examined both via simulations, using umbrella sampling Monte Carlo techniques, and experimentally by light scattering. However, for low supersaturations, i.e. low volume fractions, the rates disagree. In this thesis we revisit this problem in Chapter 6.

1.3.2 Binary hard-sphere mixtures

Binary hard-sphere mixtures consist of mixtures of large and small hard spheres with diameters σ_L and σ_S respectively. Close-packed arrangements in such systems have long been studied as a model for atomic crystallization. In the 1960's, Parthé explained many atomic crystal structures using packing arguments [13]. On the colloidal side, Murray and Sanders observed binary crystal structures in naturally occurring gem opals and explained their results based on the close-packed structures [6, 7].

In this thesis we predict close-packed crystal structures for binary hard-sphere mixtures. See Chapters 2 and 4. Additionally, in Chapters 3 and 5 we examine the stable phase behaviour for binary hard-sphere mixtures for a variety of size ratios.

In Table 1.1 we give an overview of all the binary crystal structures which are predicted to be stable in the phase diagrams of binary hard-sphere mixtures obtained from full free-energy calculations for various size ratios $q = \sigma_S/\sigma_L$ [14–19]. We have highlighted in bold size ratios which are examined in this thesis.

1.4 Techniques

In this section we briefly discuss a number of different simulation techniques used throughout this thesis. In particular, we examine Monte Carlo simulations in the NVT and NPT

Size Ratio (q)	Stable Crystal Structures	Reference
0.033	FCC with disordered small	[14]
0.05	FCC with disordered small	[14]
0.1	FCC with disordered small	[14]
0.2	FCC with disordered small	[14]
0.3	interstitial solid solution and AB_6	Chapter 5
0.4	interstitial solid solution	Chapter 5
0.414	NaCl	[15]
0.42	interstitial solid solution	Chapter 5
0.45	NaCl and AlB_2	[15]
0.50	AlB_2	[16]
0.54	AlB_2 and ico-AB_{13}	[16]
0.58	AlB_2 and ico-AB_{13}	[16, 17]
0.59	AlB_2 and ico-AB_{13}	[16]
0.60	AlB_2 and ico-AB_{13}	[16]
0.61	AlB_2 and ico-AB_{13}	[16]
0.625	ico-AB_{13}	[16]
0.74	only FCC_L and FCC_S	Chapter 3
0.76	Laves Phases ($MgZn_2$, $MgCu_2$, $MgNi_2$)	Chapter 3
0.80	Laves Phases ($MgZn_2$, $MgCu_2$, $MgNi_2$)	Chapter 3
0.82	Laves Phases ($MgZn_2$, $MgCu_2$, $MgNi_2$)	Chapter 3
0.84	Laves Phases ($MgZn_2$, $MgCu_2$, $MgNi_2$)	Chapter 3
0.85	eutectic solid solution	[19]
0.875	eutectic solid solution	[19]
0.90	azeotropic	[19]
0.92	azeotropic	[19]
0.9425	azeotropic	[19]
0.95	FCC solid solution (spindle)	[19]

Table 1.1: A list of all the structures which have been shown to be stable in hard-sphere systems as a function of the size ratio q.

ensembles. We also describe a method to determine free energies, specifically, thermodynamic integration. Finally, we describe how to calculate the phase coexistences in binary mixtures.

1.5 Monte Carlo simulations

Monte Carlo simulations are used to sample phase space according to a Boltzmann weight, and hence are typically used to measure equilibrium properties of a system. In this chapter we restrict ourselves to applications of Monte Carlo simulations to colloidal systems.

In the NVT ensemble, the number of particles N, temperature T, and volume V are

kept fixed. The partition function for this system is given by

$$Q = C \int d\mathbf{p}^N d\mathbf{r}^N \exp\left(-\beta H(\mathbf{r}^N, \mathbf{p}^N)\right) \tag{1.1}$$

where $\mathbf{r}^N$ ($\mathbf{p}^N$) denotes the coordinates (momenta) of the N particles, $H(\mathbf{r}^N, \mathbf{p}^N)$ is the Hamiltonian, $\beta = k_B T$ with k_B Boltzmann's constant, and C is a normalization constant. The average value of a measurable A can then be determined by

$$\langle A \rangle = \frac{C \int d\mathbf{p}^N d\mathbf{r}^N A(\mathbf{r}^N, \mathbf{p}^N) \exp\left(-\beta H(\mathbf{r}^N, \mathbf{p}^N)\right)}{Q}. \tag{1.2}$$

If the measurable A depends only on the particle coordinates, this expression simplifies as the integrals over the momenta cancel. One is left with the expression

$$\langle A \rangle = \frac{\int d\mathbf{r}^N A(\mathbf{r}^N) \exp\left(-\beta U(\mathbf{r}^N)\right)}{\int d\mathbf{r}^N \exp\left(-\beta U(\mathbf{r}^N)\right)} \tag{1.3}$$

where $U(\mathbf{r}^N)$ is the potential energy. It turns out that direct evaluation of the integrals appearing in this expression is often impossible due to the huge number of configurations which would need to be evaluated. However, it is possible to determine $\langle A \rangle$ in an indirect manner, typically referred to as the Metropolis Method.

The Metropolis Method takes advantage of the fact that Eq. 1.3 is equivalent to a weighted average of $A(\mathbf{r}^N)$ according to a Boltzmann distribution. In particular, if we can generate random configurations according to the Boltzmann distribution, then

$$\langle A \rangle = \frac{1}{M} \sum_{k}^{M} A(\mathbf{r}_k^N) \tag{1.4}$$

where M is the number of random configurations and $\mathbf{r}_k^N$ denotes the particle coordinates associated with configuration k. Hence, the Metropolis method simply presents a way in which states can be selected according to their Boltzmann weight.

In practice, for a simple colloidal system this can be accomplished as follows. A simulation is started where N particles are placed in a box of volume V at temperature T. A random particle is chosen and a new (trial) position for this particle is found by adding a random vector $\Delta\mathbf{r}$ to the particle's current position. The potential energy difference between the old configuration and the new configuration is given by $\Delta U = U(\mathbf{r}_i + \Delta\mathbf{r}, \{r_{j\neq i}\}) - U(\{\mathbf{r}_i\})$. This new particle position is accepted using the following acceptance rule: if $\Delta U < 0$ then the new position is accepted, and if $\Delta U > 0$ then the new position is accepted with the probability $\exp(-\beta\Delta U)$. The set of configurations generated in this manner are consistent with the Boltzmann distribution.

Similarly, we can use the Metropolis algorithm to determine average measurables in the NPT ensemble. In this case, in addition to trial particle displacements, trial changes of the volume are also necessary. The trial particle moves obey the same acceptance rule as in the NVT ensemble. The trial volume moves from a volume V_{old} to V_{new} are accepted according to the following rule: if we set $\zeta = (-\beta\Delta U + \beta P(V_{\text{new}} - V_{\text{old}}) - N \ln V_{\text{new}}/V_{\text{old}})$ then when $\zeta < 0$ the new volume is accepted, and when $\zeta > 0$ then the new volume is accepted with the probability $\exp\zeta$.

NVT and NPT are two of the most frequently used ensembles for studying colloidal systems, however algorithms also exist for the grand canonical ensemble, the Gibbs ensemble, and many others. For a full description of the Monte Carlo method, details regarding the application of the technique in a variety of systems, and tricks for implementing the algorithms, see Ref. [20].

1.6 Free-energy calculations

In many chapters in this thesis, free-energy calculations are used in combination with common tangent constructions to determine phase diagrams. In this section we give an overview of some of the more common methods associated with these calculations.

1.6.1 Thermodynamic integration

The Helmholtz free energy of a system of N particles in a volume V is given by

$$F = U - TS \tag{1.5}$$

where F is the Helmholtz free energy, U is the potential energy, T is the temperature and S is the entropy.

One method of calculating the exact free energy for a general system, such as hard-sphere mixtures, is thermodynamic integration. In this case, it is assumed that there exists a reference system for which we can calculate the free energy analytically. For example, for liquids often the ideal gas is used and for crystals, the Einstein crystal [21] can serve as the reference system. If the potential energy of the reference system is given by U_R and the potential energy of our true system of interest is denoted U_T then it is possible to define a new (fictitious) potential energy

$$U(\lambda) = (1-\lambda)U_T + \lambda U_R, \tag{1.6}$$

which is now a function of a coupling parameter λ, which varies between 0 and 1. Note that this function has the property that when $\lambda = 0$ it reduces to our system of interest, and when $\lambda = 1$ it reduces to the reference system. The free-energy difference between the reference and the system of interest can be determined exactly, see Ref. [20], and is given by

$$F(\lambda=1) - F(\lambda=0) = \int_{\lambda=0}^{\lambda=1} d\lambda \left\langle \frac{\partial U(\lambda)}{\partial \lambda} \right\rangle_\lambda . \tag{1.7}$$

Thus, to calculate the free energy exactly we simply need to determine $\langle \partial U(\lambda)/\partial\lambda \rangle_\lambda$ as a function of λ. Such an average can be determined using a Monte Carlo simulation. After the Helmholtz free energy is known, all other relevant thermodynamic quantities (such as the Gibbs free energy) can then be obtained.

Moreover, once the free energy is known for one state point, using Maxwell's relation we have

$$\left(\frac{\partial F/N}{\partial \rho}\right) = \frac{P(\rho)}{\rho^2} \tag{1.8}$$

and we can show that

$$\frac{\beta F}{N}(\rho) = \frac{\beta F(\rho_0)}{N} + \beta \int_{\rho'=\rho_0}^{\rho} d\rho' \frac{P(\rho')}{\rho^2}. \tag{1.9}$$

An additional Monte Carlo simulation (NPT) can be used to determine the equation of state $P(\rho)$, and then the free energy is known for all ρ.

1.6.2 Common tangent constructions in a binary mixture

The coexistence regions in binary mixtures are typically calculated using so called "common tangent" constructions. In the following we quickly demonstrate the theoretical basis for this method. This derivation follows closely the derivation presented in Ref. [22]

Assume that we have a two component mixture (such as a binary mixture of colloids or nanoparticles) and that we have $N_{1(2)}$ particles of type 1(2), which can be in two phases, α and β. The conditions for thermodynamic equilibrium for the two phases requires that the temperature, pressure and the chemical potentials for the two species must be equal in both phases. Specifically,

$$p(\rho_1^\alpha, \rho_2^\alpha, T) = p(\rho_1^\beta, \rho_2^\beta, T), \tag{1.10}$$
$$\mu_1(\rho_1^\alpha, \rho_2^\alpha, T) = \mu_1(\rho_1^\beta, \rho_2^\beta, T), \tag{1.11}$$
$$\mu_2(\rho_1^\alpha, \rho_2^\alpha, T) = \mu_2(\rho_1^\beta, \rho_2^\beta, T), \tag{1.12}$$

where $\rho_{1(2)}$ is the density of species 1(2), p is the pressure, T is the temperature and $\mu_{1(2)}$ is the chemical potential of species 1(2).

The Gibbs free energy is an extensive variable and so it scales with the total number of particles in the system (N) as

$$G(N_1, N_2, p, T) = N g(x, p, T) \tag{1.13}$$

where $g(x, p, T)$ is the Gibbs free energy per particle, and $x = N_1/N$. Since the chemical potentials are related to the Gibbs free energy by

$$\mu_{1(2)}(x) = \left(\frac{\partial G}{\partial N_{1(2)}} \right)_{N_{2(1)}, P, T} \tag{1.14}$$

they can be written

$$\mu_1(x) = g(x) + (1 - x) g'(x) \tag{1.15}$$
$$\mu_2(x) = g(x) - x g'(x). \tag{1.16}$$

Applying the chemical equilibrium relations expressed in Eqns 1.11 and 1.12, we obtain

$$g'(x^\alpha) = g'(x^\beta) \tag{1.17}$$
$$g'(x^\alpha) = \frac{g(x^\alpha) - g(x^\beta)}{x^\alpha - x^\beta}. \tag{1.18}$$

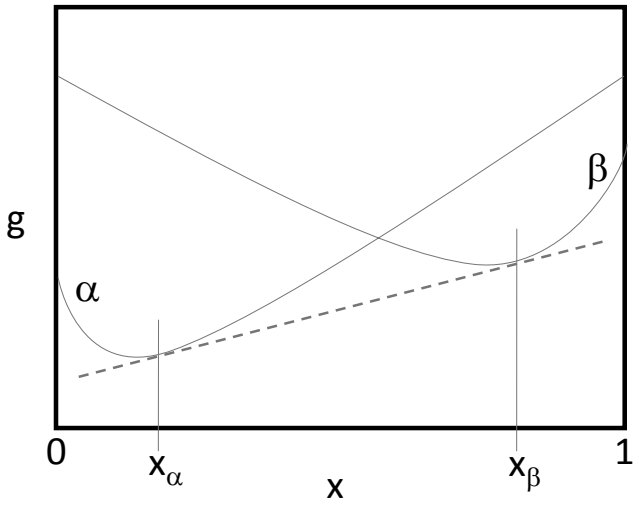

Figure 1.1: A cartoon of a common tangent construction between two phases α and β. The label x_α and x_β denote the boundaries of the coexistence region. For $x < x_\alpha$ the α phase is stable, for $x_\alpha < x < x_\beta$ there is a coexistence between the α and β phases, and for $x > x_\beta$ the β phase is stable.

Summarizing, phase coexistence happens when, for some x^α and x^β the slopes of the Gibbs free energy per particle for both phases (at constant temperature and pressure) are equal, *and* the lines tangential to the free energy through both these points have the same "y" intercept.

Another way to think about the common tangent construction is that the system as a whole always tries to minimize the total free energy. Thus, for a given composition x, the system will choose a linear combination of phases α and β such that the total Gibbs free energy is minimized. Graphically, such a minimum corresponds to a common tangent construction. A cartoon of a common tangent construction is shown in Figure 1.1.

1.7 Thesis outline

The work in this thesis can be roughly grouped into three sections. In Chapters 2 and 4 we examine the prediction of candidate crystal structures for use in predicting the phase behaviour. In Chapters 3 and 5 we examine the phase behaviour of a range of binary hard-sphere mixtures. Finally, in Chapters 6 and 8 we examine the crystal nucleation of hard and almost hard systems.

2

Prediction of binary hard-sphere crystal structures

We present a method based on a combination of a genetic algorithm (GA) and MC simulations to predict close-packed crystal structures in hard-core systems. We employ this method to predict the binary crystal structures in a mixture of large and small hard spheres with various stoichiometries and diameter ratios between 0.4 and 0.84. In addition to known binary hard-sphere crystal structures similar to NaCl and AlB_2, we predict additional crystal structures with the symmetry of CrB, γCuTi, αIrV, $HgBr_2$, $AuTe_2$, Ag_2Se and various structures for which an atomic analogue was not found. In order to determine the crystal structures at infinite pressures, we calculate the maximum packing density as a function of size ratio for the crystal structures predicted by our GA using a simulated annealing approach.

2.1 Introduction

Close packed arrangements of hard spheres have been of interest for centuries both as theoretical challenges as well as models for various physical systems. However, the question of which structures pack best relies heavily on physical intuition and experimental results. In the case of identical hard spheres, Kepler's 17th century conjecture that the densest arrangement was achieved by stacking close-packed hexagonal planes remained one of the major mathematical challenges until 1998 when Hales presented what appears to be almost a complete proof [23]. However, the prediction of close packed structures of mixtures of various sized hard spheres is even more challenging due to the enormous size and complexity of the phase space that must be searched to locate the best packed arrangements. In this chapter we use a combination of a genetic algorithm (GA) and Monte Carlo (MC) simulations to search for such crystal structures, attempting to remove much of the (ad hoc) guess work associated with predicting the crystal structures realized by such systems. By finding the close-packed arrangements, our algorithm predicts crystal structures that are stable at infinite pressures and additionally produces candidate crystal structures for the phase behavior at lower pressures. While most of the structures found for $R_S/R_L < 0.6$ (where R_S (R_L) is the radius of the small (large) hard spheres), such as NaCl and AlB_2, have already been discussed in the literature, many of the structures for larger size ratios are novel in the context of the phase behavior of binary hard-sphere mixtures.

The close-packed structures of binary hard-sphere mixtures have been studied intensively as a model for atomic and colloidal systems. In the 1960's Parthé [13] used the concept of packing to explain binary atomic crystal structures found in nature and in 1980 Murray and Sanders argued that binary mixtures of hard spheres order into the structure with the largest possible packing fraction under sedimentation and compaction to explain the long-range crystal structures observed in gem opals. [6] More recently, packing arguments have also been used to explain the experimental observations of intriguing and complicated superlattice structures in binary mixtures of nanoparticles [24, 25], of colloidal particles [26–30], and of block copolymer micelles [31]. The underlying idea of these packing arguments is that structures that have a higher close-packed density, will have a larger free volume per particle at lower densities, resulting in a higher contribution to the entropy and hence a lower free energy. In studies of self-assembled nanoparticles where non-close-packed crystalline structures are observed it is often asserted that other interactions must play a role [25].

Genetic algorithms, developed first by Holland [32] in the 1970s, provide a framework for finding the optimal solution of a specific problem by mimicking Darwin's principle of "survival of the fittest" by means of natural selection. GAs enable us to sample efficiently large search spaces in an unbiased and unrestricted way. A basic quantity in a GA [32] is an individual that represents a trial solution to the problem which can be ranked according to a fitness function (e.g. the potential energy). From a random initial population of individuals, the system evolves from generation to generation by using cross-over and mutation operators until the population converges to a solution. Originally GAs were designed to search a finite phase space and used a discrete genetic representation of the individuals [32]. Since the 1980s "hybrid" GAs have been widely used to search continuous

phase spaces. Such algorithms exploit the advantages of both GAs and local minimizers: a fast local minimization technique is used to relax an individual to its local minimum and mutations and crossovers are employed in the GA to hop between local minima. In this manner continuous parameters, such as the primitive and basis vectors that describe a crystal structure, can be varied to minimize the respective fitness function.

Genetic algorithms were introduced to atomic and molecular systems in the 1990's in an attempt to determine the lowest energy structure of an atomic cluster [33–35]. Although the first such algorithms involved traditional discrete GA's [33, 34], the most commonly used ones are based on a hybrid GA introduced by Deaven and Ho [35]. In their GA the genetic code consists of the atomic positions, and crossovers are performed by cutting clusters with a plane in real space; the complementary partial spaces are recombined from parent clusters and the resulting structures relaxed to their local minimum with a conjugate gradient algorithm. Variations of this technique have since been used to study many clusters, however, the use of GAs to study periodic systems such as colloidal and atomic systems is much more recent and employ either a lattice and basis representation of the crystal structure [36, 37], a discrete binary representation of these vectors [38], or a so-called "hydra" representation based on displacement vectors [39]. A cartoon of the hydra representation is depicted in Figure 2.1 . This last implementation has been applied to a system with approximately hard interactions. The inclusion of hard interactions in a GA complicates the problem severely as most cross-over and mutation operations cause overlaps between the particles. Many forbidden regions are present in the search space that should be circumvented. In this chapter, we use a modification of the GA based on the hydra representation to search for close-packed structures in binary hard-sphere systems.

This chapter is organized in the following manner. In section 2.2 we describe the method we used to determine the binary crystal structures, including a description of the GA. In section 2.3 we present a table with the structures we have found along with space filling curves for the best packed structures with AB and AB_2 stoichiometry. Finally, in section 2.4 we discuss the results and our conclusions.

2.2 Method

In this chapter we employ a combination of a GA and Monte Carlo simulations to maximize the packing fraction of a binary crystal structure for a given stoichiometry and particle radius ratio $q = R_S/R_L$. The GA we use is based on the algorithm introduced by Stucke and Crespi [39] to examine ternary hard-sphere systems. As the packing fraction depends only on the volume of the unit cell and not on the basis vectors, the algorithm will encounter severe convergence problems if the packing fraction is used as the fitness function. Hence, the packing fraction is not a suitable fitness function for a hybrid GA. The method proposed by Stucke and Crespi attempts to avoid this problem by minimizing a fictitious potential. We follow a similar route here but extend the approach as follows: we first use a GA to locate the potential minima of a fictitious potential, and subsequently we replace the fictitious potential with a true hard-sphere interaction, expand the unit cell until any resulting overlaps are removed, and then use a Monte Carlo pressure annealing

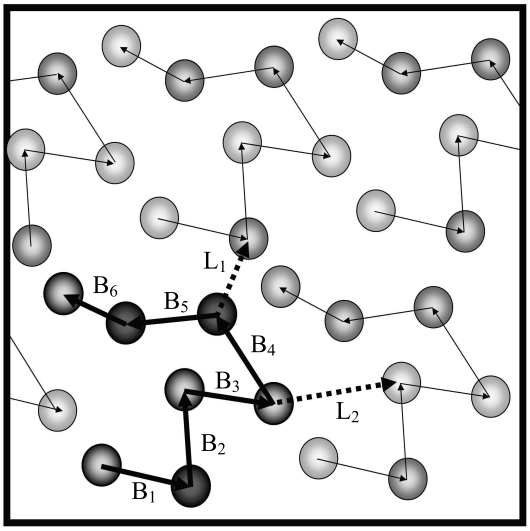

Figure 2.1: A typical 2D "hydra" for a binary system with 7 particles in the unit cell: 3 of type A (darker spheres) and 4 of type B (lighter spheres). (Colour Online)

simulation to crush the resulting structure to the best packing. The structure is then identified either by visual inspection, or with the FINDSYM program [40].

2.2.1 Genetic algorithm

An "individual" in our GA is a system representation for a crystal structure. As mentioned in the introduction, we have chosen to represent crystal structures using a displacement vector representation, called the "hydra" representation [39]. A cartoon illustrating the "hydra" representation is shown in Figure 2.1. In our version of the "hydra" representation the genetic code consists of two sequences, one for the basis particles and one for the periodic lattice. In d dimensions with N distinguishable particles per unit cell, the first sequence consists of the displacement vectors between particles and is given by the hydra $\mathbf{B} = \mathbf{B}_1, \mathbf{B}_2, \cdots, \mathbf{B}_{N-1}$. The vector $\mathbf{B}_i$ connects particle i to $i+1$ in this representation. In the hydra representation the particles connected by the displacement vectors are generally not in the same unit cell, however, there is exactly one image of each particle in the hydra. The second sequence contains the lattice vectors of the hydra $\mathbf{L} = \mathbf{L}_1, \cdots, \mathbf{L}_d$, which denote the projections to periodic images of the hydra. We note that $\mathbf{L}_i$ can interconnect a particle with its image, but it can also interconnect distinct particles in the hydra. The particles that are interconnected by the lattice vectors $\mathbf{L}_i$ are selected at the beginning of the GA. To initialize a hydra, the displacement vectors $\mathbf{B}_i$ are chosen according to a Gaussian distribution peaked at 1.2 $(R_i + R_{i+1})$, where R_i denotes the radius of particle i. The angular orientation is then chosen at random. The lattice vectors $\mathbf{L}_i$ are chosen in the same manner. We start our GA with a random initial population of hydras.

In theory, we would like to use the packing fraction as a fitness function, but in that case the GA experiences convergence problems as the packing fraction is independent of the particle positions in the cell. Instead, we replace the hard-sphere interaction by the

following pair potential:

$$V(r_{ij}) = \epsilon_{ij} \left(\frac{\sigma_{ij}}{r_{ij}} \right)^m - \left(\frac{\sigma_{ij}}{r_{ij}} \right)^n \tag{2.1}$$

where r_{ij} is the interparticle distance between particles i and j. The fitness function is then the sum of these pairwise interactions. As this is now a continuous function of all lattice parameters, the local minima can easily be determined using a conjugant gradient method. In our implementation of the algorithm, we have typically chosen $m = 42$ and $n = 24$ in the pair-wise potential, however, we have checked for various stoichiometries and size ratios that other values of n result in the same crystal structures implying that our results are robust with respect to the fictitious attractive tail.

The genetic algorithm starts with a population of M members. To search space more efficiently, each hydra is relaxed to its local minimum using the Broyden-Fletcher-Goldfarb-Shanno (BFGS) algorithm [41]. In the hydra representation, the potential energy calculation can be computationally expensive as it is possible that several images must be summed over before all the interactions within the cutoff radius of a single hydra are included. For instance, it is possible that some of the nearest neighbours of a particle in a given hydra are several lattice vectors away. In a Bravais representation, however, it is possible to determine in advance the number of cells along each lattice vector that are needed to calculate the potential energy of a crystal structure. It is thus advantageous to map the hydra to a Bravais representation before relaxing the structure. For this purpose the Bravais lattice vectors are constructed from the $\mathbf{L}$ vectors and a lattice reduction algorithm is used to produce a more cubic unit cell. In 2D we use the well known Gaussian reduction algorithm while in 3D we use the lattice reduction method described in Ref. [38]. The 3D method attempts to minimize the surface area of the unit cell. Denoting the lattice vectors $\mathbf{r}_1, \mathbf{r}_2$ and $\mathbf{r}_3$ and the surface area of the box spanned by the vectors A, the 12 linear combinations

$$\mathbf{r}_i^{\text{new}} = \mathbf{r}_i \pm \mathbf{r}_l, \tag{2.2}$$

with $i \neq l \in \{1, 2, 3\}$, are determined and the surface areas $A_{i,l}^{\text{new}}$ of the new boxes spanned by $\mathbf{r}_i^{\text{new}}$, $\mathbf{r}_j$ and $\mathbf{r}_k$ are compared to A. If any of the $A_{i,l}^{\text{new}}$ is smaller than A then the corresponding $\mathbf{r}_i$ is set to $\mathbf{r}_i^{\text{new}}$, otherwise the algorithm terminates. A single hydra is then mapped to the resulting unit cell and relaxed to its local minima. The hydra representation is then reconstructed in the following manner: the $\mathbf{B}_i$'s are found by taking the shortest vector between any image of particle i and $i+1$ and the $\mathbf{L}_i$'s are constructed similarly. The mapping between the hydra and Bravais representations is one of the main differences between our algorithm and the one in Ref. [39] where the potential energy is calculated by summing *all* the interactions between W^d hydras with d the dimensionality. Our mapping between the hydra and Bravais representations serves two purposes. First, for the energy calculation the number of cells which need to be summed over is less than or equal to the W^d boxes summed in Ref. [39], and hence significantly faster. Secondly, neighbours in the hydra representation remain close in real space. This increases the speed of the local minimization and prevents displacement vectors from becoming exceedingly long. Additionally, according to the building block hypothesis for GAs, having the most related parameters close in the system representation improves the GA convergence [42].

A new generation consists of S offspring produced by mutations and cross-overs. To

produce an offspring, two parents are selected at random (denoted p_1 and p_2) from the current generation. Each displacement vector in the corresponding **B**'s undergo a random mutation in its length with a probability of 10%. The first step in the cross-over is to randomly choose a k_1 between 0 and d. The first k_1 vectors of the sequence L are then taken from p_1 and the remaining from p_2. The new lattice vectors are tested to make sure that they are not co-linear. If they are then a new k_1 is chosen. Next, a random cross-over point k_2 is chosen between 1 and $N-2$. The first k_2 elements of the sequence **B** are then taken from p_1 and the rest from p_2. The two partial hydra are then rotated in real space around the connection point until a minimum in the potential energy is found. The structure is then relaxed to its local minimum as previously described. For the candidate structure to become a member of the offsping it must still meet three additional requirements: that (i) the bond lengths are less than some maximum value r_{max}, that (ii) its fitness is better that the worst of the previous generation and that (iii) its normalized dot product with the members of the current generation and any other current offspring is less than 0.8. The latter requirement is needed to prevent the offspring from being located in the same local minima as the other members, and allows us to work with a rather small population. However, if the normalized dot product between the potential offspring and a single member is greater than 0.80 and if the fitness is better it replaces the other. The bond length restriction is used to select out a specific set of solutions. For instance, for large R_S/R_L ratios, the best packed solution is always phase separated hexagonal close-packed structures of small and large hard spheres. However, by restricting the bond lengths, we are able to exclude this possibility and force the simulation to find the next best solution. Since we are interested in binary hard-sphere crystal structures, this is an essential component of the algorithm. It should be noted, however, that this restriction is only important for larger unit cells (with $\approx$8 or more colloids per unit cell). When S children are produced in this way, the next generation is produced by a form of elitism where the best M members of the parents and offspring are taken. The algorithm terminates when all the members of the population have the same energy (within δE) for 10-20 generations. In the majority of our simulations we used $M = 20$ and $S = 10$. If either M or S are much larger, then the normalized dot product restriction is rarely met and many candidate structures are thrown out. In summary, our modifications to the GA, which improved significantly the speed and convergence of the algorithm, allowed us to systematically predict candidate crystal structures for a large range of size ratios and stoichiometries and to locate binary crystal structures even when monodisperse (rHCP) crystal structures pack better.

2.2.2 Monte Carlo pressure annealing

The GA in the previous section minimizes a fictitious potential. Replacing the fictitious pair potential from the previous algorithm with a hard-sphere potential often results in either slight overlaps of the particles or holes in the structure. Thus, in order to find the true, hard-sphere packing fraction of the resulting structure, an additional method is needed. To solve this problem we employ a form of MC pressure annealing. The "hydra" representation is first mapped to it's corresponding Bravais lattice. The resulting lattice vectors are used as the simulation box. In this MC simulation, a typical metropolis

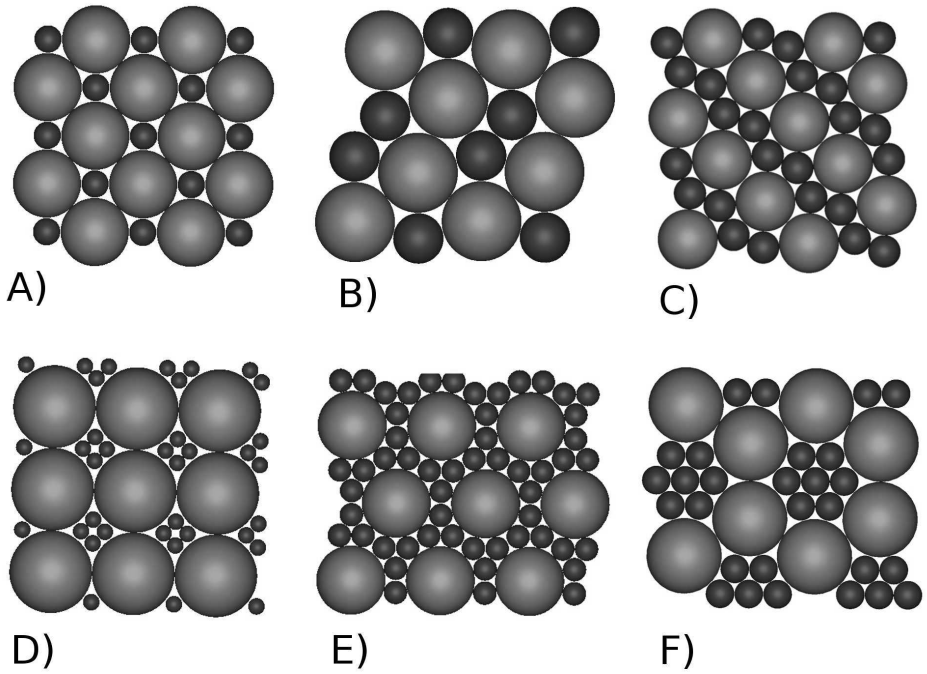

Figure 2.2: 2D crystal structures predicted using the GA. The naming convention for the crystal structures is consistent with Ref. [43]. A) crystal structure S_1: AB stoichiometry with $q = 0.4$, B) H_2: AB, $q = 0.63$, C) H_1: AB_2, $q = 0.54$, D) S_2: AB_4, $q = 0.2$, E) T_2: AB_6, $q = 0.34$, F) H_3: A_2B_7, $q = 0.38$. (Colour online)

algorithm is used to move particles in a unit cell, while volume moves allow both the size and the shape of the simulation box to vary. An initial pressure is chosen such that the crystal structure cannot melt and the pressure is slowly increased until the particles can no longer move (to single precision accuracy). This pressure is higher for particles with small R_S/R_L values as they melt at lower pressures. The resulting structure is then identified either by inspection, or with the FINDSYM program [40].

2.3 Method verification and results

To test the algorithm we have examined various systems of hard disks and hard spheres. In 2D monodisperse systems we found hexagonal lattices and in 3D the GA converges to crystal structures consisting of stacked hexagonal planes in face-centered-cubic (FCC), hexagonal-close-packed (HCP) and rHCP arrangements as conjectured by Kepler. In all cases the GA converged to several different hydra representations of the same crystal structures suggesting that the potential minimum was indeed found. We also examined 2D binary systems with AB, AB_2, AB_4, AB_6, and A_2B_7 stoichiometries for various size ratios, a system examined previously by Likos and Henley [43]. Our results are shown in Figure 2.2 and agree with their predictions. It should be noted that we did not do an extensive search of the phase space, but rather used this as a check of the algorithm. The stoichiometries we checked were chosen to be representative of their results. However, it is

q	0.4	0.5	0.6	0.7
AB	NaCl/NiAs	CrB	CrB	CrB
	0.788	0.749	0.745	0.722
AB_2	-	$AuTe_2$	AlB_2	S 74h/e
		0.756	0.757	0.718
AB_3	S 5b/ac	S 19b/1f	S 12 c/ib	S 8a/aaa
	0.722	0.744	0.721	0.672
AB_4	S 1a/aaaa	S 160a/ab	S 123d/fg	S 38b/de
	0.738	0.725	0.737	0.666
AB_5	-	S 8a/abb	S 8a/bba	S 183a/bc
		0.690	0.713	0.690
AB_6	S 10d/gj	S 83c/gk	S 38a/dee	S 69b/ij
	0.756	0.710	0.729	0.680
q	0.72	0.74	0.76	0.78
AB	CsCl	CsCl	CrB	CrB
	0.719	0.726	0.719	0.718
AB_2	SG 74h/e	SG 74h/e	SG 74h/e	$AuTe_2/HgBr_2$
	0.719	0.715	0.704	0.714
AB_3	S 12d/ai	S 12d/ai	S 12c/ib	S 6b/aab
	0.672	0.670	0.669	0.684
AB_4	S 65b/ij	S 65d/ij	S 65d/gh	S 65c/gh
	0.664	0.655	0.647	0.640
AB_5	S 183a/bc	S 183a/bc	S 160a/aab	S 189a/cg
	0.688	0.686	0.674	0.684
q	0.8	0.82	0.84	
AB	γCuTi	αIrV	αIrV	
	0.721	0.722	0.729	
AB_2	$AuTe_2$	Ag_2Se*	$AuTe_2$	
	0.714	0.7204	0.707	
AB_3	S 123b/ah	S 12d/ai	S 47b/al	
	0.694	0.672	0.700	
AB_4	-	S 87b/h	S 87b/h	
	0.698	0.705	0.704	
AB_5	S 189a/cg	S 183 b/df	S 8 a/abb	
	0.688	0.686	0.667	
AB_6	S 139b/ge	S 2	S 12a/iii	
	0.658	0.674	0.695	

Table 2.1: Binary crystal structures with the largest packing fraction predicted for various q ratios for AB (4), AB_2 (6), AB_3 (4), AB_4 (5), AB_5 (6) and AB_6 (7) stoichiometries where the number in () refers to the number of colloids per unit cell studied. * was calculated with 12 colloids per unit cell and in addition to Ag_2Se another structure was found, which is a distortion of the $MgZn_2$ Laves phase, but with extremely low symmetry and a packing of 0.716.

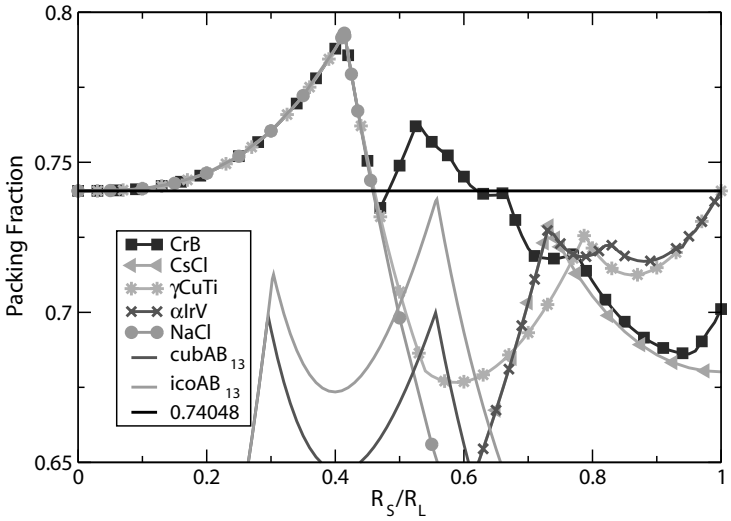

Figure 2.3: Space filling curves for the AB structures listed in Table 2.1 as well as icosahedral and cuboctahedral AB_{13}. Only a fraction of the data points were plotted to simplify the image. (Colour online)

still possible that a more thorough study of the binary hard disk system would yield new structures. Additionally, unlike the algorithm we used, the method of Likos and Henley involved systematically filling holes in the lattice of typical monodisperse 2D lattices with smaller particles and allowing the crystalline structures to distort in a manner that resulted in best packings for the given size ratio and stoichiometry. However, unlike our search, the method used by Likos and Henley [43] relied on preselected structures for their searches while the GA implementation used here searches all possible binary crystals with the only restriction being the number of particles per unit cell.

Additionally, we studied binary mixtures in 3D with AB, AB_2, AB_3, AB_4, AB_5, and AB_6 stoichiometries for various size ratios *. The structure with the densest packing fraction had either AB or AB_2 stoichiometry for any given size ratio. Our results for all stoichiometries are summarized in Table 2.1.

The crystal structures are identified by an atomic analogue of the binary structure which has the same space group and Wyckoff positions. For instance, $AuTe_2$ refers to a structure which has the symmetry associated with space group 12 when the 2a Wyckoff positions are occupied by the larger particles and the 4i positions are occupied by the smaller particles, this leaves 6 degrees of freedom for the structure (a, b, c, β, x, z). Hence, structures which have been identified as $AuTe_2$ may have different lattice parameters. When no atomic analogue was found the structures were listed by their space group and occupied Wyckoff positions.

In order to determine the best-packed crystal structures for a given size ratio, we calculate the space filling curves for all the AB and AB_2 structures predicted by our

*Since the first submission of this work, a paper predicting 3D binary hard-sphere crystal structures with AB stoichiometries has been published [44]. We have compared our results for 3D AB stoichiometries with this paper and found agreement. Ref. [44] examined the packing of known inorganic binary crystalline structures using a simulated annealing approach.

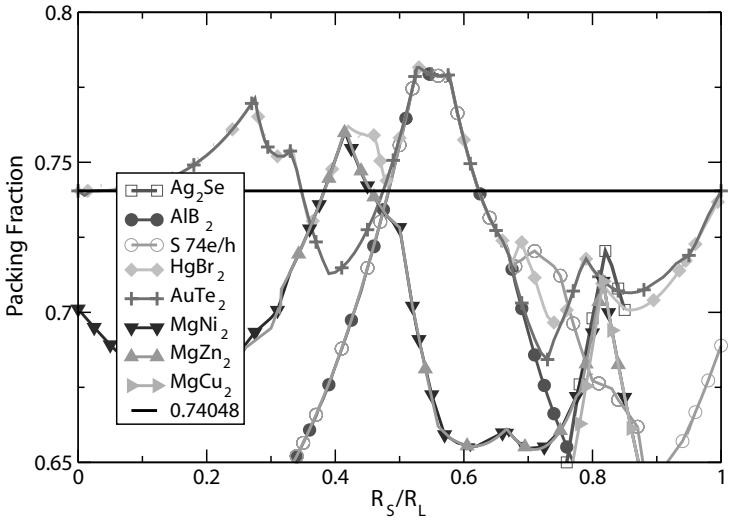

Figure 2.4: Space filling curves for the AB_2 structures listed in Table 2.1 along with the curves for the Laves structures ($MgCu_2$, $MgZn_2$ and $MgNi_2$). (Colour online)

GA. To this end, we maximize, for a given structure and size ratio, the packing fraction as a function of the lattice parameters using a simulated annealing algorithm. Since the number of free parameters describing a given structure is typically small, it is often possible to maximize the packing fraction for the hard-sphere potential[†]. The space filling curves of the AB and AB_2 structures listed in Table 2.1 are shown in Figures 2.3 and 2.4 and cartoons depicting the associated crystal structures are shown in Figures 2.5 and 2.6. For comparison with our results, we have also included the space filling curves of the Laves phases in Figure 2.4 as well as the cuboctahedral (cub) and icosahedral (ico) AB_{13} in Figure 2.3. In the case of the AB_{13} structures, the only parameter varied was the overall lattice scaling.

2.4 Discussion and conclusions

From the packing fraction curves it is possible to predict the infinite pressure phase diagrams since, for a given size ratio q, the structure with the largest packing fraction is stable at infinite pressures. Hence we predict NaCl/NiAs ($0 < q \leq 0.44$), $HgBr_2$ (0.44 - 0.48), $AuTe_2$ (0.48 - 0.53), and AlB_2 (0.53-0.62). For size ratios larger than 0.62 monodisperse FCC, HCP and rHCP have the largest packing.

In contrast, at finite pressures, it is necessary to compare the Gibbs free energies to determine the stability of a phase. Such analyses on binary hard-sphere systems have included NaCl (stable for $0.3 < q < 0.45$), AlB_2 (0.45 - 0.61), icoAB_{13} (0.54 - 0.62), CsCl (no known stable region), and the Laves phases (0.76 - 0.84) [15, 17, 45–47]. Many of

[†]In the case of Ag_2Se however, the structure has 12 internal parameters and the simulated annealing approach only worked when a good initial guess was known. Hence, near $q = 0.82$ we were able to use the structure predicted by the GA, but we were unable to determine the packing for the full set of size ratios.

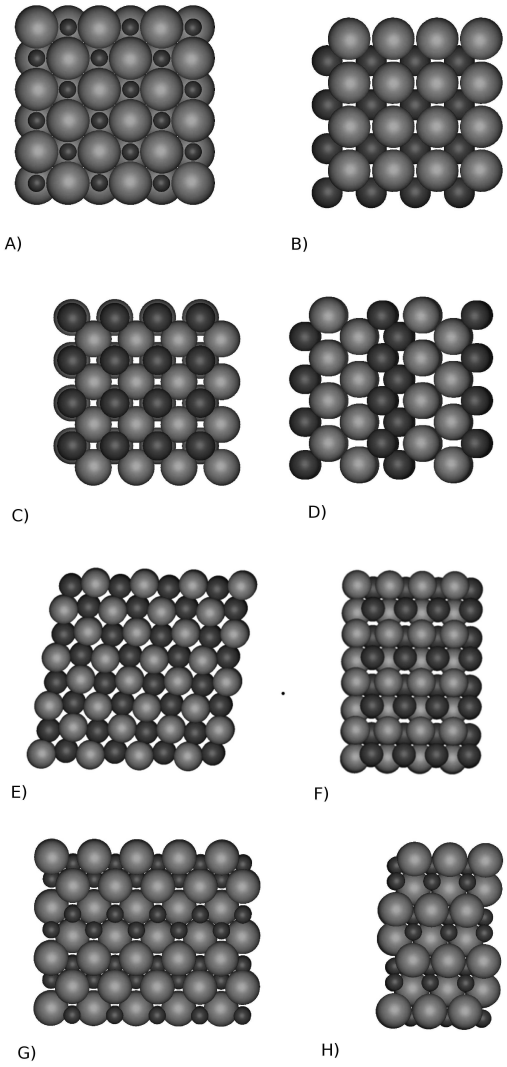

Figure 2.5: Cartoons of the AB crystal structures which have the best overall packing for a given size ratio. A) NaCl, $q = 0.4$, B) CsCl, $q = 0.73$, C-D) γCuTi, $q = 0.8$, xy and xz planes respectively, E-F) αIrV, $q = 0.82$, xy and xz planes G-H) CrB, $q = 0.6$ xy and xz (Colour online)

these calculations were motivated by experimental evidence for these structures in approximately hard-sphere systems, as well as the fact that they all pack well at some size ratio. The packing fractions of these structures is shown in Figure 2.3 and 2.4. Experimentally, AlB_2 and $icoAB_{13}$ have been seen in a large variety of systems, including gem opals [6], approximately hard colloidal systems [28, 29] , and more recently in nanoparticles [25, 48]. NaCl, NiAs, the Laves phases, and CsCl have also been seen experimentally in colloidal systems [28, 49–51] and nanoparticle systems [25]. While the question remains whether these experimentally realized particles interact with truly a hard core interaction, these structures nonetheless present a reasonable starting place for finite pressure calculations.

While the Laves phases are predicted to be stable for a finite pressure region when $q = 0.76$ to 0.84 (see Chapter 3), in Figure 2.4 we see that the Laves phases are not the

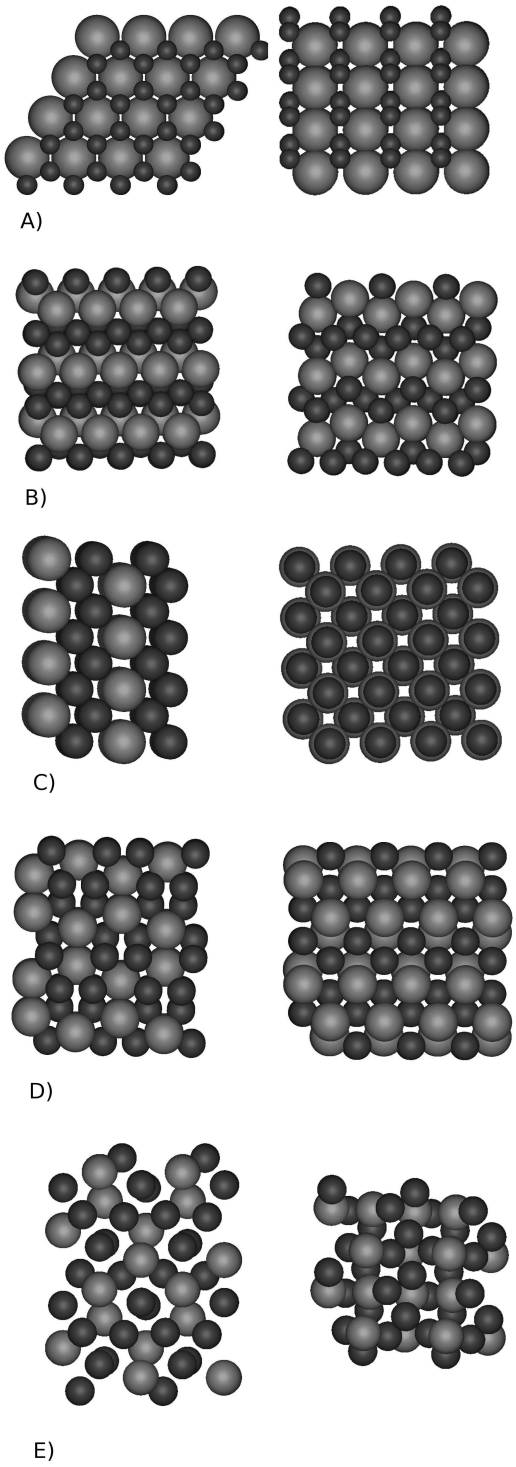

Figure 2.6: Cartoons of the AB_2 crystal structures which have the best overall packing for a given size ratio. A) AlB_2, $q = 0.6$, B) $HgBr_2$, $q = 0.69$, C) $AuTe_2$, $q = 0.78$ D) S74e/h , $q = 0.72$ E) $AgSe_2$, $q = 0.82$ (Colour online)

best packed candidates in this range. In particular, at $q = 0.82$ we find a number of structures which pack better than the Laves phases, including αIrV, γCuTi, $AuTe_2$ and Ag_2Se. Full free-energy calculations show that the only stable structures at this size ratio are the Laves phases. Additionally, constant pressure NPT MC simulations show that Ag_2Se melts into $MgCu_2$ at pressures where the more symmetric $MgCu_2$ is predicted to be stable. Thus, Ag_2Se can be looked at as a high pressure distortion of $MgCu_2$. Hence, at a size ratio of 0.82 the binary hard-sphere system seems to favor the more symmetric crystal structure over the best packed structure. As a result, the space filling arguments currently being used to explain the crystal structures of nanoparticles, specifically, studies such as Ref. [25], which make the direct association of the entropic contribution to the free energy with the space filling curves, are not always valid.

In contrast, while $icoAB_{13}$ packs better then $cubAB_{13}$, as shown in Figure 2.3, NPT MC simulations show that the more symmetric $cubAB_{13}$ melts into $icoAB_{13}$ for the size ratio range where $icoAB_{13}$ is predicted to be stable. In this case it appears that the system chooses the lower symmetry, higher packed crystal structure in agreement with the space filling arguments. However, in this case, the result violates the symmetry principle proposed by Laves in 1956 [52], which states that the structure with the highest symmetry is adopted.

Taken together, these results imply that when examining the phase behavior of systems at finite pressures it is important to examine *both* the close-packed structures and the related higher symmetry crystal structures. While it is possible that this behavior is simply due to the particle free volume not scaling with the unit cell volume, the fact that the system (as in the case of the Laves phases) sometimes chooses the lower packed, higher symmetry structures indicates that lattice vibrations may be important in the phase behavior of binary hard-sphere crystal structures. Our results also show that there are a number of additional structures, particularly for $q > 0.6$, not previously studied in the context of binary hard-sphere mixtures which may be stable for binary hard-sphere systems. Moreover, as the structures stable for hard spheres are also seen in systems with soft interactions, for instance NaCl, AlB_2, $icoAB_{13}$ and the Laves phases have been seen in nanoparticle systems [24, 25] and $icoAB_{13}$ was seen in block copolymer micellar systems [31], the predicted structures can also be used as a starting point for phase behavior studies of many such systems.

In conclusion, we have used a combination of a GA, MC NPT simulations, and simulated annealing techniques to predict close-packed binary hard-sphere crystalline structures for a wide range of stoichiometries and sphere diameter ratios. The results are in agreement with the known structures and show that there are a number of as yet unexamined binary crystal structures with competing packing fractions for q between 0.6 and 0.84. Additionally, our results demonstrate the importance of full Gibbs free-energy calculations in determining the stability of binary crystal structures indicating that the association of the entropic free-energy contribution to the packing fraction is not always valid Finally, we stress that our GA and NPT MC simulations can easily be extended to find crystal structures for multi-component mixtures, particles with soft interactions, and non-spherical particles.

3

Stability of AB and AB_2 crystal structures in binary hard-sphere mixtures

We study by computer simulations the stability of various crystal structures in a binary mixture of large and small spheres interacting with a hard-sphere potential. We consider structures that have atomic prototypes CrB, γCuTi, αIrV, $HgBr_2$, $AuTe_2$, Ag_2Se and the Laves phases ($MgCu_2$, $MgNi_2$, and $MgZn_2$) as well as a structure with Space Group symmetry 74. By utilizing Monte Carlo simulations to calculate Gibbs free energies, we determine composition versus pressure and constant volume phase diagrams for diameter ratios of $q = 0.74$, 0.76, 0.8, 0.82, 0.84, and 0.85 for the small and large spheres. For diameter ratios $0.76 \leq q \leq 0.84$, we find the Laves phases to be stable with respect to the other crystal structures that we considered and the fluid mixture. By extrapolating to the thermodynamic limit, we show that the $MgZn_2$ structure is the most stable one of the Laves structures.

3.1 Introduction

Hard spheres are interesting model systems due to their extreme simplicity and yet complex behavior that includes freezing into solid phases and glass formation. While the stable solid structure of pure hard spheres is always the face-centered-cubic (fcc) crystal phase [53] with a maximum packing fraction of ~ 0.741, the number of stable crystal structures is increased enormously when one considers binary mixtures of large and small hard spheres. The first experimental observations of binary crystal structures of hard-sphere-like particles were made by Sanders [7] in natural gem opals. Later, other authors, [30, 50, 54] observed binary crystals with the large (A) and small (B) spheres arranged in AB_2 (atomic analog AlB_2) and AB_{13} (atomic analog $NaZn_{13}$) structures. It has since been shown that both of these structures are stabilized by entropy alone [17]. The AlB_2 structure is stable at diameter ratios $0.45 \leq q \leq 0.61$ for the small and large spheres and the $NaZn_{13}$ structure is stable at $0.54 \leq q \leq 0.625$ [15, 16, 47].

The space filling of hard spheres has been used as a starting point for various theoretical studies regarding the phase behavior of binary hard-sphere systems (e.g. Ref. [17]) and to explain experimental observations in binary mixtures of colloids with approximately hard interactions [30, 54]. At infinite pressures the crystal structure with the highest close packed density will be stable. However, at lower pressures the stability of a structure is determined by the free energy, which for hard spheres reduces to a purely entropic contribution. It is often asserted in such systems that the free volume per particle is inversely related to the packing fraction of a crystalline structure, and that the entropy is proportional to the free volume. While this argument is incomplete, as evidenced by the stability of $NaZn_{13}$ which has a maximum packing fraction of 0.738 which is lower than for pure fcc, it has been used successfully by various authors to determine candidate crystalline structures to examine using full free-energy calculations [15–17].

Recently, it was proposed, based on Gibbs free-energy calculations, that AB_2 Laves crystal structures with atomic analogs $MgCu_2$, $MgNi_2$, and $MgZn_2$ are stable in the range $0.76 \leq q \leq 0.84$ [45]. All three Laves structures have the same maximum packing fraction, $\eta \approx 0.710$ at $q \approx 0.816$. However, in Chapter 2 we examined the packing of binary crystal structures in more detail and a number of additional crystal structures have been identified which pack at least as well as the Laves phases for the size ratios in question. These structures were identified through the combined use of a genetic algorithm (GA) and Monte Carlo simulations.

In the size ratio of interest for this chapter, namely sphere diameter ratios between 0.74 and 0.85 the AB structures which packed best have atomic prototypes CrB, CsCl, and γCuTi, while the AB_2 structures included $HgBr_2$, $AuTe_2$, Ag_2Se, and a structure with the Space Group symmetry 74 with Wyckoff positions e and f occupied, which we call S74 (see Chapter 2). In this chapter we use Gibbs free-energy calculations to compare the stability of these various new phases with the Laves structures and present composition vs. pressure and constant volume phase diagrams for binary mixtures of hard spheres for size ratios $q = 0.74$, 0.76, 0.8, 0.82, 0.84, and 0.85. The only stable binary crystal structures we find on this interval are the Laves phases, with a stability range of $0.76 \leq q \leq 0.84$. Moreover, we find that $MgZn_2$ is the most stable of the Laves structures in the thermodynamic limit where the number of particles is taken to infinity.

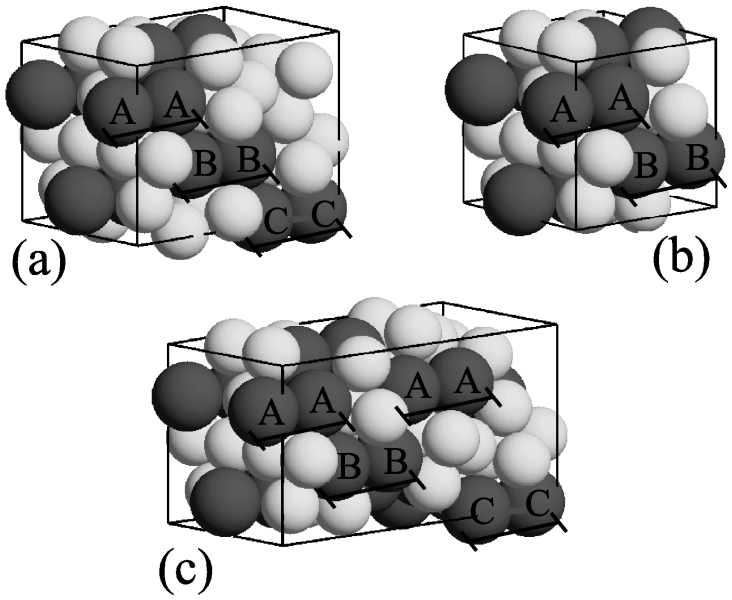

Figure 3.1: (Color online) The Laves phases. The large spheres are dark (red) and the small spheres are light (yellow). (a) $MgCu_2$, (b) $MgZn_2$, (c) $MgNi_2$

The Laves structures are shown in Figs. 3.1(a)-(c), and as can be seen, they differ only in the way the hexagonal layers formed by the doublets of large (red) spheres are packed: In the $MgCu_2$ structure in Fig. 3.1(a), this packing is AABBCC, in the $MgZn_2$ structure in Fig. 3.1(b) AABB, and in the $MgNi_2$ structure in Fig. 3.1(c) AABBAACC. These different packings can be compared to the ABC and AB packings of hexagonal planes in fcc and hexagonal-close-packed (hcp) crystals, respectively.

To calculate the stability of the phases, we calculate the Gibbs free energy using Monte Carlo simulations. Typically, Monte Carlo free-energy calculations consists of two steps: one first calculates the Helmholtz free energy of a crystal at a single density using the Einstein crystal (or Frenkel-Ladd) method and then combines this with a fitted equation of state from e.g. constant pressure simulations to give the free energy in the whole density range. This approach is followed in this chapter. The advantage of the Monte Carlo free-energy calculations compared to the theoretical approaches is that the results are more accurate since there are no approximations and the error only comes from the statistical noise and the finite system size. This allows us to determine the free-energy differences between the three Laves structures that all have the same maximum packing fraction, and where the applicability of approaches based on free volume arguments can be doubted. Such an approach is followed in the cell theory by Cottin and Monson [55, 56]. In this theory, the free volume, i.e. the configurational integral, of each sphere is sampled using Monte Carlo simulations with the surrounding spheres frozen at their lattice sites. The individual sphere partition functions are then combined to give the total partition function and hence the free energy. While this approach has been shown to give good agreement with Monte Carlo simulations, [19, 57, 58] it can miss subtle free-energy differences such as the difference between the Laves phases.

This chapter is organized as follows. In section 3.2, we introduce the methods used to calculate the phase diagrams. In section 3.3 we present the phase diagrams for binary mixtures of hard spheres. We end with conclusions in section 3.4.

3.2 Methods

We consider a binary mixture of N_L large spheres with diameter σ and N_S small spheres with diameter $q\sigma$ where $q < 1$. The pair potential in units of k_BT between two hard spheres is given by

$$\frac{u_{ij}^{\mathrm{HS}}(r)}{k_BT} = \begin{cases} 0 & r \geq \frac{1}{2}(\sigma_i + \sigma_j) \\ \infty & r < \frac{1}{2}(\sigma_i + \sigma_j). \end{cases} \tag{3.1}$$

where r is the center of mass difference between sphere i and j, and σ_i is the diameter of particle i.

The phase diagrams are determined using common tangent constructions on Gibbs free energy data. The Gibbs free energy G is given by $G = F + PV$, where F is the Helmholtz free energy, P is the pressure, and V is the volume. In the case of the binary hard-sphere fluid and the pure face-centered-cubic (fcc) hard-sphere crystal, the Gibbs free energies G are obtained from the analytical functions given in the literature [59, 60]. In order to obtain the Gibbs free energy of the remaining crystalline phases of hard spheres, the Helmholtz free energy F was calculated using Monte Carlo simulations and combined with the equation of state (P vs. η) data. Below we describe this procedure in more detail.

The Helmholtz free energies of the solid phases are calculated with the Frenkel-Ladd method [20, 21] using Monte Carlo simulations in the canonical ensemble where the number of particles N, volume V, and temperature T are fixed. In the Frenkel-Ladd method, one starts from an Einstein crystal where the particles are tied to their ideal lattice positions by harmonic springs. Then, the springs are slowly removed and one recovers the original interactions. The auxiliary potential energy function that includes the harmonic springs is given by

$$U_\lambda(\mathbf{r}^N) = U(\mathbf{r}^N) + k_BT\lambda\alpha\sum_{i=1}^{N}(\mathbf{r}_i - \mathbf{r}_{0,i})^2/\sigma^2, \tag{3.2}$$

where $\mathbf{r}_{0,i}$ is the lattice position of particle i, α is a dimensionless spring constant, and $\lambda \in [0,1]$ is a coupling parameter. For the hard-sphere system, $U(\mathbf{r}^N)$ in Eq. (3.2) is given by a sum of hard-core potentials (3.1). At $\lambda = 0$, we recover the system of interest with the original interactions, while at $\lambda = 1$, once the spring constant α is chosen large enough, the particles do not "feel" each other and the system reduces to an Einstein crystal with Madelung energy $U(\mathbf{r}_0^N)$ (the potential energy of a crystal with all particles at their lattice positions which for hard spheres is identically zero). The Helmholtz free energy is obtained from [20, 21, 61]

$$\begin{aligned} F(N,V,T) &= F_{\mathrm{Ein}}^{\mathrm{CM}}(N,V,T,\alpha) + F_{\mathrm{CM}}(N,V,T) \\ &\quad - \frac{\alpha k_BT}{\sigma^2}\int_0^1 d\lambda \left\langle \sum_{i=1}^{N}(\mathbf{r}_i - \mathbf{r}_{0,i})^2 \right\rangle_\lambda^{\mathrm{CM}}, \end{aligned} \tag{3.3}$$

where the ensemble average $\langle \ldots \rangle_\lambda^{\mathrm{CM}}$ is calculated with the Boltzmann factor $\exp(-U_\lambda/k_BT)$ for a crystal with fixed center of mass. In Eq. (3.3), the free energy of an Einstein crystal with fixed center of mass is given by

$$F_{\mathrm{Ein}}^{\mathrm{CM}}(N,V,T,\alpha) = U(\mathbf{r}_0^N) + \frac{3(N-1)}{2} k_B T \ln\left(\frac{\alpha\Lambda^2}{\pi\sigma^2}\right), \tag{3.4}$$

where Λ is the de Broglie wavelength, and the term

$$F_{\mathrm{CM}}(N,V,T) \;=\; k_B T \ln\left(\frac{\Lambda^3}{V N^{1/2}}\right), \tag{3.5}$$

corrects for the fixed center of mass. As noted in Ref. [20], it is useful to rewrite the integral in Eq. (3.3) as

$$\int_{\ln c}^{\ln(\alpha+c)} (\lambda\alpha + c) \left\langle \sum_{i=1}^{N} (\mathbf{r}_i - \mathbf{r}_{0,i})^2/\sigma^2 \right\rangle_\lambda^{\mathrm{CM}} d[\ln(\lambda\alpha + c)], \tag{3.6}$$

where

$$c = \frac{k_B T}{\left\langle \sum_{i=1}^{N} (\mathbf{r}_i - \mathbf{r}_{0,i})^2/\sigma^2 \right\rangle_0^{\mathrm{CM}}}. \tag{3.7}$$

The integral in Eq. (3.6) is evaluated numerically using a Gauss-Legendre quadrature [62] with 10-20 integration points.

We calculated Gibbs free energies by first calculating the Helmholtz free energy at a reference state with packing fraction η_r and then we use equation of state (P vs. η) data obtained from constant pressure simulations (where the number of particles N_L and N_S, pressure P, and temperature T are constant) to calculate the Gibbs free energy at all densities. We define the packing fraction $\eta = \zeta N/V$ with

$$\zeta = \frac{\pi}{6}\sigma^3[(1-x) + xq^3] \tag{3.8}$$

where $x = N_S/(N_L + N_S)$ is the composition, and $N = N_L + N_S$. Employing the equation of state $P(\eta')$ for $\eta' \in [\eta_r, \eta]$, the Gibbs free energy at η is obtained from

$$\frac{G(\eta)}{N k_B T} = \frac{F(\eta_r)}{N k_B T} + \frac{P(\eta)V}{N k_B T} + \frac{\zeta}{k_B T}\int_{\eta_r}^{\eta} \frac{P(\eta')}{(\eta')^2} d\eta'. \tag{3.9}$$

Equation (3.9) assumes that the reference packing fraction η_r is within the packing fraction range scanned in the constant pressure simulations. In order to evaluate the integral in Eq. (3.9), the equation of state data was fitted by analytical functions. For the solid phases, the fitting was done using

$$\frac{PV}{N k_B T} = \sum_{i=-1}^{n} a_i \gamma(\eta)^i, \tag{3.10}$$

where $\gamma(\eta) = \eta_{\mathrm{cp}}/\eta - 1$ and η_{cp} is the maximum packing fraction of the solid [47]. The series was typically truncated at $n = 3$. We performed additional Helmholtz free-energy

calculations to check that the fitting procedure and the subsequent integration in Eq. (3.9) produce accurate results.

The ensemble averages for the Helmholtz free-energy calculations were obtained from MC simulations that consisted of 20 000-100 000 equilibration steps (trials to displace each particle once) and 20 000-200 000 sampling steps. In the constant pressure simulations, we used 200 000 equilibration steps and 400 000 sampling steps.

The solid free energies calculated using the above procedure have a system-size dependence that scales as $1/N$ [61]. While in many cases this system-size dependence only has an insignificant effect on the phase behavior, it is an important factor in determining the relative stability of solids that have the same packing efficiency and similar structure, and that therefore can be expected to have nearly equal free energies, as is the case for the fcc and hcp solids [53]. Not surprisingly the free energies of the three Laves phases $MgCu_2$, $MgZn_2$, and $MgNi_2$ turned out to be very close to each other. In order to remove the system-size dependency, we used the method introduced in Ref. [61] where one performs free-energy calculations for increasing N and extrapolates to the $N \to \infty$ limit.

3.3 Results

We determine the phase diagrams for size ratios $q = 0.74$ 0.76, 0.80, 0.82, 0.84, and 0.85 by calculating the Gibbs free energy for CrB, γCuTi, αIrV, $HgBr_2$, $AuTe_2$, $AgSe_2$, S74, and the Laves phases. We employ analytical expressions [59, 60] for the fluid and the fcc phase. Figures 3.2-3.7 show the phase diagrams in the composition $x = N_S/(N_L + N_S)$ - reduced pressure $p = P\sigma^3/k_BT$ plane. The constant pressure representation follows directly from the common tangent constructions and is the most natural one from a theoretical point of view as this representation can be used e.g. in nucleation studies. In order to compare our results with experimental data, we convert the phase diagram to the corresponding η_S-η_L representation. In Figs. 3.8-3.13 we show the phase diagrams for the corresponding η_S-η_L plane. The only stable solid phases we find for this size ratio are the Laves phases and the pure fcc phases. In the phase diagrams, "fcc_L" and "fcc_S" denote the fcc crystals of pure large and pure small spheres, respectively. The common features in all the phase diagrams are the stable fluid phase at low pressure, a phase coexistence between an fcc crystal of large spheres and the fluid ("fcc_L+fluid") at elevated pressure for $x \lesssim 2/3$, and a phase coexistence between an fcc crystal of small spheres and the fluid ("fluid+fcc_S") at elevated pressure and $x > 2/3$. At very high pressure, we find a coexistence between fcc crystals of pure large and pure small spheres ("fcc_L+fcc_S"). From Figs. 3.3-3.6 we see that the Laves phases are stable at size ratios $0.76 \leq q \leq 0.84$ in the intermediate pressure range between the fcc-fluid coexistence region and the fcc-fcc coexistence. The stable regions of Laves phases consist of a small pocket where the Laves phases coexist with a fluid phase at low pressure followed by larger coexistence regions of fcc and Laves phases at higher pressure. Figures 3.3-3.6 show that the Laves phases become stable at $p \approx 25$ for all size ratios $0.76 \leq q \leq 0.84$. We also see that when q increases from 0.82 to 0.84, the region of stable Laves phases first shrinks and then disappears at $q = 0.85$. Similar behavior is observed at lower size ratios when q decreases from 0.8 to 0.76 and 0.74. We would like to point out here that the phase diagram we drew for size ratio $q = 0.85$ only

Phase	N	$n_{\text{eq}} \times 10^3$	$n_{\text{prod}} \times 10^3$	F_{ex}/Nk_BT	$\pm$
$MgCu_2$	216	40	800	7.3957	0.0010
$MgCu_2$	648	40	300	7.4230	0.0010
$MgCu_2$	1080	20	100	7.4286	0.0010
$MgCu_2$	2592	20	20	7.4347	0.0010
$MgCu_2$	5760	20	20	7.4361	0.0010
$MgZn_2$	288	40	800	7.4028	0.0003
$MgZn_2$	1080	20	100	7.4257	0.0010
$MgZn_2$	2304	20	20	7.4315	0.0010
$MgZn_2$	4800	20	20	7.4327	0.0004
$MgNi_2$	288	40	800	7.4043	0.0004
$MgNi_2$	1440	40	100	7.4304	0.0010
$MgNi_2$	2304	20	20	7.4327	0.0020
$MgNi_2$	5760	20	20	7.4351	0.0005

Table 3.1: System sizes and simulation details used to calculate the excess Helmholtz free energies in Fig. 3.14 for $q = 0.82$ and $\eta = 0.6$. n_{eq} and n_{prod} are the number of MC cycles in the equilibration and production runs, respectively, and the error estimate is given by the standard deviation of four independent runs.

takes into consideration the Laves phases and the monodisperse fcc phases. Specifically, we have not considered a substitutional solid solution when drawing this phase diagram. The size ratio $q = 0.85$ has been examined before, and a substitutional solid solution has been found to be stable. Hence, for a complete phase diagram for size ratio $q = 0.85$ see Ref. [19].

Figure 3.14 plots the excess Helmholtz free energy per particle F_{ex}/Nk_BT plus $\ln(N)/N$ as a function of $1/N$ at $q = 0.82$ and $\eta = 0.6$ for the Laves phases $MgCu_2$, $MgNi_2$, and $MgZn_2$. The Helmholtz free-energy calculations were performed in a cubic or nearly cubic box. Details of the calculations can be found in Table 3.1. Note that the number of production MC cycles, n_{prod} is reduced as the system size is increased without noticeable effect on the accuracy. This can be done because in large systems spatial averaging replaces some of the time averaging. In Fig. 3.14, the solid lines are linear fits to the data points. As shown in Ref. [61], $F_{\text{ex}}/Nk_BT + \ln(N)/N$ is a linear function of $1/N$ and the intercept at $1/N = 0$ gives the excess free energy of the infinite bulk system. Analyzing the intercept values, we find that $MgZn_2$ has the lowest bulk free energy per particle at $7.436k_BT$, followed by $MgNi_2$ at $7.438k_BT$, and $MgCu_2$ at $7.439k_BT$. That is, the free-energy difference between the three Laves phases is on the order of 10^{-3} k_BT per particle. Due to the small free-energy difference, one expects to observe in experiments a mixture of all three Laves phases similar to the experimental observation of the random-hexagonal-close-packed (rhcp) crystals of pure hard spheres, which can be seen as a mixture of fcc and hcp crystals.

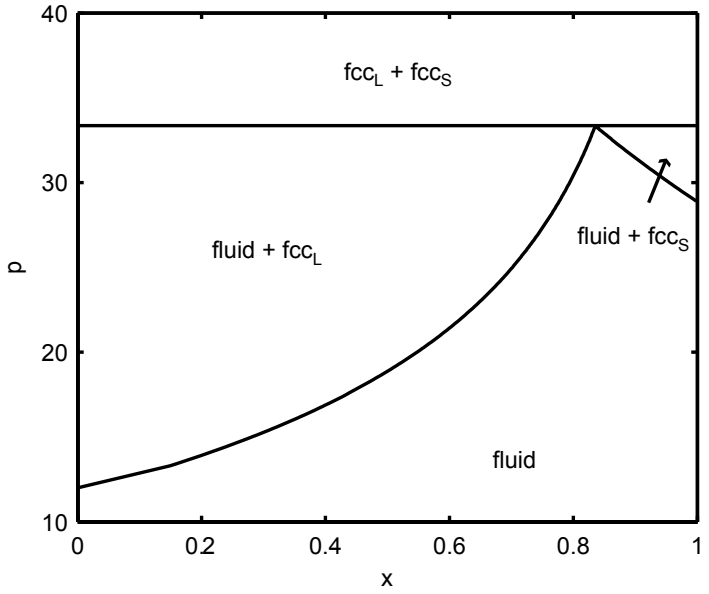

Figure 3.2: Phase diagram of binary hard-sphere mixtures in the composition $x = N_S/(N_L + N_S)$ - reduced pressure $p = P\sigma^3/k_BT$ plane with size ratio $q = 0.74$. Labels "$\mathrm{fcc_L}$+fluid" and "fluid+$\mathrm{fcc_S}$" denote coexistence regions between an fcc crystal of large (L) or small (S) spheres and a fluid, and "$\mathrm{fcc_L}$+$\mathrm{fcc_S}$" denotes a coexistence region between fcc crystals of large and small spheres.

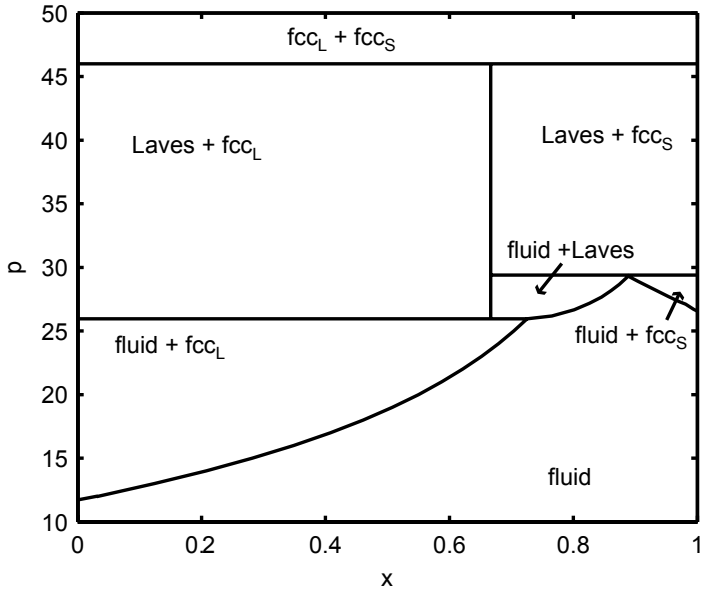

Figure 3.3: Phase diagram of binary hard-sphere mixtures in the composition $x = N_S/(N_L + N_S)$ - reduced pressure $p = P\sigma^3/k_BT$ plane with size ratio $q = 0.76$. The labels are the same as in Fig. 3.2, and additionally "$\mathrm{fcc_L}$+Laves", "Laves+$\mathrm{fcc_S}$", and "Laves+fluid" denote the coexistence regions between the Laves phase and an fcc crystal of large (L) or small (S) spheres, or a fluid.

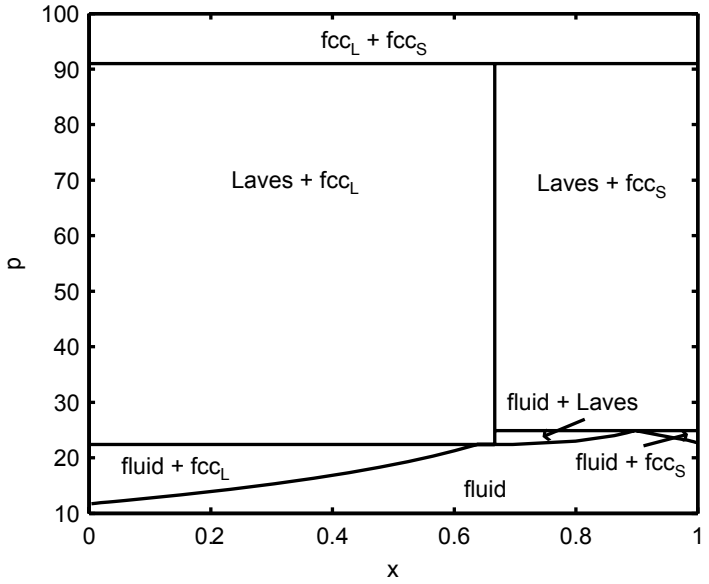

Figure 3.4: Phase diagram of binary hard-sphere mixtures in the composition $x = N_S/(N_L + N_S)$ - reduced pressure $p = P\sigma^3/k_BT$ plane with size ratio $q = 0.8$. The labels are the same as in Fig. 3.3.

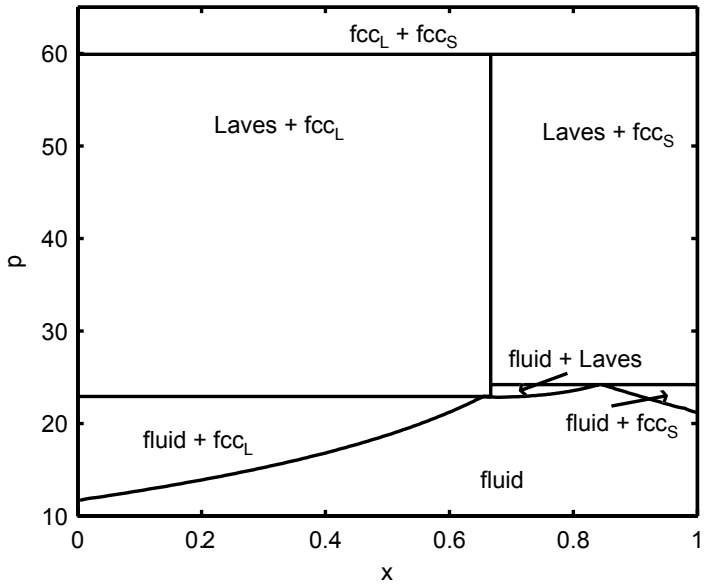

Figure 3.5: Phase diagram of binary hard-sphere mixtures in the composition $x = N_S/(N_L + N_S)$ - reduced pressure $p = P\sigma^3/k_BT$ plane with size ratio $q = 0.82$. The labels are the same as in Fig. 3.3.

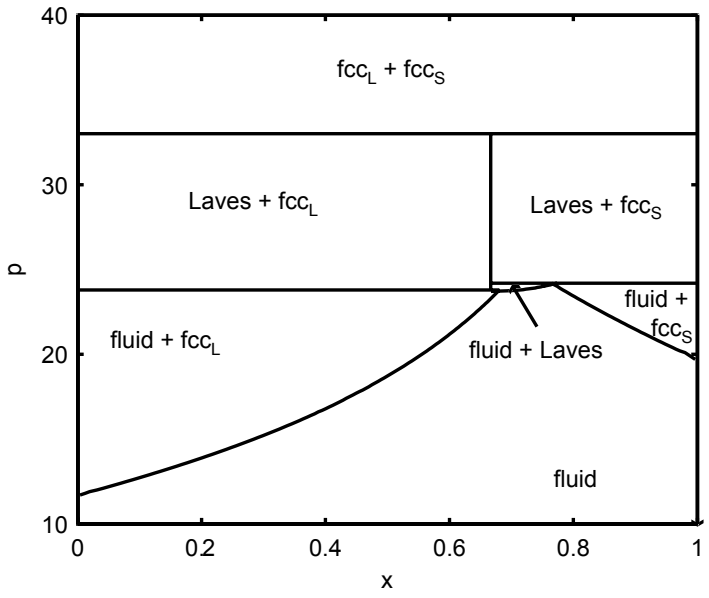

Figure 3.6: Phase diagram of binary hard-sphere mixtures in the composition $x = N_S/(N_L + N_S)$ - reduced pressure $p = P\sigma^3/k_BT$ plane with size ratio $q = 0.84$. The labels are the same as in Fig. 3.3.

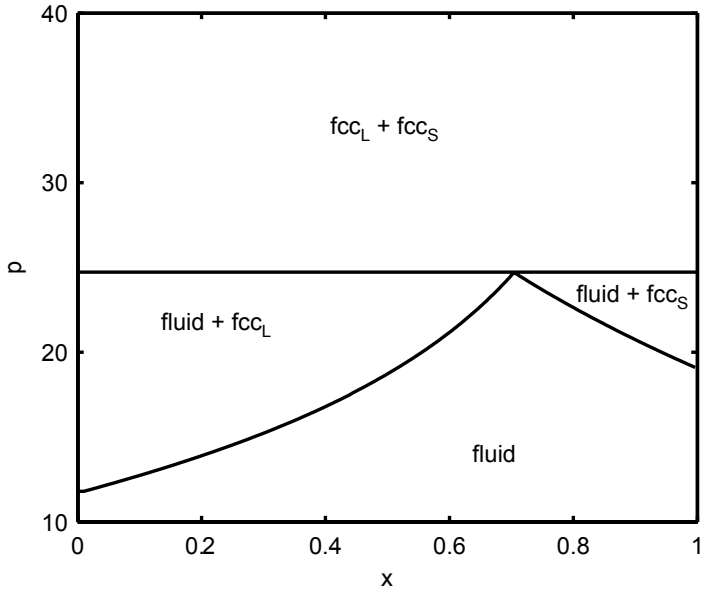

Figure 3.7: Phase diagram of binary hard-sphere mixtures in the composition $x = N_S/(N_L + N_S)$ - reduced pressure $p = P\sigma^3/k_BT$ plane with size ratio $q = 0.85$. The labels are the same as in Fig. 3.2.

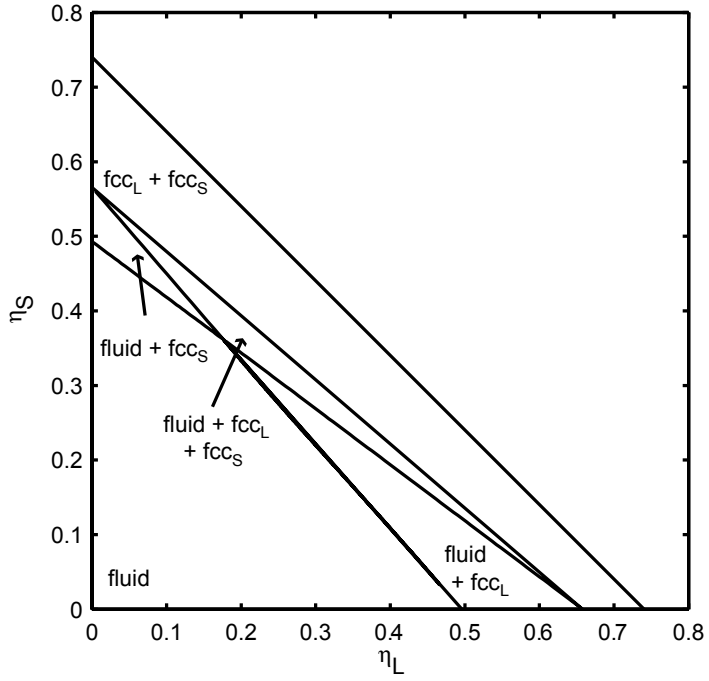

Figure 3.8: Phase diagram of binary hard-sphere mixtures in the $\eta_S - \eta_L$ representation with size ratio $q = 0.74$. The labels are the same as in Fig. 3.2.

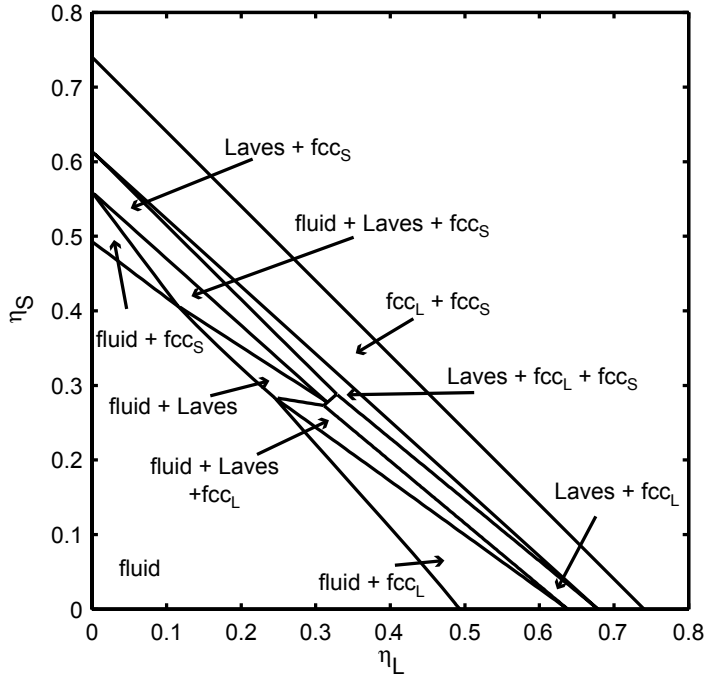

Figure 3.9: Phase diagram of binary hard-sphere mixtures in the $\eta_S - \eta_L$ representation with size ratio $q = 0.76$. The labels are the same as in Fig. 3.3.

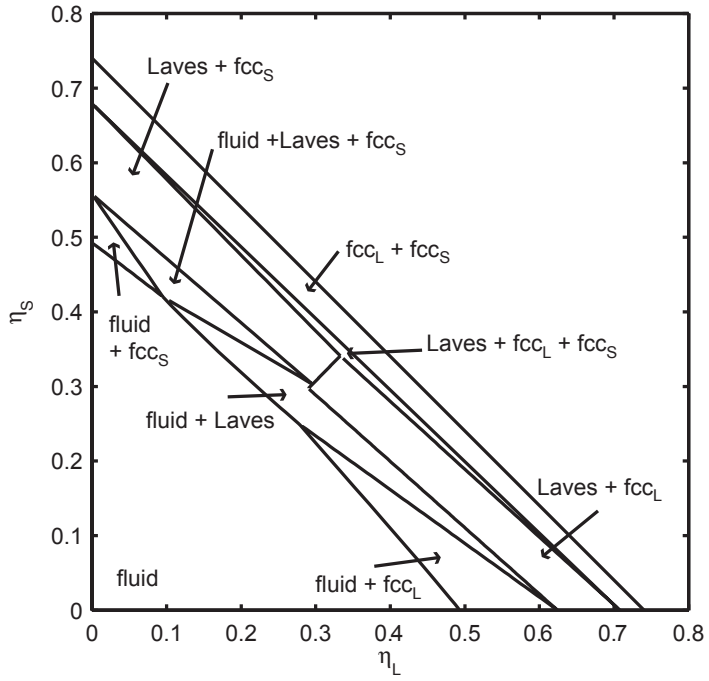

Figure 3.10: Phase diagram of binary hard-sphere mixtures in the $\eta_S - \eta_L$ representation with size ratio $q = 0.80$. The labels are the same as in Fig. 3.3.

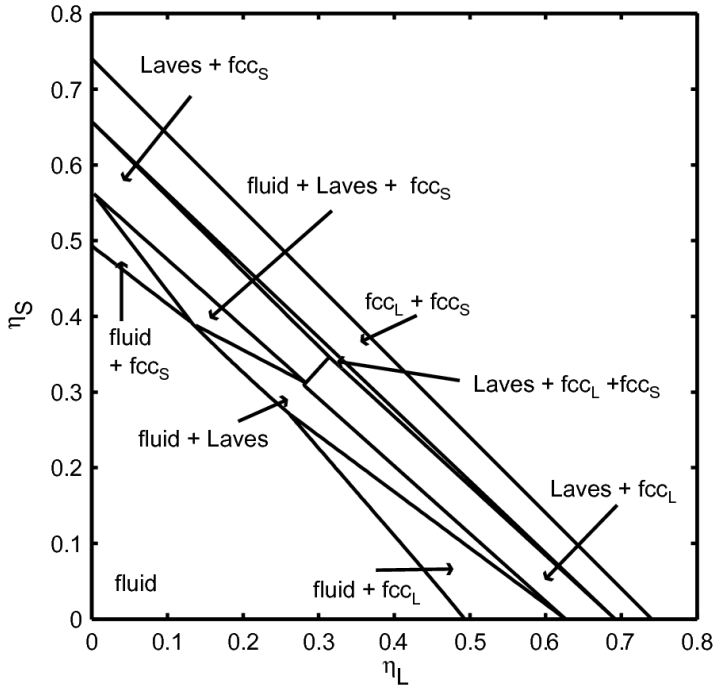

Figure 3.11: Phase diagram of binary hard-sphere mixtures in the $\eta_S - \eta_L$ representation with size ratio $q = 0.82$. The labels are the same as in Fig. 3.3.

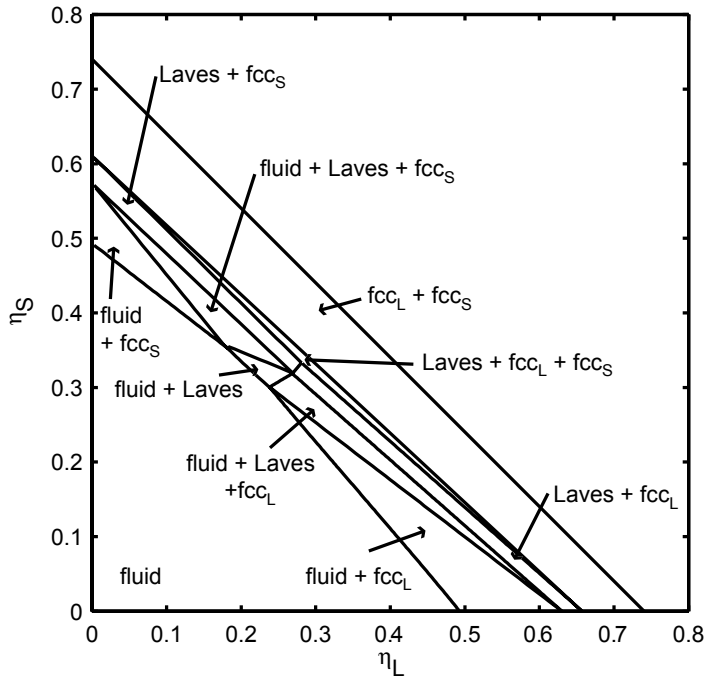

Figure 3.12: Phase diagram of binary hard-sphere mixtures in the $\eta_S - \eta_L$ representation with size ratio $q = 0.84$. The labels are the same as in Fig. 3.3.

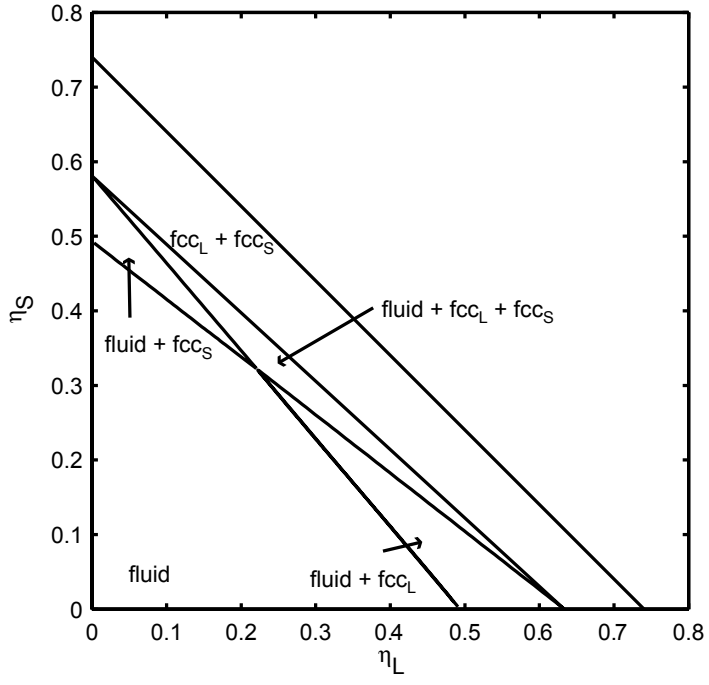

Figure 3.13: Phase diagram of binary hard-sphere mixtures in the $\eta_S - \eta_L$ representation with size ratio $q = 0.85$. The labels are the same as in Fig. 3.2.

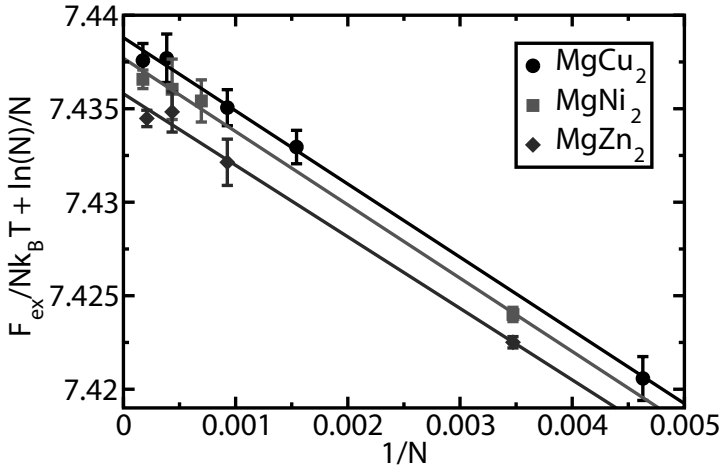

Figure 3.14: (Color online) Finite-size scaling of the excess Helmholtz free energy, $F_{\rm ex}/Nk_BT + ln(N)/N$ vs. $1/N$ at $q = 0.82$ and $\eta = 0.6$ for the Laves phases $MgCu_2$, $MgNi_2$, and $MgZn_2$. The lines are linear fits to the data points.

3.4 Conclusions

We have presented phase diagrams in the composition x vs. pressure p and in the η_S-η_L representation for binary hard-sphere mixtures of large and small hard spheres for size ratios $q = 0.74$, 0.76, 0.8, 0.82, 0.84, and 0.85. The phase diagrams are based on Gibbs free energy data calculated using thermodynamic integration techniques and constant pressure Monte Carlo simulations. We showed that the Laves structures, $MgCu_2$, $MgZn_2$, and $MgNi_2$, are stabilized by entropy alone and that they are stable with respect to fluid mixtures, binary CsCl, CrB, γCuTi, αIrV, $HgBr_2$, $AuTe_2$, Ag_2Se, S74, and single component fcc crystal structures at size ratio range $0.76 \leq q \leq 0.84$. By extrapolating our free energy data to the infinite system limit, we showed that the free-energy difference between the three Laves phases is small, order 10^{-3} k_BT per particle, and that the $MgZn_2$ crystal has the lowest free energy followed by $MgNi_2$ and $MgCu_2$.

3.5 Acknowledgements

I would like to thank Antti-Pekka Hynninen for his original work on the binary hard-sphere phase diagrams.

4

An efficient method for predicting crystal structures: Variable box shape simulations

In this chapter we present an efficient and robust method based on Monte Carlo simulations in the isotension ensemble for predicting crystal structures *at finite temperature*. We apply this method, which is surprisingly easy to implement, to a variety of systems, thereby demonstrating the effectiveness of the method for hard interactions, attractive interactions, anisotropic interactions, binary mixtures, semi-long-range soft interactions, and truly long-range interactions. In the case of binary hard-sphere mixtures, star polymers, and binary Lennard-Jones mixtures, the crystal structures predicted by this algorithm are consistent with literature, thereby providing confidence in the robustness of the method. We also demonstrate that this method can be combined with Ewald sums and can be applied to systems with long-range interactions. Finally, we predict new crystal structures for hard asymmetric dumbbell particles, bowl-like particles, patchy particles and hard oblate cylinders and present the phase diagram for the oblate spherocylinders based on full free-energy calculations.

4.1 Introduction

The ability of atomic, colloidal, and nanoparticle systems to self-organize into crystal structures makes the prediction of stable crystal structures in these systems an important challenge for science. In a recent Review Article, Woodley and Catlow claim "The prediction of structure at the atomic level is one of the most fundamental challenges in condensed matter science" [63]. It is therefore not surprising that the subject has received much attention from the scientific community over the last several decades.

The question itself is deceivingly simple: assuming that the underlying interactions between constituent particles are known, which crystal structures are stable. Before the 1990s most of our understanding of atomic crystal structures came from simple empirical rules, now well documented in solid state text books. In 1990, Pannetier *et. al.* proposed a method based on simulated annealing techniques [64]. In their method a general crystal structure was described in terms of lattice and basis vectors, and the 'cost' function for the system was minimized using simulated annealing. This method can easily be extended to any atomic system for which a suitable 'cost' function, e.g. the potential energy or enthalpy, can be constructed [65]. Similarly, in 2009 Torquato [66] applied a method based on pressure annealing for determining dense packings of platonic and archimedean solids. Typically these pressure [66] and temperature [64, 65, 67] annealing simulations break the (detailed) balance condition (i.e. these methods cause a deviation from the Boltzmann distribution). When only the zero temperature or infinite pressure structures are required the detailed balance condition is not expected to be important. However, if the objective is to find stable crystal structures, as we will discuss in this chapter, it is advantageous to use a simulation method which does not a priori break detailed balance and thus which samples configuration space according to the Boltzmann distribution, such as regular Monte Carlo or Molecular Dynamics simulations. We would also like to point out that simulations which do not break detailed balance have been applied to the study of phase transitions between solid phases [68, 69]. Particularly, Monte Carlo simulations and Molecular Dynamics simulations where the box shape was allowed to fluctuate have been applied for this purpose. However, these simulations were not used to find crystal structures appearing out of the liquid and relied on an initial guess of the crystal structure.

In addition to simulated temperature and pressure annealing methods, more advanced minimization techniques such as genetic algorithms (see e.g. Refs. [36, 38] and Chapter 2 of this thesis), and Monte Carlo basin hopping algorithms [70] have been applied. Typically these techniques are used to locate the minimum in the potential energy of the system, and as such, probe the *zero-temperature* phase behavior. However, for systems where the *entropy* plays a significant role, these techniques break down. For instance, new crystal structures can appear in the phase diagram at finite temperature, which are different from the zero-temperature crystal structures, and hence predicting the zero-temperature structures will not be sufficient for making predictions at finite temperature. Additionally, for hard systems the potential energy is always zero as only non-overlapping configurations contribute to the partition function, and hence, crystal structures are stabilized by entropy alone. For such systems it is difficult to construct an appropriate 'cost' function, and therefore the Monte Carlo basin hopping algorithm and the genetic algo-

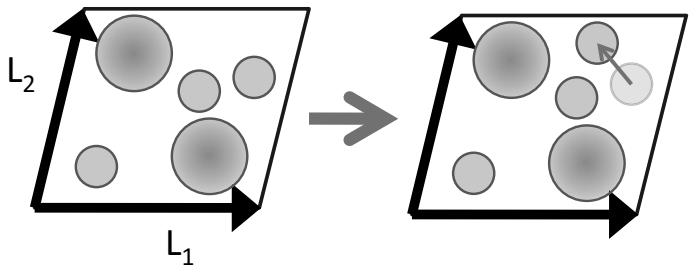

Figure 4.1: In the algorithm used in this chapter, the unit cell of the crystal is the simulation box. Here we give an example of a particle move in our system. Left: A sample (2 dimensional) unit cell (i.e. simulation box) where the lattice vectors are labelled L_1 and L_2. Right: The same unit cell as on the left after a particle has been moved.

rithms cannot directly be applied to hard-core systems *. With the recent progress in the chemical synthesis and fabrication of colloidal particles and nanoparticles, there is unprecedented ability to control the interparticle interactions in such systems, through particle synthesis and chemistry [8, 71, 72], through the solvent in which they are dispersed [73], and through the application of external fields [9]. The resulting interactions between the colloidal particles can be made sufficiently weak that emerging crystal structures are stabilized predominantly by entropic contributions to the free energy. For instance, experimental realizations of binary hard-sphere mixtures and hard bowl-like particles as described in this chapter, are stabilized purely by entropy. Additionally, crystal structures found in binary mixtures of nanoparticles (eg. NaCl, AlB_2, $NaZn_{13}$) are consistent with hard-sphere interactions, indicating a significant entropic contribution to the free energy of these systems [74]. Hence, locating stable crystal structures for soft interactions at finite temperature and for hard-core interactions presents an important and exciting challenge and plays a vital role in the rational design of advanced materials.

One attempt to predict crystal structures for such systems is the ergodicity search algorithm described in Ref [75]. In the algorithm, the entropic contribution to the free energy is approximated by the harmonic phonon contribution. However, even such an approximation is difficult and computationally expensive, and not straightforward to apply to hard-core interactions.

In this chapter we present a novel method to predict crystal structures at finite temperature for a wide variety of systems, including systems whose phase behavior is purely entropy-driven such as binary hard-sphere mixtures, hard asymmetric dumbbells, hard bowl-like particles, and hard oblate cylinders. The chapter is organized as follows, in Section 4.2 we describe the method we use, in Section 4.3 we describe our results and in Section 4.4 we describe our conclusions.

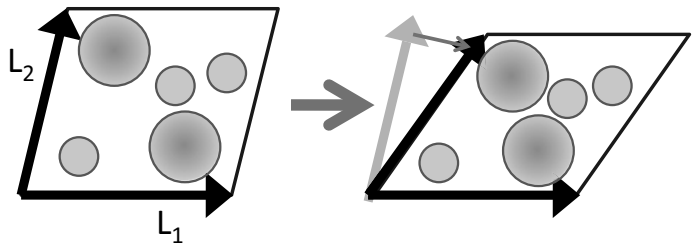

Figure 4.2: An example volume move in our algorithm. On the left is the system before the volume change and on the right is the same system after the volume change.

4.2 Method

The general algorithm consists of Monte Carlo (MC) simulations in an isotension-isothermal ensemble. In our MC simulations, lattice vectors $\vec{L}$ comprise the simulation box, and the positions of the particles in the crystal, i.e. the basis vectors $\vec{R}$, are expressed in terms of these lattice vectors (see the cartoon in Figure 4.1). As is typical for an MC simulation in the isothermal-isobaric (NPT) ensemble, each MC step consists of either a trial particle displacement (Figure 4.1) or a trial volume change (Figure 4.2) where the acceptance rules of the particle and volume moves are given by the Metropolis algorithm and thus by defination obey detailed balance (see Ref. [20]). In order to allow for box shape fluctuations, a trial volume move involves an attempt to change the orientation and the length of a random lattice vector. An important part of our algorithm is to treat the simulation box as a unit cell, and as such work with extremely small particle numbers. In this chapter, the number of particles in the simulation box ranges from 1-12. Working with small simulation boxes, and allowing the shape of the simulation box to fluctuate introduces new problems for the simulations. The main problem is that while the system is in the liquid phase, the shape of the box fluctuates significantly. Thus, the box can become extremely distorted, which makes the potential energy summation time consuming. To avoid this problem, we use a lattice reduction technique to redraw the unit cell when it becomes too distorted. In 2D we use the well-known Gaussian reduction algorithm, while in 3D we use the lattice reduction method described in Ref. [38]. Additionally, we impose a restriction on all the angles and the lengths of the lattice vectors to avoid trivial unphysical crystal structures. Without these restrictions the particles tend to line up in columns, such that the particles only interact with their own periodic images in one of the lattice directions resulting in unphysical contributions to the entropy. Angles less than 30^o and greater than 150^o are not accepted. Such a condition prevents the box (particularly while in the fluid phase) from an extreme distortion, while allowing for all possible crystal phases to emerge in our simulations. Additionally, for each configuration of interest, we run several parallel MC runs, with various starting configurations and pressures.

*For more details on how one might apply a minimization algorithm to hard particles, see Chapter 2.

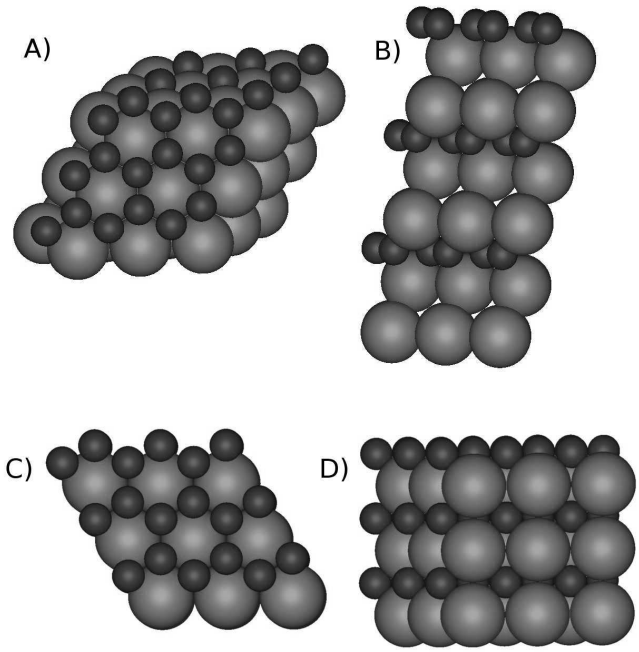

Figure 4.3: A) and B) correspond respectively to the xy and xz faces of the AB crystal structure from Space Group 166 found in the set of predicted phases for size ratios 0.4-0.6. C) and D) correspond to the xy and xz phases of the AlB_2 crystal structure. Note that the planes made by the small particles in both structures correspond to 2D honeycomb planes, while the large colloids sit on a hexagonal lattice.

4.3 Results

We applied this method to several representative systems: binary hard-sphere mixtures, binary Lennard-Jones mixtures, star polymers, dipolar hard spheres in an electric field, asymmetric hard dumbbells, hard bowl-like particles, patchy particles and hard oblate cylinders. In this section we explore our results for each system.

4.3.1 Binary hard-sphere mixtures

In the case of binary hard-sphere mixtures, the initial pressure was chosen such that the simulation started in the fluid phase. The pressure was increased slowly until the particles crystallized, and the crystal structure remained constant. In order to facilitate the identification of the crystal structure, the pressure was then increased significantly. The results for AB and AB_2 crystal structures are shown in Table I for varying size ratios $q = \sigma_S/\sigma_L$ with $\sigma_{L,S}$ the diameter of the large and small hard spheres, respectively. The close packed structures for AB [44, 76] and AB_2 [76] stoichiometry have been predicted previously, using a genetic algorithm (see Chapter 2) and a simulated annealing technique using structures from a crystallographic database [44]. We note that all the structures predicted in Ref. [44, 76] are also predicted by our algorithm as shown in Table I. Additionally, the stability of the AB and AB_2 structures has been determined in computer

q	structure AB (2:2)	%	structure AB_2 (4:8)	%
0.4	**NaCl**	40%		
	NiAs	20%		
	SG 166*	30%		
0.5	SG 166	60%	**AlB_2**	55%
	CrB	30%		
0.6	CrB	70%	**AlB_2**	40%
	SG 166	10%		
	SG 12	10%		
0.7	CsCl	40%		
	CrB	20%		
0.8	γCuTi	30%	**Laves**	75%
	αIrV	10%	SG139	5%
	CsCl	10%		

Table 4.1: AB and AB_2 structures predicted for binary hard-sphere mixtures for various size ratio $q = \sigma_S/\sigma_L$. Each simulation was repeated between 10-20 times with different initial configurations, and the frequency (%) of the resulting structures is listed. * has been used to denote structures which are slightly distorted from their symmetric structure. Structures which have been previously predicted to be stable [15–17, 77] are indicated in bold. For $q = 0.4$ and 0.7, our method was unable to predict ordered AB_2 crystal structures, which is consistent with the fact that no AB_2 structures are stable for these size ratios.

simulations using free-energy calculations. These studies show that NaCl is stable for $q \in [0.414 - 0.45]$ [15], AlB_2 for $q \in [0.45 - 0.61]$ [16, 17], and the Laves phases are stable for $q \in [0.76 - 0.84]$ [18]. We indeed observe from Table I that the stable crystal structures, which are denoted in bold, are indeed predicted by our new method.

For $q = 0.5$ we see that the most frequently occurring AB crystal structure is not the best packed structure CrB, but rather a crystal structure within the symmetry group 166 (denoted SG 166). A cartoon of this structure along with AlB_2 is shown in Figure 4.3. While AlB_2 is stable for $q = 0.5$, no AB stoichiometry crystal structure is found to be stable. An examination of SG 166 shows that while it has a different stoichiometry than AlB_2, it has similar planes, ie. the small colloids sit on a 2D honeycomb lattice, while the larger colloids are in hexagonal planes. Thus it appears that while the system was unable to find the structure with the lowest free energy since the stoichiometry was incorrect, it located a compromise.

The crystal structures appearing at $q = 0.8$ are also of significant interest. At this size ratio the Laves phases are expected to be stable. Our results show that a significant majority of our simulations have resulted in Laves phases (75%). It is interesting to note that we have been able to improve the results for this size ratio dramatically by restricting the length of the lattice vectors. When this restriction is removed, we only find 30% resulting in the Laves phases. Additionally, for all q, the runs with 12 particles per unit cell do not produce crystal structures when this restriction is removed.

Summarizing, we find that our method predicts the stable crystal structures for binary

ρ	0.5	1.5	2.25	2.5	3	3.75
structure	fcc	trigonal*	diamond	diamond	hexagonal*	hcp

Table 4.2: Results for star polymers with a arm number $f = 64$ and corona diameter $\sigma = 1$ as a function of the number density ρ. * cartoons of these crystal structures can be found in Ref. [79].

hard-sphere mixtures, including a few additional structures which are the best packed crystal structures for the given stoichiometry, and structures whose planes were related to stable crystal structures.

4.3.2 Binary Lennard-Jones mixtures

A recent Molecular Dynamics (MD) simulation demonstrated that the Wahnström binary Lennard-Jones mixture, which has often been used in simulations to study glassy behavior, crystallizes spontaneously into the $MgZn_2$ Laves phase [78]. The Lennard-Jones interaction is given by

$$u(r_{ij}) = 4\epsilon_{ij}\left[(\sigma_{ij}/r_{ij})^{12} - (\sigma_{ij}/r_{ij})^{6}\right], \tag{4.1}$$

where the Lorentz-Berthelot mixing rule

$$\sigma_{AB} = (\sigma_{AA} + \sigma_{BB})/2 \tag{4.2}$$

was used. Choosing the parameter $\epsilon_{AA} = \epsilon_{BB} = \epsilon_{AB} = 1$, and $\sigma_{BB}/\sigma_{AA} = 0.8 - 0.84$, we have also located predominantly the $MgCu_2$ and $MgZn_2$ Laves phases, which is consistent with Ref. [78].

4.3.3 Star-polymers

Star polymers [80] interact via a soft interaction given by

$$\beta V(r) = \begin{cases} \left(\frac{5}{18}\right) f^{3/2}\left[-\ln\left(\frac{r}{\sigma}\right) + \left(1 + \frac{\sqrt{f}}{2}\right)^{-1}\right] & r \le \sigma \\ \left(\frac{5}{18}\right) f^{3/2}\left(\frac{\sigma}{r}\right)\left(1 + \frac{\sqrt{f}}{2}\right)^{-1} & r > \sigma \end{cases} \tag{4.3}$$

where f is the arm number and σ is the corona diameter. In this interaction the potential scales with the temperature, and thus there are only two thermodynamic parameters relevant in the phase behaviour, the arm number f and the number density. For studying this system, we changed the volume move in our MC simulation. We only allowed for box shape moves which keep the overall volume of the system fixed. In order to obey detailed balance, this was done in the following manner. Two random lattice vectors were chosen, and from each lattice vector a random component. A random δr was chosen from the interval $[-\delta r_{max}, \delta r_{max}]$ and added to one of the lattice vector components, and the other vector was changed in such a way that the volume remained unchanged. In the case of star polymers a single Monte Carlo simulation visited a large range of crystal structures,

and even upon reaching the lowest energy structure, would then transform again. Thus in this case, for each run we saved the 5 crystal structures with the lowest energy. We then found the crystal structure with the lowest potential energy and compared it with results for a genetic algorithm search and found complete agreement [38]. The results are shown in Table 4.2.

4.3.4 Dipolar hard spheres

We also implemented box shape moves in a system with long-range interactions, i.e., a system of dipolar hard spheres in an electric field. The interaction potential is given by

$$\beta u(\mathbf{r}) = (\gamma/2)(\sigma/r)^3(1 - 3\cos(\theta)) \tag{4.4}$$

with $\gamma = 15$. The phase behavior of this system has been studied previously [77], and the three known stable crystal structures are the body-centered-tetragonal (bct), face-centered-cubic (fcc) and hexagonal-close-packed (hcp) phase. The crystal phases predicted by our algorithm included bct, fcc, and hcp, and are consistent with previous phase diagram calculations [77], thereby demonstrating that our method can be applied to systems with long-range interactions.

4.3.5 Hard asymmetric dumbbells

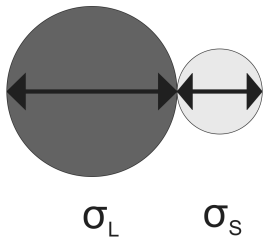

Figure 4.4: Cartoon of hard asymetric dumbell.

In the case of asymmetric dumbbell particles consisting of a tangent large and small hard sphere (see Figure 4.4), our method predicts crystal structures that are atomic analogs of the NaCl, CsCl, γCuTi, CrB, and αIrV when we regard the two individual spheres of each dumbbell independently. (Cartoons of these strutures are found in Chapter 2). The bonds that connect the dumbbells appear to connect random small-large pairs, and hence the crystal structures are in fact aperiodic in positional and orientational order. These results are consistent with the structures found for the AB stoichiometry structures of the binary hard-sphere mixtures (see Chapter 2). We also point out that on further studies of the hard asymmetric dumbbells, where we examined the melting of the crystalline phases, we also observed a rotator phase based on an underlying NaCl crystal lattice. This appears to be the asymmetric dumbbell analogue of the hopping in the interstitial solid solution examined in Chapter 5 for binary hard-sphere mixtures.

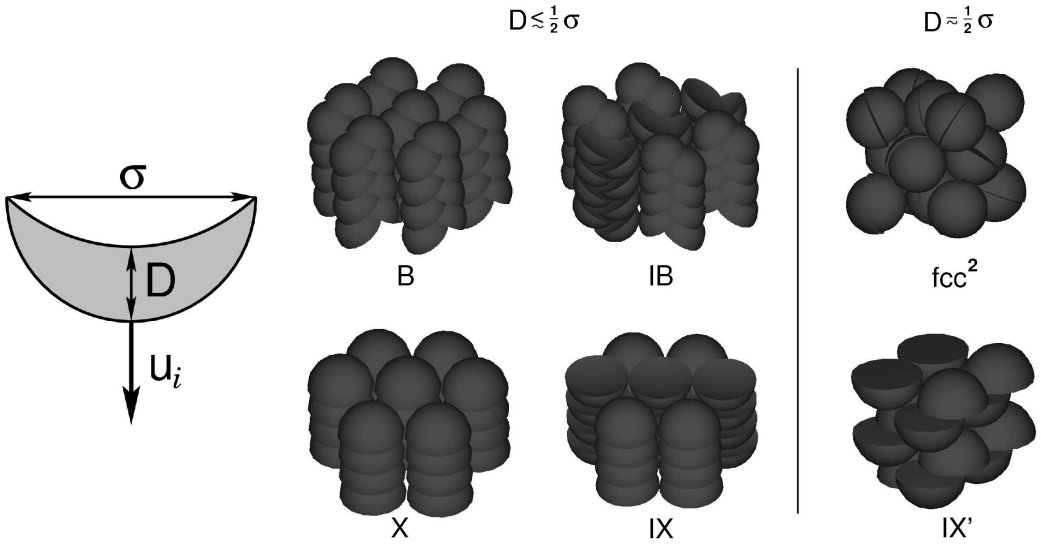

Figure 4.5: Cartoon and predicted crystal structures for bowl-like particles.

4.3.6 Hard bowl-like particles

The bowl-like particles are modeled by the solid of rotation of a crescent, where the thickness of the crescent is denoted by D, the diameter by σ, and the axis of rotation is defined as $\mathbf{u}$. A cartoon of the particles is shown in Figure 4.5. To predict the crystal structures, unit cells of 2 to 6 particles were examined. The system was initialized at a pressure of $\beta p\sigma^3 = 10$ and was increased by a factor of 10 each step until a pressure of $\beta p\sigma^3 = 10^6$ was reached. The resulting structures are shown in Figure 4.5. Subsequent free-energy calculations showed that four of the six predicted crystal structures are indeed stable: IB, IX', IX and fcc^2 [81].

4.3.7 Patchy particles

Here we consider a system of patchy particles modeled as hard spheres whose surface is decorated by 6 bonding sites at fixed locations in a regular geometry [82]. The pair potential between particles is the sum of an isotropic hard-core repulsion of diameter σ and a site-site anisotropic attraction. Sites on different particles interact via a square-well potential of depth $\epsilon = 1$ and attraction range $\delta = 0.119\sigma$. Hence, the interaction $V(\mathbf{1}, \mathbf{2})$ between particles $\mathbf{1}$ and $\mathbf{2}$ is

$$V(\mathbf{1}, \mathbf{2}) = V_{HS}(\mathbf{r_{12}}) + \sum_{i=1}^{f} \sum_{j=1}^{f} V_{SW}(\mathbf{r}_{12}^{ij}) \tag{4.5}$$

where the individual sites are denoted by i and j, V_{HS} is the hard-sphere potential, $V_{SW}(z)$ is a square-well interaction (of depth $-\epsilon$ for $z \leq \delta$, 0 otherwise) and $\mathbf{r_{12}}$ and $\mathbf{r}_{12}^{ij}$ are respectively the vectors joining the particle-particle and the site-site (on different particles) centers. Two particles are identified as bonded when their pair interaction

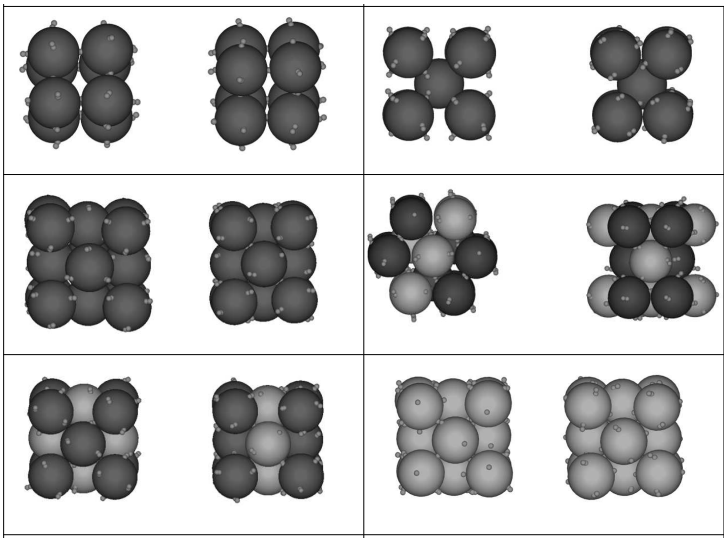

Figure 4.6: A colour version of this figure can be found on page 123. The figure shows the unit cells of (from left to right, from up to down): the fully bonded SC crystal, the fully bonded BCT crystal, the fully bonded FCC crystal (all of them with energy per particle e=-3), the HCP unit cell whose average energy per particle is $e = -2.25$, and two partially bonded FCC crystals, with average energy respectively $e = -2.5$ and $e = -2.0$. Note that the number of bonds per particle is indicated by the colour, red for 6 bonds, blue for 5 bonds and turquoise for 4 bonds.

energy is -ϵ. The choice of δ guarantees that each site is engaged at most in one bond. Each particle can thus form only up to 6 bonds and consequently the average energy per particle, e, can vary from 0 (system of monomers) down to -3 (fully bonded systems).

We show in Fig. 4.6 the predicted crystal structures: a face-centered-cubic (FCC) crystal, a hexagonal-close-packed (HCP) structure, a body-centered-tetragonal (BCT) crystals, and a simple cubic (SC) crystal. Since the number of bonds per particle is well defined, particles in the snapshots have colours determined by their number of bonds (red = 6 bonds, blue = 5 bonds, turquoise = 4 bonds), while sticky sites are always coloured in green. To better visualize the bonded sites, patches of particles not belonging to the unit cell are represented together with patches of particles belonging to the unit cell.

4.3.8 Hard oblate cylinders

Hard oblate spherocylinders [83, 84] are rounded cylinders with a diameter D and a thickness L as depicted in Figure 4.7a. For this system, we find the two crystal phases, X_{tilted} and X_{aligned}, depicted in Figure 4.7. In the X_{tilted} phase the particles are tilted with respect to each other. Surprisingly, no analog crystal phase exists in the more conventional model for platelets, i.e. cut spheres [85]. We note that the X_{aligned} phase is the analog to the crystal phase seen in cut spheres, where all particles point in the same direction. The phase diagram for this system is presented in Figure 4.7. Interestingly, both predicted crystal structures are stable in some region of phase space, specifically, X_{titled} for $L/D \lesssim 0.46$ and X_{aligned} for larger L/D. It should be noted that this phase diagram is based on full free-energy calculations, which are examined elsewhere [86].

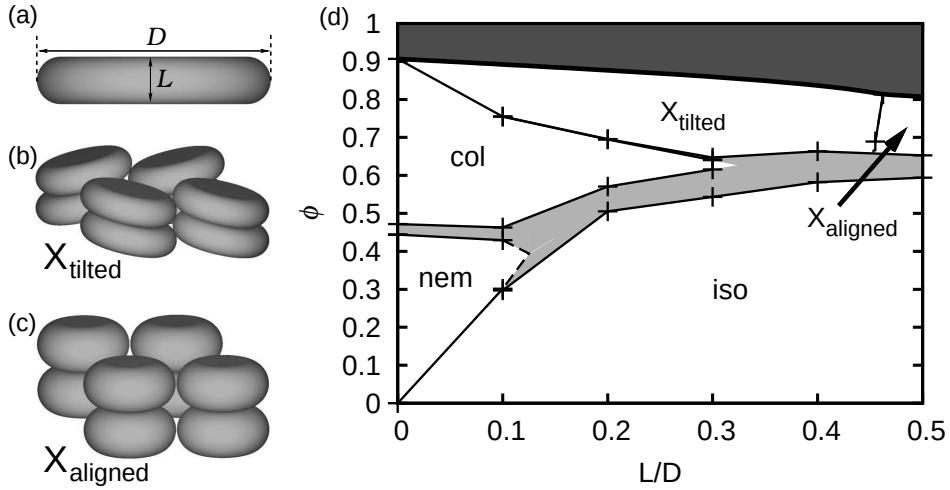

Figure 4.7: The phase diagram of hard oblate spherocylinders in the packing fraction (ϕ) versus dimensionless thickness (L/D) representation as obtained by free-energy calculations (d), where the diameter D and thickness L are depicted in (a). The state points in the dark gray area are inaccessible since they lie above the maximum close packing line. X_{aligned} and X_{tilted}, denote the aligned and tilted crystal structures as shown in (b) and (c), "iso" is the isotropic fluid, "nem" the nematic phase, and "col" is the columnar phase. The lines are a guide to the eye. The coexistence packing fractions of the nematic and the columnar phase for $L/D = 0$ are from Ref. [87].

4.4 Conclusions

In conclusion, we have presented an algorithm to predict candidate crystal structures at finite temperature for a wide variety of systems. We have established the reliability of our method as all the predicted structures are consistent with the literature. In particular, the binary hard-sphere mixtures, binary Lennard-Jones mixtures, star polymers and long range dipolar system all yielded crystal structures consistent with literature. Additionally, we have applied the method to a variety of systems not previously studied in literature, namely hard asymmetric dumbbells, patchy particles, hard bowl-like particles and hard oblate cylinders.

We note that the algorithm is extremely simple to implement. We expect this algorithm to be widely applicable in the study of new materials, such as colloidal particles, nanoparticles, and micelles.

4.5 Acknowledgements

I would like to thank Matthieu Marechal for his work on the hard bowl-like particles and hard oblate cylinders, Frank Smallenburg for his work on the long-range interactions, Daniel Pelt for his work on the Lennard Jones system and Bas van Oorschot for his work on the anisotropic dumbbells, and Emanuela Bianchi for her work on the patchy particles.

5

Self-assembly of a colloidal interstitial solid solution

In this chapter we explore theoretically and experimentally the self-assembly of a purely entropic interstitial solid solution. Using full free-energy calculations, we calculate the constant pressure and constant volume phase diagrams for mixtures of hard spheres with diameters σ_S and σ_L for size ratios $q = \sigma_S/\sigma_L = 0.3, 0.4$ and 0.42. For these size ratios we find large regions of phase space where an interstitial solid solution is stable. In particular, we find interstitial solid solutions for which the filling fraction of small particles is completely tunable from 0-100%, taking the system from a monocomponent face-centered-cubic to an NaCl crystal structure. We also find regions of stability for a binary liquid, phase separated monodisperse face-centered-cubic structures of the large and small particles, and binary crystal phases with AB_6 stoichiometry. Additionally, we examine in detail the diffusion of small particles in the interstitial solid solution arising in binary hard-sphere mixtures with size ratio $q = 0.3$. In contrast to most systems, we find a region where the diffusion of small particles increases as a function of the packing fraction.

5.1 Introduction

An interstitial solid solution (ISS) occurs when a random selection of interstitial sites on a lattice are filled by a different species. In general, ISSs can be found in systems which obey the Hume-Rothery rules: the solute particles must be smaller than the holes in the underlying (solvent) lattice and the electronegativity of both the solvent and solute must be similar. They appear frequently in atomic systems, e.g. crystalline iron is strengthened by the addition of interstitial carbon atoms yielding steel, and hydrogen can be dissolved into intermetallic compounds resulting in metal hydrides for hydrogen storage [88]. However, to the best of our knowledge, a thermodynamically stable ISS phase has not been reported in colloidal and nanoparticle mixtures.

Hard-core particle mixtures are one of the most important systems for modelling and understanding phase behaviour in colloidal, nanoparticle and atomic systems. First, while interactions between nanoparticles and colloids are complicated, arising from e.g. Van der Waals interactions, steric stabilization, electrostatics, and depletion effects [89], they can often be minimized such that these particles behave like hard particles (see. e.g. Refs. [9, 90]). Secondly, the phases found in hard-particle systems are often also present in weakly interacting systems and, as a result, hard-particle phases are often a good starting point for studying the phase behaviour in a wide range of systems. And thirdly, even in the case of strongly interacting systems, the phase behaviour of hard-particle systems is an extremely useful tool for interpreting the phase behaviour, particularly in helping dis-entangle effects associated with interactions from effects associated with the hard core. Hence, the presence of an ISS in a hard-sphere mixture would demonstrate that ISS phases should be generally considered an important class of crystal structures when interpreting and predicting phase behaviour in colloidal and nanoparticle systems.

The stability of an NaCl crystal structure in hard-sphere mixtures has been discussed in a number of papers. Specifically, between size ratios $q = \sigma_S/\sigma_L = 0.3$ and 0.45 stable binary NaCl [15, 28, 51] phases have been reported. An NaCl lattice is constructed by filling all octahedral holes in an FCC lattice of large particles with small particles (Figure 5.1). Thus, a random, incomplete filling trivially results in an ISS (Figure 5.2). The

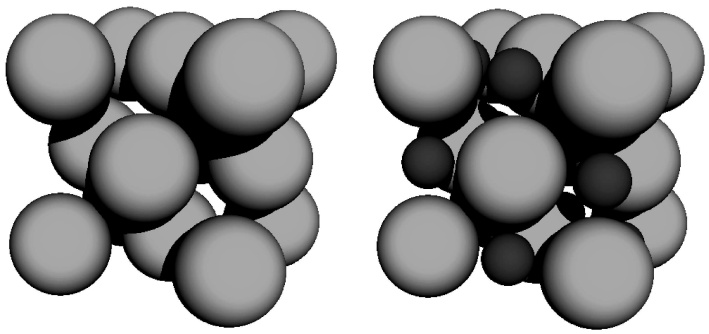

Figure 5.1: Cartoons of crystal structures. On the left is a cartoon image of an FCC lattice and on the right is an FCC lattice with all of the octahedral holes filled by smaller particles resulting in an NaCl crystal structure. Note that the small particles are not drawn to scale.

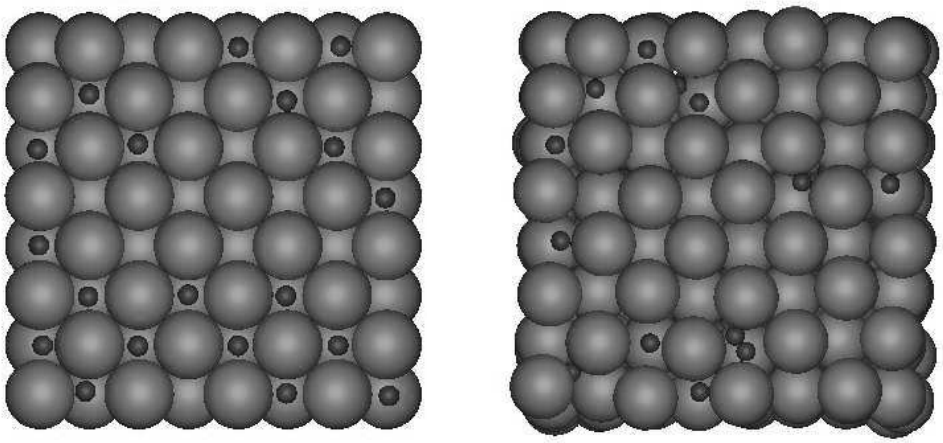

Figure 5.2: Left: A cartoon of an ISS with approximately localized interstitials. Right: A cartoon of an ISS with mobile interstitials.

stoichiometry of the ISS phase is defined as AB_n where n is a fractional number in the range $[0, 1]$. We note that $n = 0$ corresponds to the FCC phase and $n = 1$ to a perfect NaCl structure where the small particles are also on an FCC lattice. An ISS phase can also be constructed by filling some octahedral holes in the monodisperse HCP lattice. In this case a complete filling yields a NiAs crystal. However, both the monodisperse FCC and binary NaCl hard-sphere crystal structures have been shown to be favored over the competing HCP and NiAs phases with free-energy differences on the order of 0.001 k_BT [53, 61] and 0.002 k_BT [51] per particle, respectively. Therefore, in this chapter we focus on the FCC-NaCl based ISSs. We note, however, that free-energy differences on the order of 0.001 k_BT per particle have minimal effect on crystal structures grown in experiments, and consequentially any ISS seen experimentally would be expected to be a mixture of both the FCC-NaCl and HCP-NiAs ISSs. Additionally, the continuous crossover between a perfect FCC crystal, an FCC crystal with interstitial defects, an ISS, an NaCl crystal with vacancies, and a perfect NaCl crystal makes differentiation between an ISS and a defective solid unclear (subjective). Thus, in this chapter, any structure in the crossover regime will be called an ISS. We point out here that experimentally, the presence of interstitials in the holes of the FCC lattice can stem from two main causes: (i) a lowering of the free energy of the system due to the addition of the interstitials resulting in a thermodynamically stable ISS phase, or (ii) thermodynamically unstable phases caused by a kinetic trapping of the system. While these two effects are often difficult to distinguish experimentally, theoretically, full free-energy calculations can demonstrate conclusively if there are thermodynamically stable ISS phases present, and the stoichiometry of such phases.

In this chapter we focus on the phase behaviour found in a binary mixture of large and small hard spheres with diameters σ_L and σ_S respectively, and with size ratios $q = \sigma_S/\sigma_L = 0.3, 0.4$ and 0.42. This chapter is organized as follows. In section 5.2 we calculate the equilibrium phase diagrams, in section 5.3 we discuss the diffusion in a hard-sphere ISS of size ratio $q = 0.3$, in section 5.4 we demonstrate an experimental realization of

an interstitial solid solution, and in sections 5.5 and 5.6 we present a discussion and our conclusions.

5.2 Phase stability of an interstitial solid solution

In this section we examine the equilibrium phase behaviour for binary hard-sphere mixtures with size ratios $q = 0.3, 0.40$ and 0.42. Using the method discussed in Chapter 4, we predict candidate binary crystal structures for this mixture where both species exhibit long-range crystalline order. We find NaCl, NiAs, and, for size ratio $q = 0.3$, a superlattice structure with AB_6 stoichiometry where A (B) represents the large (small) particles. A cartoon of the AB_6 structure is depicted in Figure 5.3.

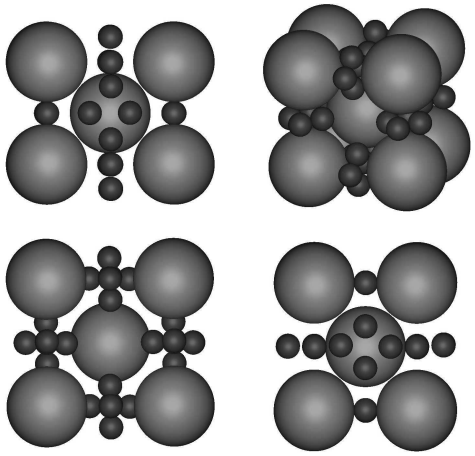

Figure 5.3: Unit cell of the binary AB_6 superlattice structure described in this chapter. Note that both species exhibit long-range crystalline order. The unit cell is based on a body-centered-cubic unit cell of the large particles in contrast to the face-centered-cubic unit cell associated with the interstitial solid solution phase discussed in this chapter.

5.2.1 Phase diagram calculations

To calculate the phase diagrams for binary mixtures of size ratios 0.3, 0.4, and 0.42, we use common tangent constructions to the Gibbs free energies. Specifically we examine the stability of the binary hard-sphere liquid phase, monodisperse FCC crystals of the large and small spheres, the binary NaCl crystal structure, the ISS phase as shown in Figure 5.2 and, for size ratio $q = 0.3$, the AB_6 binary crystal shown in Figure 5.3. The Gibbs free energies of the monodisperse FCC crystal structures as well as the binary hard-sphere fluid are taken from analytic expressions [59, 60]. For the purpose of the common tangent construction, it is useful to fit the Gibss free energy of the liquid at constant pressure as a function of the composition to a simpler function. The Gibbs free energy of the binary fluid fits extremely well to the function

$$\frac{\beta G(x_S)}{N} = b_1 x_S \log(x_S) + b_2(1 - x_S) log(1 - x_S) + \sum_{i=1}^{M} a_i x_S^i \tag{5.1}$$

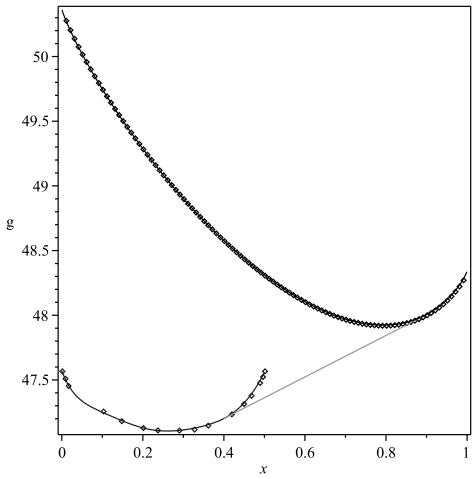

Figure 5.4: Gibbs free energy ($g = \beta G/N$) per particle as a function of concentration for the binary fluid phase, and the ISS phase at a reduced pressure of $\beta P\sigma^3 = 50$. A linear shift $f(x) = ax$ has been subtracted from the free energies to aid in the visualization of the common tangent construction. The open circles are data points from the thermodynamic integration for the ISS and the line is the corresponding fit. The solid data points come from the analytic expression for the free energy of the binary fluid, and the line is the associated fit. The dashed line is the common tangent construction. Note that this plot demonstrates the coexistence between the binary fluid at $x \approx 0.9$ and the ISS with a composition $x \approx 0.4$.

where $x_S = N_S/(N_L + N_s)$ is the concentration of small particles, M is an integer between 3 and 6, and a_i and b_i are fitting parameters.

The Helmholtz free energies of the binary crystal structures are calculated using the Frenkel and Ladd thermodynamic integration method [18, 21, 61]. This method is discussed in detail in Chapter 3. In this method an Einstein crystal is used as the reference system and the particles are attached to their lattice positions using harmonic springs. The thermodynamic integration described by Frenkel-Ladd involves integrating over the associated spring constant. To preform such integrals, we apply Monte Carlo NVT simulations. Once the Helmholtz free energy (F) at a reference packing fraction η^r is known, the Gibbs free energy at any packing fraction can then be determined using

$$\frac{\beta G(\eta)}{N} = \frac{\beta F(\eta_r)}{N} + \frac{\beta P(\eta) V}{N} + \beta\zeta \int_{\eta_r}^{\eta} \frac{P(\eta')}{(\eta')^2} d\eta'. \tag{5.2}$$

with

$$\zeta = \frac{\pi}{6}\sigma_L^3[(1 - x_S) + x_S q^3] \tag{5.3}$$

and where $P(\eta)$ is calculated using a simple NPT Monte Carlo simulation. Note that ζ is the proportionality constant between the packing fraction and the number density (ρ), i.e. $\eta = \zeta N/V$.

To calculate the Helmholtz free energy of the interstitial solid solution, we use the method described in Ref. [14]. In this case, we apply thermodynamic integration and integrate over the fugacity $z_S = \exp(\beta\mu_S)/\Lambda_S^3$ of the small particles. Note that Λ_S is the

de Broglie wavelength of the small particles. The reference system is the FCC crystal of large particles.

If N_L is the number of particles in the underlying FCC lattice of large particles, V is the volume of the system and z_S is the fugacity of the small particles, the free energy of the system in the $N_L V z_S T$ ensemble, which we denote F^z, is then given by

$$\begin{aligned} \beta F^z\left(N_L, V, z_S\right) &= \beta F^z\left(N_L, V, z_S = 0\right) \\ &\quad + \int_0^{z_S} dz'_S \left(\frac{\partial \beta F^z\left(N_L, V, z'_S\right)}{\partial z'_S}\right), \end{aligned} \tag{5.4}$$

where

$$\left(\frac{\partial \beta F^z\left(N_L, V, z'_S\right)}{\partial z'_S}\right) = -\frac{< N_S >_{z'_S}}{z'_S}. \tag{5.5}$$

Applying a Legendre transform, the free energy in the $N_1 N_2 V T$ ensemble can then be written

$$F(N_L, N_S, V, T) = F^z(N_L, V, z_S, T) + \mu_S N_S, \tag{5.6}$$

where μ_S is the chemical potential of the small particles and N_S is the number of small particles. Monte Carlo simulations in the $N_L \mu_S V T$ ensemble are used to determine the average number of small particles as a function μ_S. Again the Gibbs free energy is determined using Eq. 5.2, however, in this case, we use a slightly modified $N_S N_L P T$ Monte Carlo simulation to determine the equation of state. In addition to the typical particle and volume moves, we include trial moves in which a small particle is completely removed from the simulation box and placed at a new random position. The acceptance rule for such a move is the same as for a normal particle move. This move is included to average over the disorder of the small particles in the ISS. The equations of states for the solid NaCl phase, as well as the ISS phases for size ratios 0.3 and 0.4, are fit using the expression

$$\frac{\beta P V}{N} = \sum_{i=-1}^{M} a_i \left(\frac{\eta_{max}}{\eta} - 1\right)^i \tag{5.7}$$

where M is an integer between 3 and 7 and chosen for the best fit, η is the packing fraction, and η_{max} is the maximum packing fraction possible for the given structure. For the ISS with size ratios 0.3 and 0.4, the maximum possible packing fraction is given by

$$\eta_{max} = \frac{\pi\sqrt{2}}{6}(1 + x_S q^3/(1 - x_S)). \tag{5.8}$$

In the case of the ISS for size ratios 0.42, the same fitting function is used, however, η_{max} is also treated as a fitting parameter. The Gibbs free energy at constant pressure as a function of concentration for the ISS is fit to the function

$$\frac{\beta G(x_S)}{N} = b_1 x_S \log(x_S) + \sum_{i=1}^{M} a_i x_S^i \tag{5.9}$$

where M is an integer between 3 and 6.

A sample of the Gibbs free energies for the competing phases, as well as the common tangent construction is shown in Figure 5.4 for size ratio $q = 0.3$ and a reduced pressure $\beta P \sigma^3 = 50$.

5.2.2 Phase diagrams for $q = 0.3, 0.4$ and 0.42

The phase diagrams in the pressure-composition (p-x$_S$) and small particle volume fraction-large particle volume fraction ($\eta_S - \eta_L$) representations for size ratios $q = 0.3, 0.4$ and 0.42 are shown in Figures 5.5, 5.6 and 5.7 respectively. Note that $p = \beta P \sigma_L^3$ is the reduced pressure, $x_S = N_S/(N_S + N_L)$, $N_{S(L)}$ is the number of small (large) hard spheres, $\eta_{S(L)} = \pi\sigma_{S(L)}^3/6V$ is the small (large) sphere volume fraction, $\beta = 1/k_B T$, k_B is the Boltzmann constant, T is the absolute temperature, and V is the volume. From Figures 5.5, 5.6 and 5.7 we see that there is a large region of phase space where the ISS phase is stable. Additionally, the inset in Figures 5.5 demonstrates how the filling of the octahedral holes with small particles in the coexisting ISS increases as a function of pressure, slowly approaching the 100% filling of NaCl. Note that for size ratio $q = 0.3$ the AB_6 phase is also stable.

5.3 Diffusion of small particles in an interstitial solid solution with size ratio $q = 0.3$

We examined the mobility of the small particles using event driven MD simulations. The event driven code employed an optimised version of the algorithm described by Alder and Wainwright [91]. The large particles had a mass m_L and small particles had a mass $m_\mathrm{S} = m_\mathrm{L} * \sigma_\mathrm{S}^3/\sigma_\mathrm{L}^3$. The time was measured in units of $\sigma_\mathrm{L}\sqrt{m_\mathrm{L}/(k_B T)}$. The initial velocities were drawn randomly from a Maxwell-Boltzmann distribution.

A typical trajectory taken by a single small particle determined in event driven MD simulation is shown in Figure 5.8. Clearly, the particles spend most of their time in the octahedral holes of the lattice. However, the particles do not hop directly between the octahedral holes but rather hop via a neighbouring tetrahedral hole in the FCC lattice. This process is also depicted in Figure 5.8. We point out that the tetrahedral holes are significantly smaller than the octahedral holes, $0.225\sigma_\mathrm{L}$ in comparison to $0.414\sigma_\mathrm{L}$ at close packing.

At close packing of the underlying FCC crystal, the interstitials are prevented from moving between neighbouring holes by the presence of the large particles. However, at lower pressures due to larger lattice constants in combination with the motion of particles around their lattice sites (including phonons), the small particles can travel between the octahedral holes. The mean square displacement $\langle(\Delta r_S(t))^2\rangle = \left\langle (r_S(t) - r_S(0))^2 \right\rangle$ of the small particles displays a subdiffusive regime which increases as the number density of the large particles $\rho_L \sigma_L^3$ increases. Here $r_S(t)$ denotes the small particle coordinate at time t. In Figure 5.9 we show this subdiffusive regime for an ISS with stoichiometry $n = 0.5$ and varying $\rho_L \sigma_L^3$. From the mean square displacement we can determine the long-time diffusion coefficient. In Figure 5.10 we plot the long-time diffusion coefficient of the small particles as i) a function of pressure and ii) a function of number density of the large particles $\rho_L \sigma_L^3$, for various stoichiometries n of the ISS. In the phase diagrams in Figure 5.5 the grey line corresponds to an isodiffusion line with $D\sqrt{\beta m_\mathrm{L}}/\sigma_\mathrm{L}$=0.05 for the small particles, where m_L is the mass of the large colloid. This line indicates approximately when the small particles become mobile (see Figure 5.5). Surprisingly we find that the diffusion

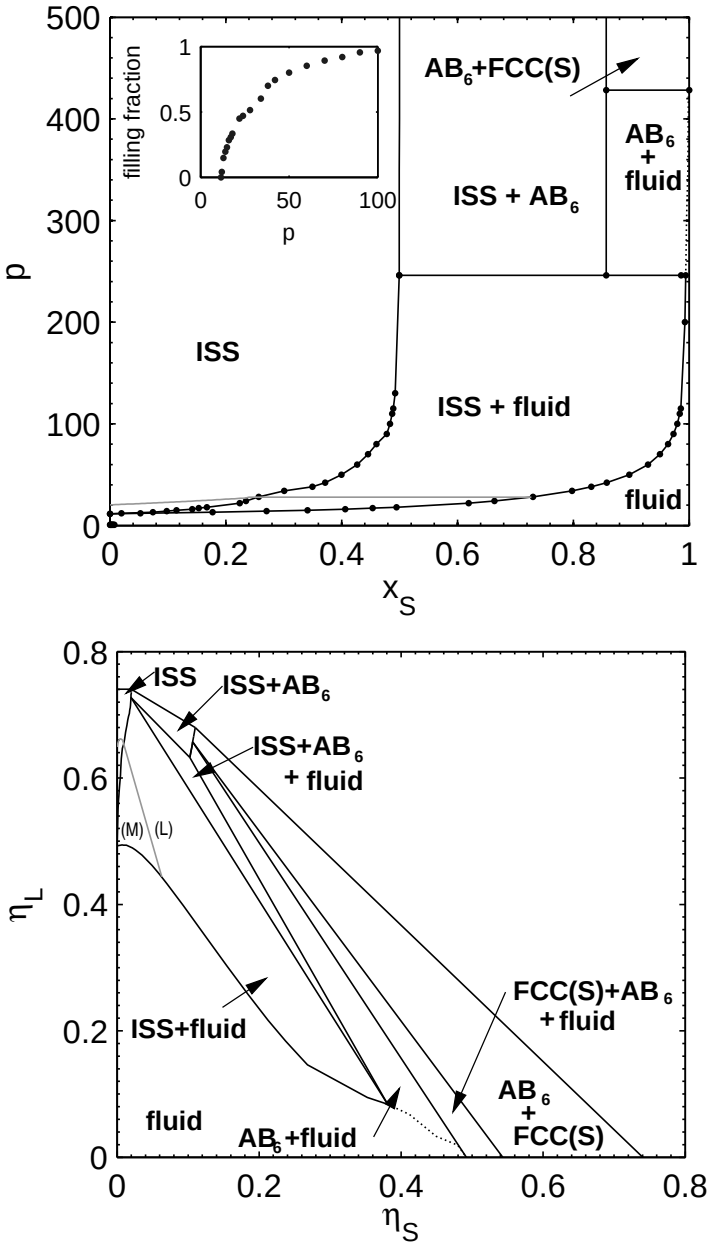

Figure 5.5: Phase diagrams for binary hard-sphere mixtures with size ratio q =0.3. Top: Phase diagram of a binary hard-sphere mixture in the composition $x_s = N_S/(N_S + N_L)$-reduced pressure $p = \beta P\sigma^3$ plane. The interstitial solid solution is denoted by ISS, FCC(S) denotes a face-centered cubic crystal of the small spheres. The tie lines that connect the coexisting phases are horizontal in this representation. The grey (green in colour) line indicates an isodiffusion line for the small particles with $D\sqrt{\beta m_{\rm L}}/\sigma_{\rm L}$=0.05 corresponding approximately to the point where the fluid of small particles in the ISS crystal solidifies. This line is only an approximation as for all finite pressures the particles can move around on a long time scale. It should be noted that this line is not horizontal inside the ISS regime and the isodiffusion line increases slightly as a function of the concentration. Inside the coexistence area the line is horizontal. Inset: The filling fraction, i.e. stoichiometry n, of the octahedral holes with small spheres of the coexisting ISS phase as a function of the pressure. Bottom: Corresponding phase diagram in the η_S-η_L representation.

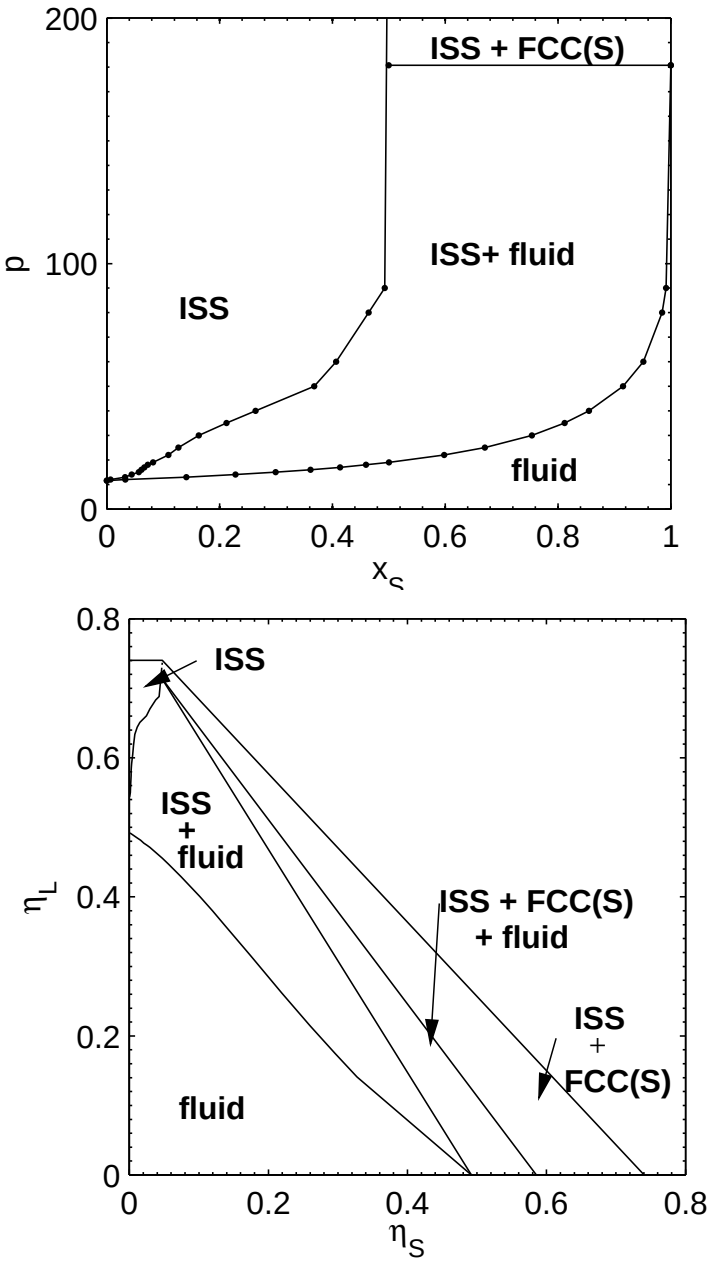

Figure 5.6: Phase diagrams for binary hard-sphere mixtures with size ratio q =0.4. Top: Phase diagram of a binary hard-sphere mixture in the composition $x_s = N_S/(N_S + N_L)$-reduced pressure $p = \beta P \sigma^3$ plane. The interstitial solid solution is denoted by ISS, FCC(S) denotes a face-centered cubic crystal of the small spheres. The tie lines are horizontal in this representation. Bottom: Corresponding phase diagram in the η_S-η_L representation.

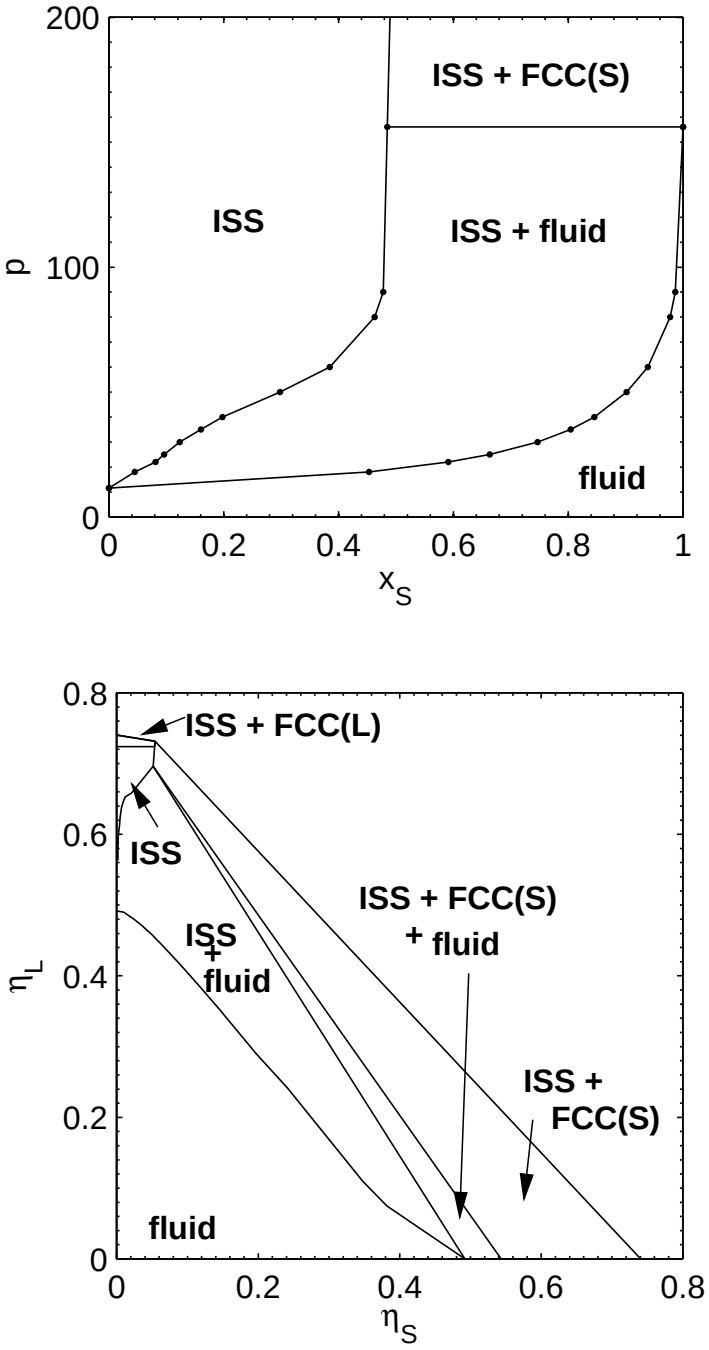

Figure 5.7: Phase diagrams for binary hard-sphere mixtures with size ratio q =0.42. Top: Phase diagram of binary hard-sphere mixture in the composition $x_s = N_S/(N_S + N_L)$-reduced pressure $p = \beta P\sigma^3$ plane. The interstitial solid solution is denoted by ISS, FCC(S) denotes a face-centered cubic crystal of the small spheres and FCC(L) denotes a face-centered-cubic crystal of the large spheres. The tie lines are horizontal in this representation. Bottom: Corresponding phase diagram in the η_S-η_L representation.

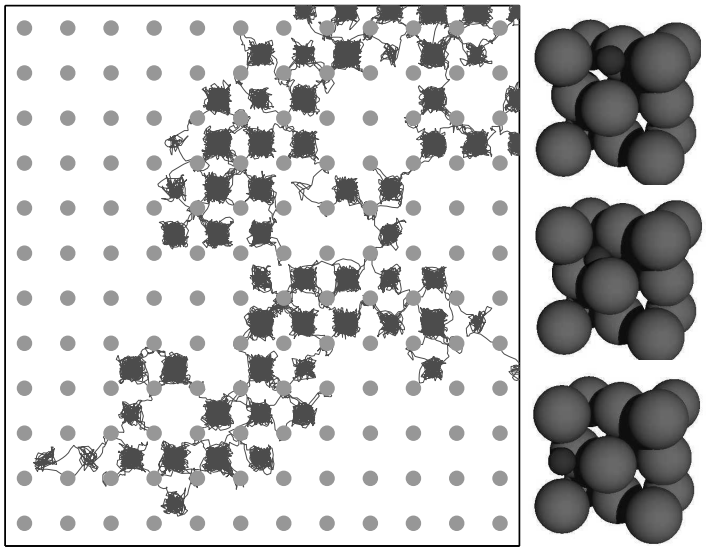

Figure 5.8: Single small particle hopping. On the left is the trajectory of a single particle for a volume fraction of the large particles $\eta_L = 0.6$. Note that none of the lines connecting the lattice sites are either vertical or horizontal indicating that the small particle does not take the direct route between neighbouring holes, but rather hops first to a tetrahedral hole, and then to an octahedral hole. A cartoon demonstrating this process is shown on the right.

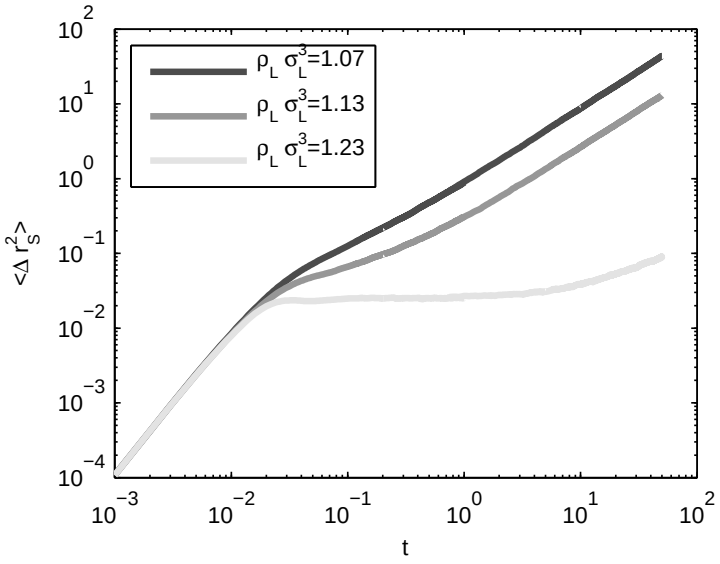

Figure 5.9: Caging of small particles in an interstitial solid solution. Using event driven MD simulations with $N_L = 256$ large particles and stoichiometry $n = 0.5$ we measured the mean square deviation $\langle \Delta r_S^2 \rangle = \langle (\mathbf{r}_S(t) - \mathbf{r}_S(0))^2 \rangle$ of the small particles as a function of time for various number densities of the large particles ρ_L. Note that $r_S(t)$ denotes the small particle coordinate at time t. Here we plot the $\langle \Delta r_S(t)^2 \rangle$ vs time (in MD units) on a log-log scale. As ρ_L increases the subdiffusive regime also increases.

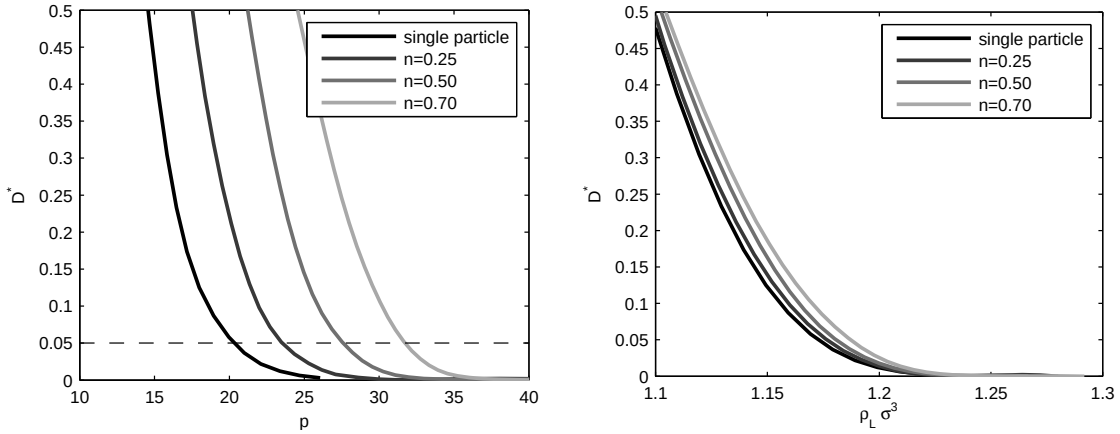

Figure 5.10: Long-time diffusion coefficient $D^* = D\sqrt{\beta m_L}/\sigma_L$ of small particles in an interstitial solid solution. Left: Long-time diffusion coefficient $D^* = D\sqrt{\beta m_L}/\sigma_L$ as a function of the reduced pressure $p = \beta P \sigma^3$ for various interstitial solid solution stoichiometries. The diffusion coefficient D^* was obtained from mean square displacement $\langle \Delta r_S^2(t) \rangle = \langle (\mathbf{r}_S(t) - \mathbf{r}_S(0))^2 \rangle$ calculations using event driven MD simulations (see Figure 5.9). Note that $\mathbf{r}_S(t)$ denotes the small particle coordinate at time t. The dashed black line corresponds to $D^* = D\sqrt{\beta m_L}/\sigma_L = 0.05$ indicating approximately the crossover from mobile interstitials to frozen interstitials. Right: Long-time diffusion coefficient D^* as a function of the number density of large particles ($\rho_L \sigma_L^3$) for various interstitial solid solution stoichiometries n. Note that the diffusion coefficient increases with stoichiometry n.

coefficient increases as we increase the ISS stoichiometry if we keep $\rho_L \sigma_L^3$ fixed. This is in contrast to most systems where the diffusion constant decreases with density; in general as the density increases the available space in the system decreases leaving less room for particles to move resulting in a lower diffusion constant. To explore possible explanations for this behaviour we determined the attractive depletion potential experienced by the large particles due to the presence of the small particles. As shown in Figure 5.11, the depth of this depletion potential increases as the chemical potential of small particles increases. As a result, the mean square deviation of the large particles from their ideal lattice sites increases (Figure 5.12) thereby making more space for the small particles to diffuse. As a consequence, the free-energy barrier heights decrease with stoichiometry n of the ISS as shown in Figure 5.13 which explains the increase in the long-time diffusion coefficient of the small particles with increasing n as shown in Figure 5.10.

Note that the free-energy barriers were determined by mapping each small particle coordinate to the closest position on the line connecting the ideal lattice positions of an octahedral hole with a tetragonal hole and then determining the normalized probability ($P(x)$) of finding a small particle at position x along that line. The free-energy barrier is then given by $\beta U(x) = -\log P(x)$ (see e.g. Ref. [93]).

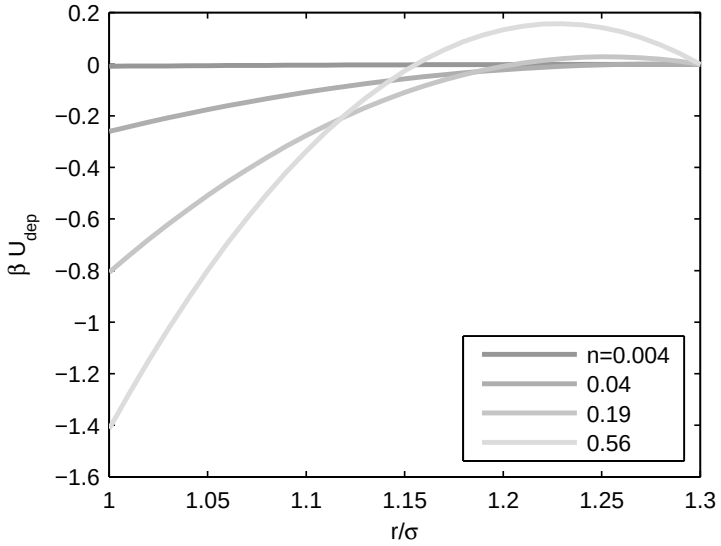

Figure 5.11: Depletion potential for various ISS stoichiometries $n = 0.004, 0.04, 0.19$ and 0.56 with $\rho_L = 1.2$ corresponding to bulk chemical potentials of the small particles $\beta\mu_S = -2.48, 1.34, 3.24, 4.97, 5.70$ and 6.38. The depletion potential was determined using an expression taken from Ref. [92]. Note that depth of the depletion interaction increases from 0 k_BT to 1.4 k_BT as n increases from 0.004 to 0.56.

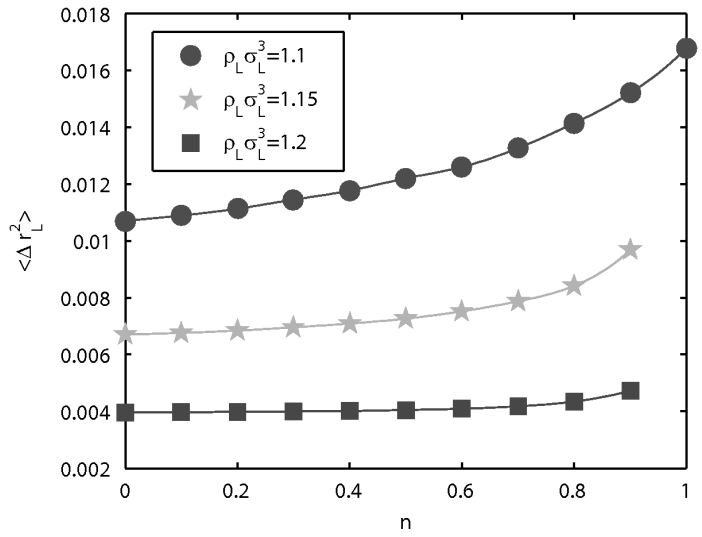

Figure 5.12: Mean square deviation of large particles from their ideal lattice sites as a function of ISS stoichiometry n for large particle number densities ρ_L as labelled. The mean square deviations, $< \Delta r_L(t) >= \left\langle (\mathbf{r}_L(t) - \mathbf{r}_L^{\mathrm{id}})^2 \right\rangle$ with $\mathbf{r}_L^{\mathrm{id}}$ the ideal lattice positions of the large particles, were determined using an Monte Carlo simulation with $N_L = 864$ large particles and correcting for the center of mass motion of the large particles.

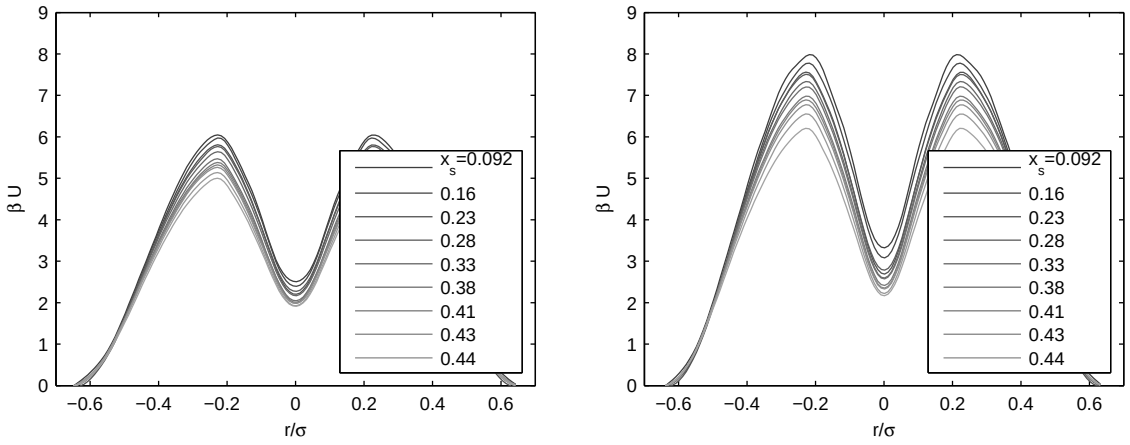

Figure 5.13: Free-energy barriers in an interstitial solid solution felt by small particles hopping from an octahedral hole to a tetragonal hole and back to an octahedral hole at number densities of the large particles of $\rho_L\sigma = 1.1$ (left) and $\rho_L\sigma = 1.2$ (right). The barriers have been determined for a range of small particle compositions, $x_S = N_S/(N_L + N_S)$ where $N_S(L)$ is the number of small (large) particles respectively. Note that the height of the free energy barriers decreases as a function of x_S.

5.4 Experimental realization of an interstitial solid solution

The structural and thermodynamic properties of a system under gravity at a certain height are identical to those of a bulk system at the corresponding pressure. Therefore, sedimentation experiments are often used in scanning the properties of a system over large pressure ranges in just a single experiment [94, 95]. As an illustration of the experimental accessibility of the ISS phase, we performed sedimentation experiments using core-shell silica colloids. The experiments were performed with large 1.4 μm core shell silica colloids. The core was dyed with fluorescein isothiocyanate (FITC) and the core diameter was 0.4 μm [96]. The small colloids had a rhodamine isothiocyanate (RITC) dyed core with a diameter of 0.37 μm and a total diameter of 0.42 μm [51]. The large colloids had a polydispersity of 2% and the small colloids a polydispersity of 7%. The solvent was an index matched mixture of 80% (volume percent) dimethylsulfoxide (DMSO) and water. The size of the domains was increased using an AC electric field of 100 V/mm which was turned off after the particles had sedimented.

Typical snapshots obtained by confocal microscopy from various samples are shown in Figure 5.14. The confocal images depict experimental realizations of ISSs for stoichiometries of approximately $n \simeq 0.1$, 0.3 and 0.8. The stoichiometry of small particles decreases as a function of height in the sample as shown in Figure 5.15. This is in qualitative agreement with the phase diagram (Figure 5.5) which predicts an increasing concentration of small particles with pressure. The confocal images and height profile demonstrate not only the existence of the ISS in this system, but the large range over which the filling of the ISS can be tuned. Furthermore, in examining the motion of the small particles using confocal microscopy, we noted some small particles near the top of the sample moving

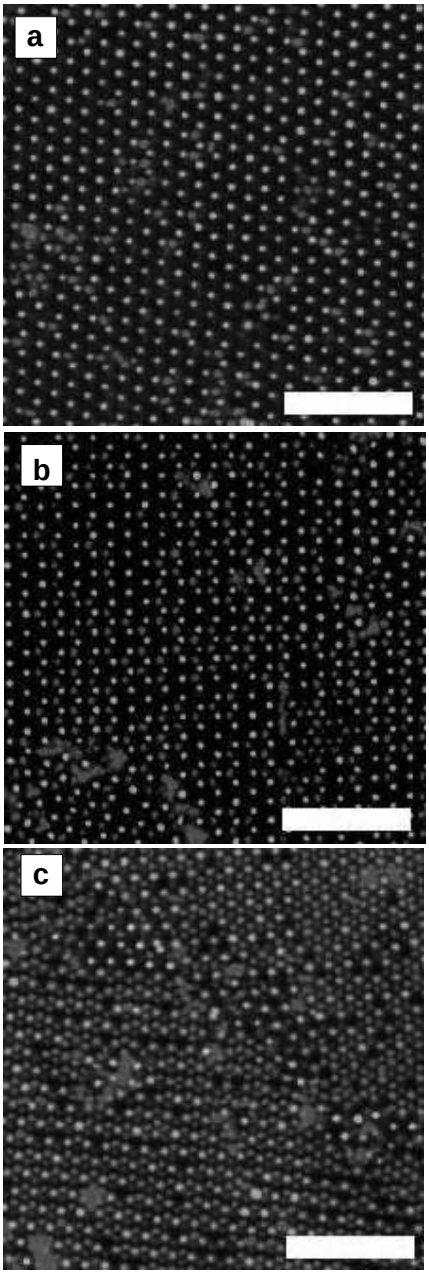

Figure 5.14: Colour version on page 124. Confocal images of an interstitial solid solution with size ratio $q = 0.3$ for various stoichometries. The labels **a**, **b**, and **c** correspond to confocal images of the ISS with $n \simeq 0.1$, 0.3 and 0.8, respectively. In these images two (111) planes of the crystal, one consisting of mostly small (red) particles with the other consisting of mostly large (green) particles have been overlayed in order to be viewable in the same figure. The larger and darker red regions correspond to defects, such as vacancies, in the underlying lattice of green particles which have been filled by many small (red) particles. Scalebars are 10 μm.

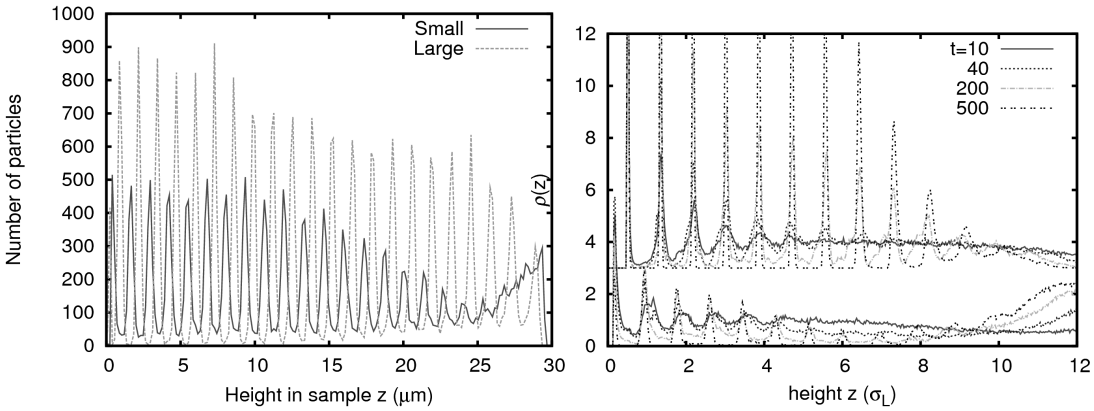

Figure 5.15: Experimental and theoretical density profiles of small and large particles as a function of height in the sample. Left: For z >25 μm, the experimental density profiles show pronounced layering of the fluid of large spheres, while for z <25 μm an interstitial solid solution is seen. Note that the peaks of the solid lines are always found between dashed peaks indicating the small and large particles are in different layers. Right: Theoretical number density profiles determined using event driven MD simulations. The time is as indicated and is measured in MD units ($\sigma_{\mathrm{L}}\sqrt{\beta m_{\mathrm{L}}}$). The number density of the large particles is shifted up by 3 for clarity. Note that the layered structure forming in time agrees well with the experimental density profile.

between interstitial lattice sites. Near the bottom of the sample, this was not observed.

5.5 Discussion

The phase behaviour of this system can be examined in the context of previous experimental and theoretical studies of binary hard-sphere mixtures. In an attempt to grow NaCl crystals, Vermolen *et al.* examined various methods for producing binary NaCl hard-sphere crystals including gravitational and electric fields, epitaxial templates, and dielectrophoretic compression from a binary mixture with relative size ratio 0.3 [51]. However the crystal structures they found all included a significant number of vacancies of the small colloids (>10%). This result is in keeping with the phase behaviour observed in Figure 5.5. Hunt *et al.* also examined binary hard-sphere mixtures of particles with size ratio 0.39 and 0.42 and reported the presence of NaCl [28]. However, from their presented results it is impossible to distinguish between an ISS and an NaCl crystal. On the theoretical side, the closest size ratios examined in literature using full free-energy calculations, are the phase diagrams presented for binary hard-sphere mixtures with $q = 0.2$ [14] and 0.414 [15]. For $q = 0.2$, the phase behaviour is expected to be significantly different than that for $q = 0.3$ as the small particles can fit in both the tetragonal and octahedral holes. However, the phase behaviour for a binary hard-sphere mixture with $q = 0.414$ is likely to be qualitatively the same as that of $q = 0.40$. In both cases, the smaller particles both fit and are restricted to reside in the octahedral holes. MD snapshots included in Ref. [15] for the $q = 0.414$ mixture show a coexistence between a solid and fluid phase which the authors identified as a monodisperse FCC phase and a binary liquid phase. However, the

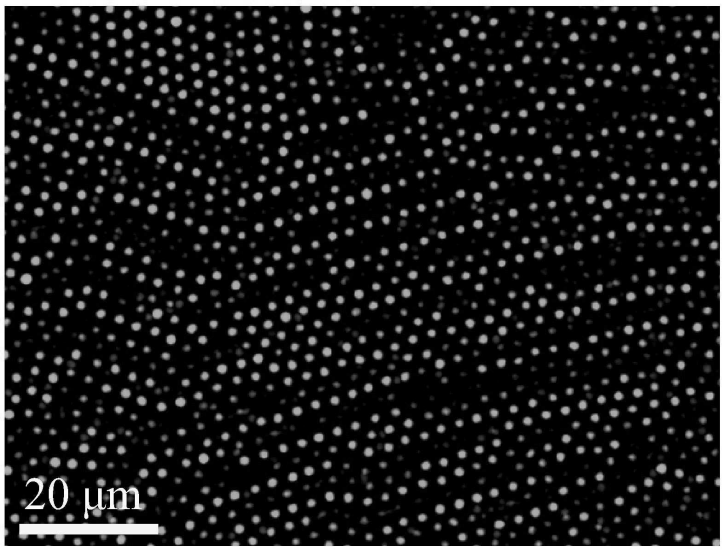

Figure 5.16: Colour version on page 125. Typical confocal image of the ISS structure found in a binary system of oppositely charged PMMA particles with size ratio σ_S/σ_L=0.73 dispersed in a mixture of 23.7 wt% cis-decahydron aphthalene and 76.3 w% cyclohexylbromide. The large (green) and small (red) particles have a diameter 1.88 μm (polydispersity 3 %) and 1.37 μm (polydispersity 5 %) respectively. The overall packing fraction was $\eta = 0.2$. The large particles mutually repel each other and formed a crystal lattice. The small particles were found on random positions in between the lattice. See Figure 5.17 for more details.

FCC phase depicted in their snapshots contains some small particles, and is more likely an ISS phase. To summarize, the NaCl phases previously identified experimentally [51] and theoretically [15] were most likely ISSs. It is, however, impossible to determine the identity of the phase from Ref. [28].

5.6 Conclusion

In conclusion, we present a simple model system for the study of ISSs. We show, with simulations and experiments, the self-assembly of a binary hard-sphere mixture into an ISS phase. We emphasize that the concentration of small particles in the ISS phase is completely tunable from a monodisperse FCC lattice to a binary NaCl lattice. We point out that this phase has likely been seen and was not recognized in previous experimental and theoretical work (e.g. Refs. [15, 51]). Additionally, we remark that there are a vast number of other colloidal and nanoparticle systems which may form an ISS phase. In particular we have found an FCC-based ISS phase in binary mixtures of oppositely charged colloids (Figures 5.16 and 5.17). However, we would also expect some binary mixtures of charged colloids to form body-centered-cubic (BCC) based ISSs in charged systems since the BCC lattice is also stable for monodisperse particles interacting via a Yukawa potential. Hence ISS phases should be considered an important class of crystal structures in interpreting and predicting the phase behaviour seen in colloidal and nanoparticle mixtures. In this work we have examined the diffusion of the small particles; this can

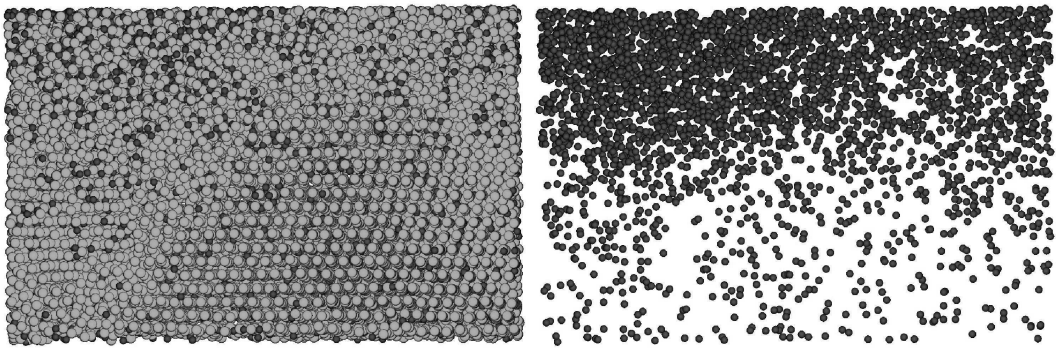

Figure 5.17: Colour version on page 126. 3-D reconstruction of an interstitial solid solution in a binary mixture of oppositely charged colloids. Left: Rendered 3-D reconstruction from a stack of 244 confocal images with a spacing of 0.25 μm between them corresponding to the system described in Figure 5.16. We identified a face-centred-cubic lattice of the mutually repelling large particles with a lattice parameter for the cubic unit cell of $a \approx 3.8$ μm. In the lower part of the sample an ISS was formed with a fluid on top of it. Whereas the large particles do not touch each other, the small particles were found to stick to one or more large particles in the lattice. This, in addition to the observation that the small particles do not appear to occupy a position on the lattice of the large particles demonstrates that the large and small particles were oppositely charged. Right: The same 3-D reconstruction showing only the small particles in the fluid (top) and the ISS (below). We note that in sequential confocal images, some of the small particles were observed hopping from one interstitial site to another.

easily be extended to examine the interaction between any number of equilibrium defects in a crystal, stress fields induced in entropic systems due to defects, binary nucleation of ISSs, and the effect that interstitials have on the photonic and phononic properties of materials. For instance, intriguing photonic colour tuning has been achieved by interstitial doping with absorbing nanoparticles in an FCC photonic crystal [97].

5.7 Acknowledgements

I would like to thank M. Hermes for the experimental results on hard spheres presented in this chapter and J. Hoogenboom and C. Graf for particle synthesis. T. Vissers and J.C.P. Stiefelhagen are thanked for their work on the oppositely charged particles. Additionally, I would like to thank F. Smallenburg and M. Marechal for many fruitful discussions.

6

Crystal nucleation of hard spheres: A numerical study

Over the last number of years several simulation methods have been introduced to study rare events such as nucleation. In this chapter we examine the crystal nucleation rate of hard spheres using three such numerical techniques: molecular dynamics, forward flux sampling and a Bennett-Chandler type theory where the nucleation barrier is determined using umbrella sampling simulations. The resulting nucleation rates are compared with the experimental rates of Harland and Van Megen [J. L. Harland and W. van Megen, Phys. Rev. E **55**, 3054 (1997)], Sinn *et al.* [C. Sinn *et al.*, Prog. Colloid Polym. Sci. **118**, 266 (2001)] and Schätzel and Ackerson [K. Schätzel and B.J. Ackerson, Phys. Rev. E, **48**, 3766 (1993)] and the predicted rates for monodisperse and 5% polydisperse hard spheres of Auer and Frenkel [S. Auer and D. Frenkel, Nature **409**, 1020 (2001)]. When the rates are examined in long-time diffusion units, we find agreement between all the theoretically predicted nucleation rates, however, the experimental results display a markedly different behaviour for low supersaturation. Additionally, we examined the pre-critical nuclei arising in the molecular dynamics, forward flux sampling, and umbrella sampling simulations. The structure of the nuclei appear independent of the simulation method, and in all cases, the nuclei contain on average significantly more face-centered-cubic ordered particles than hexagonal-close-packed ordered particles.

6.1 Introduction

Nucleation processes are ubiquitous in both natural and artificially-synthesized systems. However, the occurrence of a nucleation event is often rare and difficult to examine both experimentally and theoretically.

Colloidal systems are almost ideal model systems for studying nucleation phenomena. Nucleation and the proceeding crystallization in such systems often take place on experimentally accessible time scales, and due to the size of the particles, they are accessible to a wide variety of scattering and imaging techniques, such as (confocal) microscopy [98], holography [99], and light and x-ray scattering. Additionally, progress in particle synthesis [8], solvent manipulation, and the application of external fields [9] allows for significant control over the interparticle interactions, allowing for the study of a large variety of nucleation processes.

One such colloidal system is the experimental realization of "hard" spheres comprised of sterically stabilized polymethylmethacrylate (PMMA) particles suspended in a liquid mixture of decaline and carbon disulfide [100]. Experimentally, the phase behaviour of such a system has been examined by Pusey and Van Megen [90] and maps well onto the phase behaviour predicted for hard spheres. Specifically, when the effective volume fraction of their system is scaled to reproduce the freezing volume fraction of hard spheres ($\eta = 0.495$) the resulting melting volume fraction is $\eta = 0.545 \pm 0.003$ [90] which is in good agreement with that predicted for hard spheres [12]. The nucleation rates have been measured using light scattering by Harland and Van Megen [100], Sinn *et al.* [101], Schätzel and Ackerson [102] and predicted theoretically by Auer and Frenkel [103].

On the theoretical side, hard-sphere systems are one of the simplest systems which can be applied to the study of colloidal and nanoparticle systems, and generally, towards the nucleation process itself. As such, it is an ideal system to examine various computational methods for studying nucleation, and comparing the results with experimental data. Such methods include, but are not limited to, molecular dynamics (MD) simulations, umbrella sampling (US), forward flux sampling (FFS), and transition path sampling (TPS). It is worth noting here that Auer and Frenkel [103] used umbrella sampling simulations to study crystal nucleation of hard spheres and found a significant difference between their predicted rates and the experimental rates of Refs. [100–102]. However, it was unclear where this difference originated. In this chapter we compare the nucleation rates for the hard-sphere system from MD, US and FFS simulations with the experimental results of Refs. [100–102]. We demonstrate that the three simulation techniques are consistent in their prediction of the nucleation rates, despite the fact that they treat the dynamics differently. Thus we conclude that the difference between the experimental and theoretical nucleation rates identified by Auer and Frenkel is not due to the simulation method.

A nucleation event occurs when a statistical fluctuation in a supersaturated liquid results in the formation of a crystal nucleus large enough to grow out and continue crystallizing the surrounding fluid. In general, small crystal nuclei are continuously being formed and melting back in a liquid. However, while most of these small nuclei will quickly melt, in a supersaturated liquid a fraction of these nuclei will grow out. Classical nucleation theory (CNT) is the simplest theory available for describing this process. In CNT it is assumed that the free-energy for making a small nucleus is given by a sur-

face free-energy cost which is proportional to the surface area of the nucleus and a bulk free-energy gain proportional to its volume. More specifically, according to CNT the Gibbs free-energy difference between a homogeneous bulk fluid and a system containing a spherical nucleus of radius R is given by

$$\Delta G(R) = 4\pi\gamma R^2 - \frac{4}{3}\pi \left|\Delta\mu\right| \rho_s R^3 \tag{6.1}$$

where $|\Delta\mu|$ is the difference in chemical potential between the fluid and solid phases, ρ_s is the density of the solid, and γ is the interfacial free-energy density of the fluid-solid interface. This free-energy difference is usually referred to as the nucleation barrier. From this expression, the radius of the critical cluster is found to be

$$R^* = 2\gamma / \left|\Delta\mu\right| \rho_s$$

and the barrier height is

$$\Delta G^* = 16\pi\gamma^3 / 3\rho_s^2 \left|\Delta\mu\right|^2$$

.

Umbrella sampling [104, 105] is a method to examine the nucleation process from which the nucleation barrier is easily obtained. The predicted barrier can then be used in combination with kinetic Monte Carlo (KMC) or MD simulations to determine the nucleation rate [103]. In US an order parameter for the system is chosen and configuration averages for sequential values of the order parameter are taken. In order to facilitate such averaging, the system is biased towards particular regions in configuration space. The success of the method is expected to depend largely on the choice of order parameter and biasing potential (see e.g. [106]). Note that the free-energy barrier is only defined in equilibrium, and thus is only applicable to systems which are in (quasi-) equilibrium.

Forward flux sampling [107–109] is a method of studying rare events, such as nucleation, in both equilibrium and non-equilibrium systems. Using FFS, the transition rate constants (e.g. the nucleation rate) for rare events can be determined when brute force simulations are difficult or even not possible. In FFS, a reaction coordinate Q (similar to the order parameter in US) is introduced which follows the rare event. The transition rate between phase A and B is then expressed as a product of the flux ($\Phi_{A\lambda_0}$) of trajectories crossing the A state boundary, typically denoted λ_0, and the probability ($P(\lambda_B|\lambda_0)$) that a trajectory which has crossed this boundary will reach state B before returning to state A. Thus the transition rate constant is written as

$$k_{AB} = \Phi_{A\lambda_0} P(\lambda_B|\lambda_0). \tag{6.2}$$

Forward flux sampling facilitates the calculation of probability $P(\lambda_B|\lambda_0)$ by breaking it up into a set of probabilities between sequential values of the reaction coordinate. Little information regarding the details of the nucleation process is required in advance, and the choice of reaction coordinate is expected to be less important than the order parameter in US. Additionally, unlike US, FFS utilizes dynamical simulations and hence this technique does not assume that the system is in (quasi-)equilibrium.

Molecular dynamics and Brownian dynamics (BD) simulations are ideal for studying the time evolution of systems, and, when possible, they are the natural technique to

η	$\beta p\sigma^3$	$\beta \lvert\Delta\mu\rvert$	$\rho_s\sigma^3$
0.5214	15.0	0.34	1.107
0.5284	16.0	0.44	1.122
0.5316	16.4	0.48	1.128
0.5348	16.9	0.53	1.135
0.5352	17.0	0.54	1.136
0.5381	17.5	0.58	1.142
0.5414	18.0	0.63	1.148
0.5478	19.1	0.74	1.161
0.5572	20.8	0.90	1.178

Table 6.1: Packing fraction ($\eta = \pi\sigma^3 N/6V$) , reduced pressure ($\beta p\sigma^3$), reduced chemical potential difference between the fluid and solid phases($\beta \lvert\Delta\mu\rvert$) and reduced number density of the solid phase ρ_s of the state points studied in this chapter. The chemical potential difference was determined using thermodynamic integration [20], and the equations of state for the fluid and solid are from Refs. [60, 111] respectively.

study dynamical processes such as nucleation. Unfortunately, available computational time often limits the types of systems which can be effectively studied by these dynamical techniques. Brownian dynamics simulations, which would be the natural choice to use for colloidal systems, are very slow due to the small time steps required to handle the steep potential used to approximate the hard-sphere potential. Event driven MD simulations are much more efficient to simulate hard spheres and enable us to study spontaneous nucleation of hard-sphere mixtures over a range of volume fractions. The main difference between the two simulation methods regards how they treat the short-time motion of the particles. Fortunately, the nucleation rate is only dependent on the long-time dynamics which are not sensitive to the details of the short-time dynamics of the system [110].

In this chapter we study in detail the application of US and FFS techniques to crystal nucleation of hard spheres, and predict the associated nucleation rates. Combining these nucleation rates with results from MD simulations, we make predictions for the nucleation rates over a wide range of packing fractions $\eta = 0.5214 - 0.5572$, with corresponding pressures and supersaturations shown in Table 6.1. We compare these theoretical nucleation rates with the rates measured experimentally by Refs. [100–102].

This chapter is organized as follows: in section 6.2 we discuss the model, in section 6.3 we describe and examine the order parameter used to distinguish between solid- and fluid-like particles throughout this chapter, in section 6.4 we calculate essentially the "exact" nucleation rates using MD simulations, in sections 6.5 and 6.6 we calculate the nucleation rates of hard spheres using US and FFS respectively, and discuss difficulties in the application of these techniques, in section 6.7 we summarize the theoretical results and compare the predicted nucleation rates with the measured experimental rates of Harland and Van Megen [100], Sinn *et al.* [101], and Schätzel and Ackerson [102] and section 6.8 contains our conclusions.

6.2 Model

In this chapter we examine the nucleation rate between spheres with diameter σ which interact via a hard-sphere pair potential given by

$$\beta U^{\mathrm{HS}}(r_{ij}) = \begin{cases} 0 & r_{ij} \geq \sigma \\ \infty & r_{ij} < \sigma. \end{cases} \tag{6.3}$$

where r_{ij} is the center-to-center distance between particles i and j and $\beta = 1/k_B T$ with k_B Boltzmann's constant and T the temperature. This is in contrast to several studies on "hard" spheres where the hard sphere potential is approximated by a slightly soft potential (e.g. Refs. [112, 113]) so that Brownian dynamics simulations or traditional molecular dynamics simulations (i.e. molecular dynamics which is not event driven), which require a continuous potential, can be used. We would like to emphasize this distinction here as the hardness of the interaction has previously been shown to play a significant role in nucleation rates [114, 115]. This point will be further explored in Chapter 8.

6.3 Order parameter

In this chapter, an order parameter is used to differentiate between liquid-like and solid-like particles and a cluster algorithm is used to identify the solid clusters. For this study we have chosen to use the local bond-order parameter introduced by Ten Wolde *et al.* [116, 117] in the study of crystal nucleation in a Lennard-Jones system. This order parameter has been used in many crystal nucleation studies, including a previous study of hard-sphere nucleation by Auer and Frenkel [103].

In the calculation of the local bond order parameter a list of "neighbours" is determined for each particle. The neighbours of particle i include all particles within a radial distance r_c of particle i, and the total number of neighbours is denoted $N_b(i)$. A bond orientational order parameter $q_{l,m}(i)$ for each particle is then defined as

$$q_{l,m}(i) = \frac{1}{N_b(i)} \sum_{j=1}^{N_b(i)} Y_{l,m}(\theta_{i,j}, \phi_{i,j}), \tag{6.4}$$

where $Y_{l,m}(\theta, \phi)$ are the spherical harmonics, $m \in [-l, l]$ and $\theta_{i,j}$ and $\phi_{i,j}$ are the polar and azimuthal angles of the center-of-mass distance vector $\mathbf{r}_{ij} = \mathbf{r}_j - \mathbf{r}_i$ with $\mathbf{r}_i$ the position vector of particle i. Solid-like particles are identified as particles for which the number of connections per particle $\xi(i)$ is at least ξ_c and where

$$\xi(i) = \sum_{j=1}^{N_b(i)} H(d_l(i,j) - d_c), \tag{6.5}$$

H is the Heaviside step function, d_c is the dot-product cutoff, and

$$d_l(i,j) = \frac{\sum_{m=-l}^{l} q_{l,m}(i) q^*_{l,m}(j)}{\left(\sum_{m=-l}^{l} |q_{l,m}(i)|^2 \right)^{1/2} \left(\sum_{m=-l}^{l} |q_{l,m}(j)|^2 \right)^{1/2}}. \tag{6.6}$$

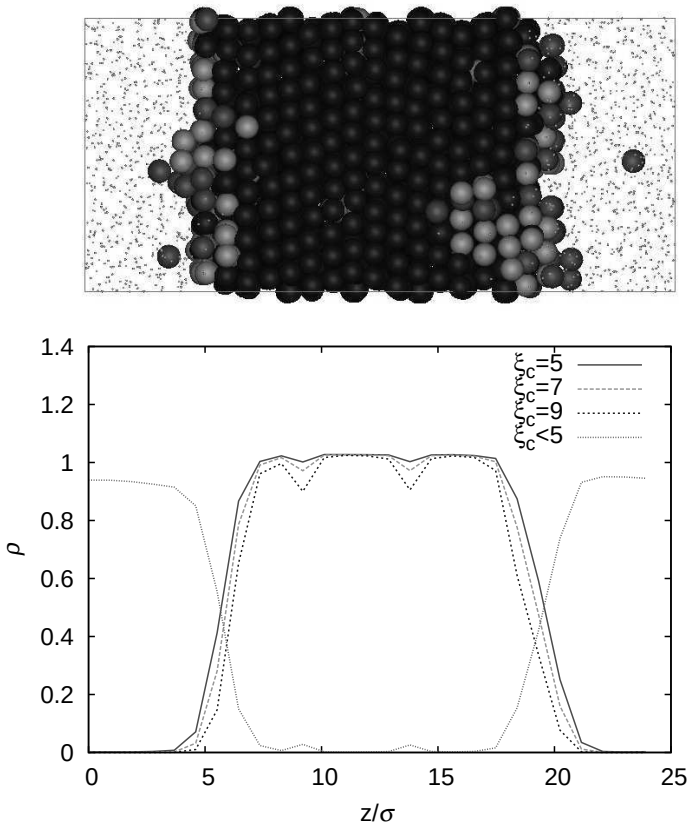

Figure 6.1: Colour version on page 127. Top: A typical configuration of an equilibrated random-hexagonal-close-packed (RHCP) crystal in coexistence with an equilibrated fluid. The crystalline particles are labelled according to three different crystallinity criteria: the red particles have between $\xi = 5$ and 6 crystalline bonds, the green particles have between $\xi = 7$ and 8 crystalline bonds and the blue particles have $\xi \geq 9$ or more crystalline bonds. The fluid-like particles ($\xi < 5$) are denoted by dots. Bottom: The density profile of particles with a minimum number of neighbours ξ as labelled. Note that the dips in the density profile correspond to HCP stacked layers. This implies that near the interface, the order parameter is slightly more sensitive to FCC ordered particles than to HCP ordered particles.

A cluster contains all solid-like particles which have a solid-like neighbour in the same cluster. Thus each particle can be a member of only a single cluster.

The parameters contained in this algorithm include the neighbour cutoff r_c, the dot-product cutoff d_c, the critical value for the number of solid-like neighbours ξ_c, and the symmetry index for the bond orientational order parameter l. The solid nucleus of a hard-sphere crystal is expected to have random hexagonal order, thus the symmetry index is chosen to be 6 in all cases in this study. Note that this order parameter does not distinguish between FCC and HCP ordered particles.

To investigate the effect of the choice of ξ_c, we examined the number of correlated bonds per particle at the liquid-solid interface. To this end, we constructed a configuration in the coexistence region in an elongated box by attaching a box containing an equilibrated random-hexagonal-close-packed (RHCP) crystal to a box containing an equilibrated fluid.

Note that the RHCP crystal was placed in the box such that the hexagonal layers were parallel to the interface. The new box was then equilibrated in an NPT MC simulation. We then examined the density profile of solid-like particles as determined by our order parameter using $r_c = 1.4\sigma$, $d_c = 0.7$ and $\xi_c = 5, 7$ and 9. As shown in Figure 6.1, for all values of ξ_c that we examined the order parameter appears to consistently identify the particles belonging to the bulk fluid and solid regions. For comparison we also show a typical configuration of the RHCP crystal in coexistence with the fluid phase. The solid-like particles, as defined by the order parameter, are labelled according to the number of solid-like neighbours while the fluid-like particles are denoted by dots. The main difference between these order parameters relates to distinguishing between fluid- and solid-like particles at the fluid-solid interface. Unsurprisingly, the location of the interface seems to shift in the direction of the bulk solid as ξ_c is increased. We note that the dips in the density profile correspond to HCP stacked layers which are more pronounced for higher values of ξ_c.

6.4 Molecular dynamics

6.4.1 Nucleation rates

In MD simulations the equations of motion are integrated to follow the time evolution of the system. Since the hard-sphere potential is discontinuous the interactions only take place when particles collide. Thus the particles move in straight lines (ballistic) until they encounter another particle with which they perform an elastic collision [91]. These collision events are identified and handled in order of occurrence using an event driven simulation.

In theory, using an MD simulation to determine nucleation rates is quite simple. Starting with an equilibrated fluid configuration, an MD simulation is used to evolve the system until the largest cluster in the system exceeds the critical nucleus size. The MD time associated with such an event is then measured and averaged over many initial configurations. The nucleation rate is given by

$$k = \frac{1}{\langle t \rangle V} \tag{6.7}$$

where V is the volume of the system and $\langle t \rangle$ is the average time to form a critical nucleus. Measuring this time is relatively easy for low supersaturations where the nucleation times are relatively long compared to the nucleation event itself, which corresponds with a steep increase in the crystalline fraction of the system. However, for high supersaturations pinpointing the time of a nucleation event is more difficult. Often many nuclei form immediately and the critical nucleus sizes must be estimated from CNT or US simulations. Additionally, the precise details of the initial configuration can play a role at high supersaturations since the equilibration time of the fluid is of the same order of magnitude as the nucleation time. Hence, for each individual MD simulation we used a new initial configuration which was created by quenching the system very quickly.

For the results in this chapter, we performed MD simulations with up to 100,000 particles in a cubic box with periodic boundary conditions in an NVE ensemble. Time

was measured in MD units $\sigma\sqrt{m/k_BT}$. The order parameter was measured every 10 time units and when the largest cluster exceeded the critical size by 100 percent we estimated the time $\tau_{\rm nucl}$ at which the critical nucleus was formed using stored previous configurations. We performed up to 20 runs for every density and averaged the nucleation times.

Volume fraction η	Average nucleation time $t\sqrt{k_BT/(m\sigma^2)}$	Rate $k\sigma^5/(6D_l)$
0.5316	$1 \cdot 10^6$	$5{\cdot}10^{-9}$
0.5348	$1.7 \cdot 10^4$	$3.6{\cdot}10^{-7}$
0.5381	$1.4 \cdot 10^3$	$5.3{\cdot}10^{-6}$
0.5414	$2.0 \cdot 10^2$	$4.3{\cdot}10^{-5}$
0.5478	42	$3.0{\cdot}10^{-4}$
0.5572	10	$2.4{\cdot}10^{-3}$

Table 6.2: The average nucleation time, obtained from MD simulations, to form a critical cluster that grew out and filled the box. The last column contains the rate (k) in units of $(6D_l)/\sigma^5$.

The results are shown in Table 6.2. The nucleation times shown here are for a system of $2.0 \cdot 10^4$ particles and are given in MD time units. To compare with other data we convert the MD time units to units of $\sigma^2/(6D_l)$ with D_l the long-time diffusion coefficient measured in the same MD simulations. We were not able to measure the long-time diffusion coefficients for high densities because our measurements were influenced by crystallization. We used the fit obtained by Zaccarelli *et al.* [118] who used polydisperse particles to prevent crystallization. For $\eta < 0.54$, we find good agreement between our data for D_l and this fit.

6.5 Umbrella sampling

6.5.1 Gibbs free-energy barriers

Umbrella sampling is a technique developed by Torrie and Valleau to study systems where Boltzmann-weighted sampling is inefficient [104]. This method has been applied frequently to study rare events, such as nucleation [105], and specifically has been applied in the past to study the nucleation of hard spheres [103]. In general, umbrella sampling is used to examine parts of configurational space which are inaccessible by traditional schemes, e.g. Metropolis Monte Carlo simulations. Typically, a biasing potential is added to the true interaction potential causing the system to oversample a region of configuration space. The biasing potential, however, is added in a manner such that is it easy to "un"-bias the measurables.

In the case of nucleation, while it is simple to sample the fluid, crystalline clusters of larger sizes will be rare, and as such, impossible to sample on reasonable time scales. The typical biasing potential for studying nucleation is given by [116, 119]

$$U_{\rm bias}(n(\mathbf{r}^N)) = \frac{\lambda}{2}(n(\mathbf{r}^N) - n_C)^2, \tag{6.8}$$

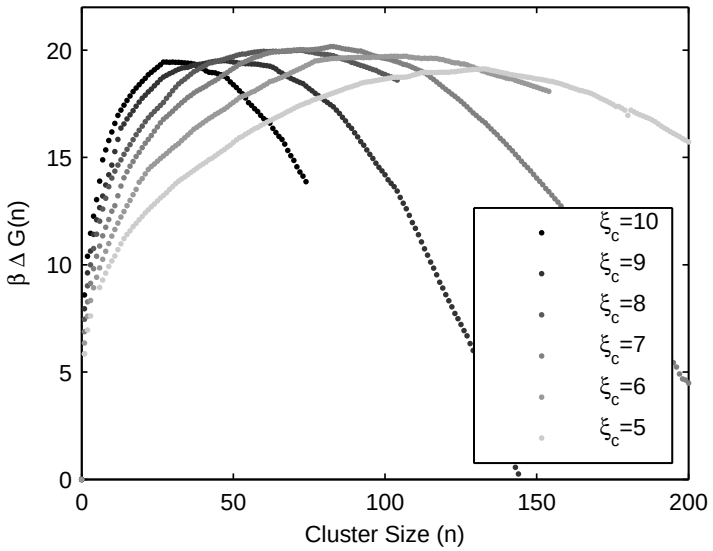

Figure 6.2: Gibbs free-energy barriers $\beta\Delta G(n)$ as a function of cluster-size n as obtained from umbrella sampling simulations at a reduced pressure of $\beta p\sigma^3 = 17$ for varying critical number of solid-like neighbours ξ_c as labelled. For $\xi_c = 5, 7$ and 9, the neighbour cutoff is $r_c = 1.4\sigma$ and for $\xi_c = 6, 8$ and 10, $r_c = 1.3\sigma$. In all cases the dot product cutoff is $d_c = 0.7$.

where λ is a coupling parameter, $n(\mathbf{r}^N)$ is the size of the largest cluster associated with configuration $\mathbf{r}^N$, and n_C is the targeted cluster size. By choosing λ carefully, the simulation will fluctuate around the part of configurational space with $n(\mathbf{r}^N)$ in the vicinity of n_C. The expectation value of an observable A is then given by

$$\langle A \rangle = \frac{\left\langle A/W(n(\mathbf{r}^N)) \right\rangle_{\text{bias}}}{\langle 1/W(n(\mathbf{r}^N)) \rangle_{\text{bias}}} \tag{6.9}$$

where

$$W(x) = e^{-\beta U_{\text{bias}}(x)}. \tag{6.10}$$

Using this scheme to measure the probability distribution $P(n)$ for clusters of size n, the Gibbs free-energy barrier can be determined by [120]

$$\beta\Delta G(n) = \text{constant} - \ln(P(n)). \tag{6.11}$$

Many more details on this method are given elsewhere [20, 120].

For a pressure of $\beta p\sigma^3 = 17$, corresponding to a supersaturation of $\beta\,|\Delta\mu| = 0.54$, we examine the effect of one of the order parameter variables, namely ξ_c, on the prediction of the nucleation barriers. The barriers predicted by US using $\xi_c = 5, 6, 7, 8, 9$ and 10 are shown in Figure 6.2. Note that the height of the barriers does not depend on ξ_c. In general, for larger values of ξ_c more particles are identified as fluid as compared with smaller values of ξ_c. This is consistent with the differences between these order parameters as demonstrated in Figure 6.1. Thus, the radius measured in our simulation will depend on the definition of the order parameter. However, from classical nucleation theory (Eq. 1),

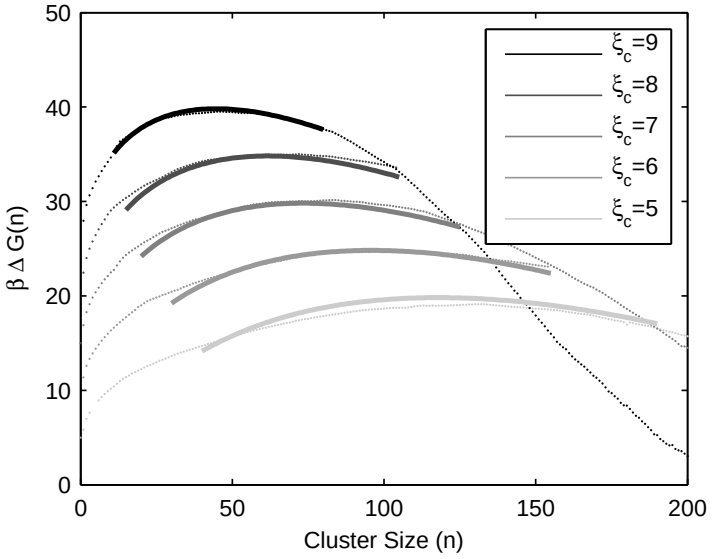

Figure 6.3: Classical nucleation theory fits (thick lines) to the Gibbs free-energy barriers obtained from umbrella sampling simulations at a reduced pressure of $\beta p\sigma^3 = 17$ for varying ξ_c as labelled. Note that the CNT radius (R_{CNT}) is related to the radius ($R(\xi_c)$) measured by umbrella sampling by $R(\xi_c) = R_{\mathrm{CNT}} + \alpha(\xi_c)$, where $\alpha(\xi_c)$ is a constant that corrects for the different ways the various order parameters identify the particles at the fluid-solid interface. The fit parameters are given in Table 6.3. We have shifted the barriers for $\xi_c = 6-9$ by $5, 10, 15$ and $20\ k_BT$ respectively for clarity

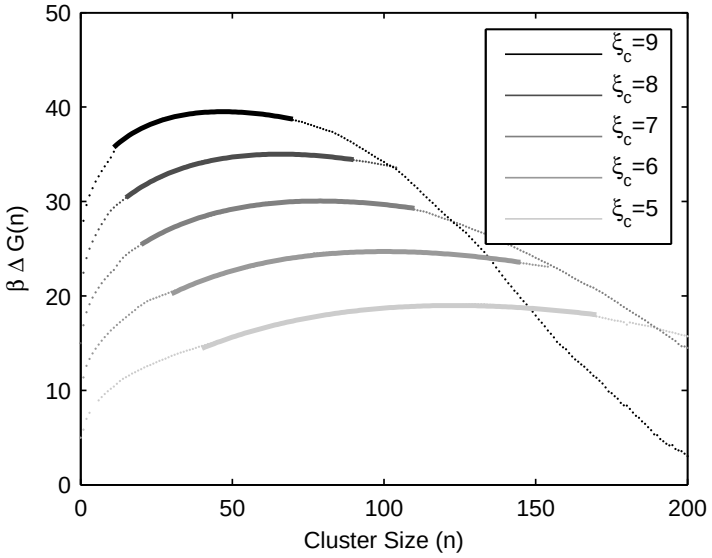

Figure 6.4: Fits of an adjusted classical nucleation theory (ACNT) presented in Section 6.5.1 to the Gibbs free-energy barriers predicted using umbrella sampling simulations at a reduced pressure of $\beta p\sigma^3 = 17$ and for varying ξ_c as labelled. Note that the CNT radius (R_{CNT}) is related to the radius measured by umbrella sampling via $R(\xi_c) = R_{CNT} + \alpha(\xi_c)$, where $\alpha(\xi_c)$ is a constant. The fit parameters are given in Table 6.3. We have shifted the barriers for $\xi_c = 6-9$ by $5, 10, 15$ and $20\ k_BT$ respectively for clarity.

	$\beta\lvert\Delta\mu\rvert$	$\beta\gamma\sigma^2$	R^*_{CNT}							
CNT	0.54	0.76	2.49							
ACNT	0.54	0.63	2.06							
	$\alpha(5)$	$\alpha(6)$	$\alpha(7)$	$\alpha(8)$	$\alpha(9)$	$c(5)$	$c(6)$	$c(7)$	$c(8)$	$c(9)$
CNT	-0.425	-0.231	-0.000	0.139	0.380					
ACNT	-0.879	-0.698	-0.464	-0.335	-0.076	7.80	8.56	8.84	8.87	8.34

Table 6.3: Numerical values for the parameters associated with the fits in Figures 6.3 and 6.4 for classical nucleation theory and the adjusted classical nucleation theory presented in this chapter.

there exists a unique definition of the liquid-solid interface and this a unique radius associated with CNT which we define as R_{CNT}. To a first approximation, for each definition of the order parameter, this radius (R_{CNT}) differs from that measured by our simulation ($R(\xi_c)$) by a constant which we denote as $\alpha(\xi_c)$, which is also dependent on ξ_c. Thus, we fit the barriers corresponding to $\xi_c = 5, 6, 7, 8$ and 9 using CNT where we have

$$R(\xi_c) = R_{\mathrm{CNT}} + \alpha(\xi_c). \tag{6.12}$$

Note that we have assumed that the cluster size n can be related to the cluster radius $R(\xi_c)$ by

$$n(\xi_c) = \frac{4\pi R(\xi_c)^3 \rho_s}{3}. \tag{6.13}$$

Only the top part of the free-energy barriers are expected to fit to classical nucleation theory, so we take the top of the barrier corresponding to the region where the difference between $\beta\Delta G(n)$ and $\beta\Delta G(n^*)$ is approximately 5. Fitting all barriers simultaneously for the interfacial free-energy density γ, the classical nucleation theory radius R_{CNT}, and the various $\alpha(\xi_c)$, we obtain the fits displayed in Figure 6.3. From the various values of α, the associated critical CNT radius (R^*_{CNT}) can be determined. We find $R^*_{\mathrm{CNT}} = 2.49\sigma$. Additionally, we find an interfacial free-energy density of $\beta\gamma\sigma^2 = 0.76$ which roughly agrees with the results of Auer and Frenkel who obtained $\beta\gamma\sigma^2 = 0.699, 0.738$ and 0.748 for pressures $\beta p\sigma^3 = 15, 16$ and 17 respectively [103]. However, recent calculations by Davidchack *et al.* [121] of γ at the fluid-solid coexistence find $\beta\gamma\sigma^2 = 0.574, 0.557$ and 0.546 for the crystal planes (100), (110), and (111) respectively. For a spherical nucleus, γ is expected to be an average over the crystal planes and was found to be $\beta\gamma\sigma^2 = 0.559$ [121]. Thus our result for γ and that of Ref. [103] appear to be an overestimate.

There have been a number of papers discussing possible corrections to CNT (eg. Refs. [122, 123]). Recent work on the 2d Ising model, a system where both the interfacial free-energy density and supersaturation are known analytically, demonstrated that in order to match a nucleation barrier obtained from US to CNT, two correction terms were required, specifically a term proportional to $\log(N)$ as well as a constant shift in ΔG which we define as c. [122] The US barrier is only expected to match CNT near the top of the barrier where the $\log(N)$ term is almost a constant. Thus, we propose fitting the barrier to an adjusted expression for CNT (ACNT), by adding a constant c to Eq. 1. Fitting the US barriers with this proposed form for the Gibbs free-energy barrier, where we assume c is a

function of ξ_c, we obtain the fits displayed in Figure 6.4. In this case we find an interfacial free-energy density $\beta\gamma\sigma^2 = 0.63$, and the values for $\alpha(\xi_c)$ and $c(\xi_c)$ are given in Table 6.3. We note that this fit is much better than the fits in Figure 6.3. The difference in the various $c(\xi_c)$ are around $1k_BT$ and correspond well to the difference in heights of the barriers. More strikingly, the interfacial free-energy density predicted from this proposed free-energy barrier is in much better agreement with recent calculations of Davidchack *et al.* [121], than the interfacial free-energy density we calculate using classical nucleation theory directly. We would also like to point out that it has been proposed that the effective interfacial free energy density will increase with pressure. However, an increase from the $\beta\gamma\sigma^2 = 0.559$ at coexistence predicted by Ref. [121] to $\beta\gamma\sigma^2 = 0.76$ predicted from CNT is larger than what would be expected (see e.g. Refs. [124, 125]). For a more thorough examination on the interfacial free-energy densities of the hard sphere model, see Ref. [125]. We would like to point out here that due to the simple form of the nucleation barrier, it is difficult to be certain of any fit with more than one fitting parameter, as there are many combinations of parameters which fit almost equally well. To examine in more detail the accuracy of these fits, we have calculated the root mean square of the residual for the two fits which we denote as σ_{RMSR}. In the case of the CNT fit we find $\sigma_{\mathrm{RMSR}} = 0.50$ while for the ACNT fit we find $\sigma_{\mathrm{RMSR}} = 0.11$ indicating that the ACNT fit is much better than the CNT fit. Additionally, we examined the ACNT fits for various interfacial free-energy densities γ. Fixing the interfacial free-energy density in the ACNT fit to the value found by CNT ($\beta\gamma\sigma^2 = 0.76$), we find $\sigma_{\mathrm{RMSR}} = 0.27$ and when we use interfacial free-energy density at coexistence [121] ($\beta\gamma\sigma^2 = 0.559$) we find $\sigma_{\mathrm{RMSR}} = 0.18$.

Using either expressions for the Gibbs free-energy barrier, namely CNT and ACNT, we were unable to fit the barrier corresponding to $\beta p\sigma^3 = 17$ and $\xi_c = 10$ simultaneously with the other predicted barriers for the same pressure. We speculate that our difficulty in fitting the barrier at $\xi_c = 10$ stems from an "over-biasing" of the system. Specifically, using $\xi_c = 10$ the biasing potential could cause the system to sample more ordered clusters more frequently, and hence change slightly the region of phase space available to the US simulations. In general, the least biased systems would be expected to explore the largest region of phase space resulting in the best results. It should be noted that, in fact, this problem is simply an equilibration and measuring problem, but it does emphasize the difficulty caused by using an overly strong biasing potential.

In conclusion, with the exception of $\xi_c = 10$, the value of ξ_c used in the order parameter did not appear to have an effect on the nucleation barriers once the difference in their measurements of the solid-liquid interface was taken into consideration. Finally, for use in our nucleation rate calculations (section 6.5.2) we also determined the Gibbs free-energy $\Delta G(n)$ for reduced pressures $\beta p\sigma^3 = 15$ and 16 using umbrella sampling simulations. We present the barrier heights in Table 6.4.

6.5.2 Umbrella sampling nucleation rates

The nucleation barriers as obtained from US simulations can be used to determine the nucleation rates. The crystal nucleation rate k is related to the free-energy barrier ($\Delta G(n)$) by [103]

$$k = Ae^{-\beta\Delta G(n^*)}, \tag{6.14}$$

where

$$A \approx \rho f_{n^*} \sqrt{\frac{|\beta \Delta G''(n^*)|}{2\pi}}, \tag{6.15}$$

n^* is the number of particles in the critical nucleus, ρ is the number density of the supersaturated fluid, f_{n^*} is the rate at which particles are attached to the critical cluster, and $\Delta G''$ is the second derivative of the Gibbs free-energy barrier. Auer and Frenkel [103] showed that the attachment rate f_{n^*} could be related to the mean square deviation of the cluster size at the top of the barrier by

$$f_{n^*} = \frac{1}{2} \frac{\langle \Delta n^2(t) \rangle}{t}. \tag{6.16}$$

The mean square deviation (MSD) of the cluster size $\Delta n^2(t) = \langle (n(t) - n^*)^2 \rangle$ can then be calculated by either employing a kinetic MC simulation or a MD simulation at the top of the barrier. For simplicity, in the remainder of this chapter the nucleation rate determined using this method will be referred to as the umbrella sampling (US) nucleation rate, although to calculate the nucleation rates both US simulations and dynamical simulations (KMC or MD) are necessary.

The mean square deviation, or variance, in the cluster size appearing in Eq. 6.16 has both a short- and long-time behaviour. At short times, fluctuations are due to particles performing Brownian motion around their average positions while the long-time behaviour is caused by rearrangements of particles required for the barrier crossings. The slope of the variance is large at short times where only the fast rattling is sampled. However, the longer the time the further the system has diffused away from the critical cluster size at the top of the nucleation barrier. Auer [126] states that runs need to be selected that remain at the top of the barrier. However, when this is done the attachment rate is lower than when the average over all runs is taken since it excludes the runs that move off the barrier fast and have the largest attachment rate. This problem is analogous to determining the diffusion constant of a particle performing a random walk. By only including walks which remain in the vicinity of the origin, the measurement is biased and excludes trajectories which quickly move away from the origin. This results is an underestimation of the diffusion constant, and similarly, in this case, an underestimate of the attachment rate. Hence, in this chapter we do not attempt to prevent the trajectories from falling off the barrier and we include all trajectories. In Figure 6.5 we demonstrate how, starting from a critical cluster, the size of the nucleus fluctuates as a function of time and, in fact, can completely disappear or double in size within $0.3\tau_l$. Note that τ_l is the time that it takes a particle on average to diffuse over a distance equal to its diameter i.e. $\tau_l = \sigma^2/(6D_l)$.

The kinetic prefactor was determined using KMC simulations with 3000 particles in an NVT ensemble in a cubic box with periodic boundary conditions. The initial configurations were taken from US simulations in one of the windows at the top of the barrier. We examined the results from both Gaussian and uniformly distributed Monte Carlo steps and found agreement within the statistical errors. For all the simulations, the MC step size was between 0.01σ and 0.1σ. The variance of the cluster size for a typical system is shown in Figure 6.6. We observed a large variance in the attachment rates calculated for different nuclei. Specifically, some nuclei have attachment rates more than an order

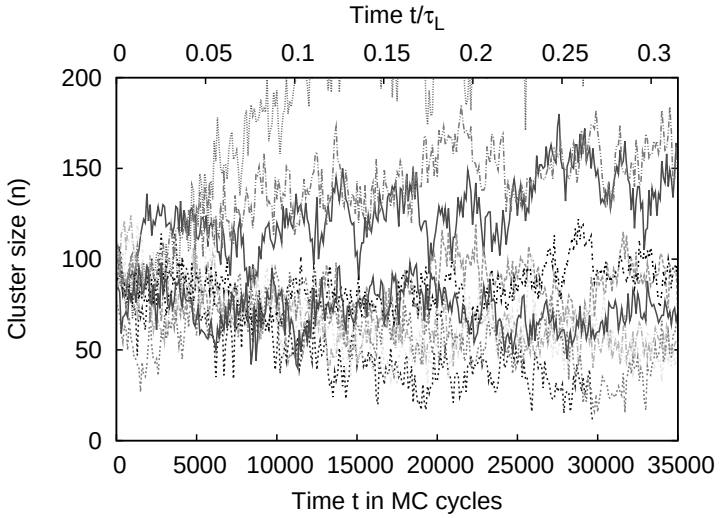

Figure 6.5: The cluster size ($n(t)$) as a function of time in MC cycles for a random selection of clusters that start at the top of the nucleation barrier.

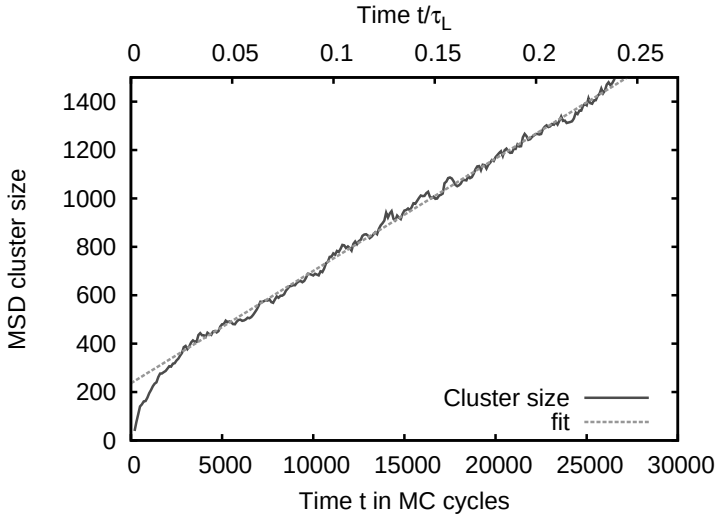

Figure 6.6: The mean squared deviation (MSD) of the cluster size $\langle \Delta n^2(t) \rangle$ as function of time t in MC cycles. The cluster size has been measured every cycle and averaged over 100 cycles to reduce the short-time fluctuations. The slope of this graph is twice the attachment rate (Eq. 6.16).

$\beta p\sigma^3$	ξ_c	n^*	$\beta\Delta G(n^*)$	$\beta\Delta G''(n^*)$	f_{n^*}/D_0	$k\sigma^5/D_0$
15	8	212	42.1 ± 0.2	$-9.6 \cdot 10^{-4}$	661.4	$4.35 \cdot 10^{-18}$
16	8	112	27.5 ± 0.6	$-1.6 \cdot 10^{-3}$	429.1	$7.80 \cdot 10^{-12}$
17	6	102	19.6 ± 0.3	$-1.2 \cdot 10^{-3}$	712.9	$3.08 \cdot 10^{-8}$
17	8	72	20.0 ± 0.4	$-2.0 \cdot 10^{-3}$	469.8	$1.77 \cdot 10^{-8}$
17	10	30	19.4 ± 0.7	$-9.4 \cdot 10^{-3}$	316.1	$4.49 \cdot 10^{-8}$

Table 6.4: Nucleation rates k in units of D_0/σ^5 with D_0 the short time diffusion coefficient as a function of reduced pressure ($\beta p\sigma^3$) as predicted by umbrella sampling. $\Delta G''(n^*)$ is the second order derivative of the Gibbs free-energy at the critical nucleus size n^*.

of magnitude higher than other nuclei of similar size. The nuclei with low attachment rates appeared to have a smoother surface than the nuclei with a high attachment rate. In calculating the attachment rates we used 10 independent configurations on the top of the barrier and followed 10 trajectories from each.

Our results for the kinetic prefactors and nucleation rates for pressures $\beta p\sigma^3 = 15, 16$ and 17 are reported in Table 6.4.

6.6 Forward flux sampling

6.6.1 Method

The forward flux sampling method was introduced by Allen *et al.* [107] in 2005 to study rare events and has since been applied to a wide variety of systems. Two review articles (Refs. [127, 128]) on the subject have appeared recently and provide a thorough overview of the method. In the present chapter we discuss FFS as it pertains to the liquid to solid nucleation process in hard spheres. In general, FFS follows the progress of a reaction coordinate during a rare event. For hard-sphere nucleation, a reasonable reaction coordinate (Q) is the number of particles in the largest crystalline cluster in the system (n). For the remainder of this chapter, for all FFS calculations, we take the reaction coordinate to be the order parameter discussed in Sec. 6.3 with $\xi_c = 8$, $r_c = 1.3\sigma$, and $d_c = 0.7$. In general, the reaction coordinate is used to divide phase space by a sequence of interfaces (λ_0, λ_1, ... λ_N) associated with increasing values $n(\mathbf{r}^N)$ such that the nucleation process between any two interfaces can be examined (see Figure 6.7). In our case the liquid is composed of all states with $n < \lambda_0$ and the solid contains all states with $n > \lambda_N$. While the complete nucleation event is rare, the interfaces are chosen such that the part of the nucleation process between consecutive interfaces is not rare, and can thus be thoroughly studied.

In the FFS methodology, the nucleation rate from the fluid phase A to the solid phase B is given by

$$k_{AB} = \Phi_{A\lambda_0} P(\lambda_N|\lambda_0) \tag{6.17}$$

$$= \Phi_{A\lambda_0} \prod_{i=0}^{N-1} P(\lambda_{i+1}|\lambda_i), \tag{6.18}$$

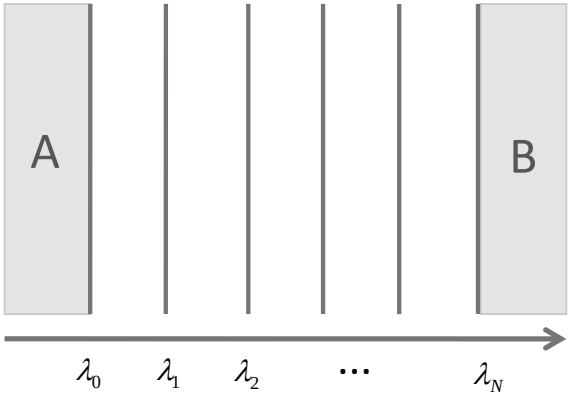

Figure 6.7: In forward flux sampling, the nucleation event from A to B is followed by a reaction coordinate (λ). As sketched above, the reaction coordinate divides phase space by a sequence of interfaces (λ_i) associated with increasing values of the reaction coordinate. In the case of hard spheres, a reasonable reaction coordinate is the order parameter discussed in Section 6.3.

where $\Phi_{A\lambda_0}$ is the steady-state flux of trajectories leaving the A state and crossing the interface λ_0 in a volume V, and $P(\lambda_{i+1}|\lambda_i)$ is the probability that a configuration starting at interface λ_i will reach interface λ_{i+1} before it returns to the fluid (A). See Figure 6.8 for a sketch depicting this method.

If we apply this method directly to a hard-sphere system a number of difficulties arise. As shown in Figure 6.5, on short times the size of a cluster measured by the order parameter fluctuates wildly. The variance in the cluster size displays two different types of behaviour, short-time fluctuations related to surface fluctuations of the cluster, and a longer time cluster growth (Figure 6.6). Thus, if we try to measure the flux $\Phi_{A\lambda_0}$ directly, we encounter difficulties due to these short-time surface fluctuations. In theory, FFS should be able to handle these types of fluctuations, however, they increase the amount of statistics necessary to properly measure the flux and the first probability window. In the second part of FFS calculations, probabilities of the form $P(\lambda_{i+1}|\lambda_i)$ need to be determined. In calculating these probabilities it is important to be able to determine if a cluster has returned to the fluid (A). For pre-critical clusters we find large fluctuations of the order parameter, as shown in Figure 6.9, which can lead to a cluster being misidentified as the fluid (A). Specifically, in this figure the darkest trajectory (black) shows a cluster containing 43 particles that shrinks to 5 particles before it returns to 40, and finally reaches a cluster size of 60 particles. Hence, if we had set $\lambda_0 = 5$, this trajectory would have been identified as melting back to the fluid phase (A). However, since the growth of a cluster from size 5 to 60 is a rare event in our system, we presume that this was simply a short-time fluctuation of the cluster and not a 'real' melting of the instantaneously measured cluster. For pre-critical clusters, these fluctuations result in cluster sizes that are smaller than the cluster 'really' is. We suggest that these fluctuations are largely related to the difficulty that this order parameter has in distinguishing between solid-

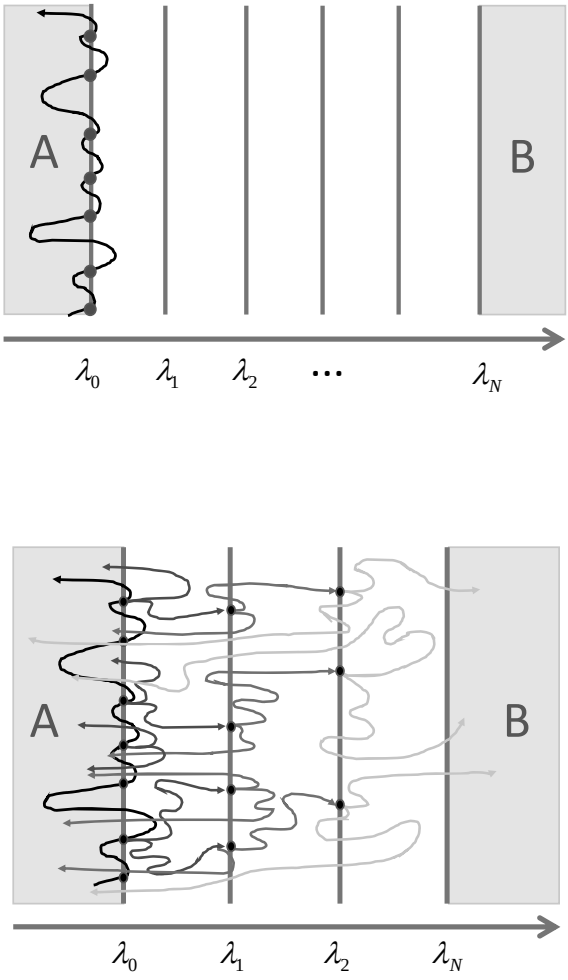

Figure 6.8: Top: In a typical forward flux sampling simulation the flux is calculated by running a simulation in the region A (i.e., in the case of hard spheres, the metastable fluid), and counting the number of times the trajectory crosses the A state boundary in time T. Bottom: A cartoon demonstrating how the probability $P(\lambda_N|\lambda_0)$ is calculated.

and fluid-like particles at the fluid-solid interface. For larger clusters, where the surface to volume ratio is small, this problem is minimal. However, for elongated or rough pre-critical clusters, where the surface to volume ratio is large, these surface fluctuations and rearrangements are important, and can cause problems in measuring the order parameter.

Thus, to try and address these problems, in this chapter, we apply forward flux sampling in a novel way. We regroup the elements of the rate calculation such that

$$k_{AB} = \tilde{\Phi}_{A\lambda_1} \prod_{i=1}^{N-1} P(\lambda_{i+1}|\lambda_i), \tag{6.19}$$

where

$$\tilde{\Phi}_{A\lambda_1} = \Phi_{A\lambda_0} P(\lambda_1|\lambda_0). \tag{6.20}$$

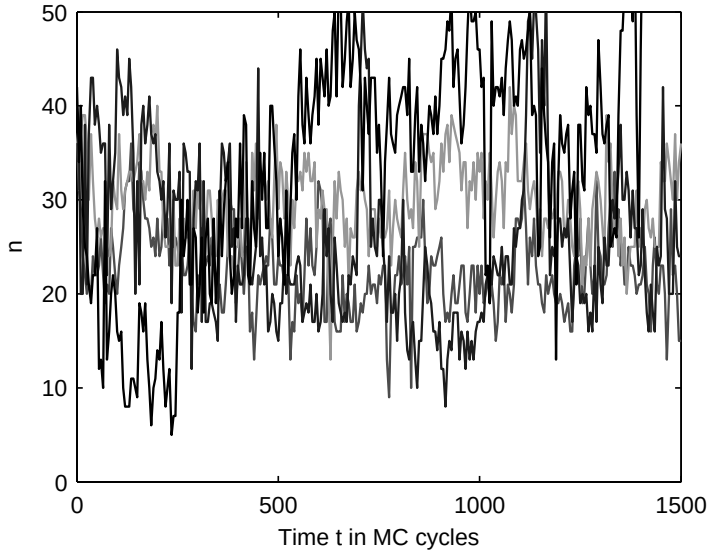

Figure 6.9: The cluster size as a function of time t in MC cycles for 4 random trajectories at pressure $\beta p\sigma^3 = 17$ starting with a cluster size of $n = 43$ using kinetic MC simulations with step size $\Delta_{\mathrm{KMC}} = 0.1\sigma$ and measuring the order parameter every $\Delta t_{\mathrm{ord}} = 5$ MC steps.

We note that if λ_1 is chosen such that it is a relatively rare event for trajectories starting in A to reach λ_1, then

$$\tilde{\Phi}_{A\lambda_1} \approx \frac{1}{\langle t_{A\lambda_1} \rangle V} \tag{6.21}$$

where $\langle t_{A\lambda_1} \rangle$ is the average time it takes a trajectory in A to reach λ_1. A sketch of this method is shown in Figure 6.10. The approximation made here, in contrast to normal FFS simulations, is that the time the system spends with an order parameter greater than λ_1 is negligible. Since even reaching this interface is a rare event, this approximation should have a minimal effect on the resulting rate. Additionally, in this way we are relatively free to place the first interface (λ_0) anywhere under λ_1.* We choose to use $\lambda_0 = 1$ to minimize the effect of fluctuations, as seen in Figure 6.9, on the probability to reach the following interface. Here we assume that any crystalline order in a system with an order parameter of 1 likely does not arise from fluctuation of a much larger cluster, but rather is very close to the fluid. Thus, it is expected to fully melt and not grow out to the next interface. In this manner we are able to start several parallel trajectories from the fluid in order to measure $\langle t_{A\lambda_1} \rangle$, stopping whenever the trajectory first hits interface λ_1.

In our implementation of FFS, we employ kinetic Monte Carlo (KMC) simulations at fixed pressure to follow the trajectories from the liquid to the solid. The KMC simulations are characterized by two parameters, the maximum step size (Δ_{KMC}) per attempt to move each particle, and the frequency with which the order parameter (reaction coordinate)

* While it does appear that Eq. 6.19 is completely independent of λ_0, this is not strictly correct as λ_0 creates the border for state A and state A is expected to be a metastable, equilibrated state. For the purposes of this chapter, the difference is insignificant as the average time for a nucleation event is much longer than the relaxation time for the fluid.

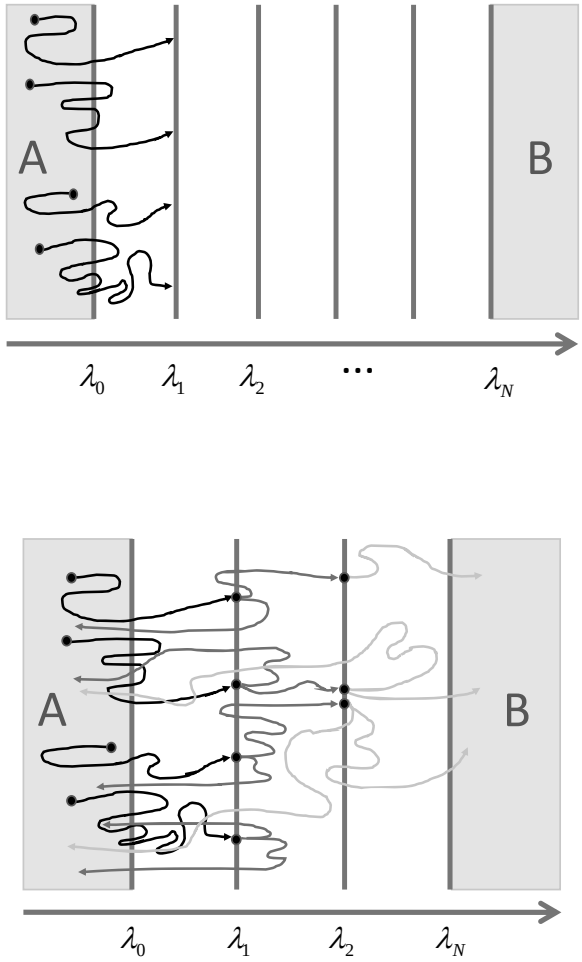

Figure 6.10: Top: In our implementation of FFS, instead of calculating the flux as shown in Figure 6.8, we start a number of simulations in the A region and use them to determine the average time to reach interface λ_1. Equation 6.21 is then used to determine the flux. Bottom: As sketch showing how $P(\lambda_N|\lambda_1)$ is calculated.

is measured Δt_{ord}. However, during an FFS simulation, it is expected that the order parameter is known at all times such that it is possible to identify exactly when and if a given simulation reaches an interface. Thus it is possible that Δt_{ord} introduces an additional error into our measurement of the rate.

To examine the effects of (i) the approximation associated with our method for calculating $\tilde{\Phi}_{A\lambda_1}$, (ii) the short-time fluctuations of the order parameter (which could be considered as an error in the measurement of the cluster size), and (iii) the frequency of measuring the order parameter, we examined the nucleation rate for a simple one-dimensional model system in the presence of such features. Details of these simulations are given in Chapter 7. However, we point out here that in this simple model system, we find that none of these features have a large effect on the rate. In fact, for most cases,

Δ_{KMC}	0.1	0.1	0.1	0.2	0.2	0.2
Δt_{ord}	2	2	2	2	2	2
$P(\lambda_2\|\lambda_1)$	0.112	0.103	0.139	0.101	0.105	0.132
$P(\lambda_3\|\lambda_2)$	0.096	0.117	0.090	0.104	0.093	0.112
$P(\lambda_4\|\lambda_3)$	0.128	0.117	0.074	0.116	0.111	0.161
$P(\lambda_5\|\lambda_4)$	0.180	0.159	0.082	0.156	0.115	0.241
$P(\lambda_6\|\lambda_5)$	0.167	0.154	0.149	0.225	0.148	0.256
$P(\lambda_7\|\lambda_6)$	0.071	0.074	0.060	0.128	0.093	0.118
$P(\lambda_8\|\lambda_7)$	0.104	0.078	0.051	0.109	0.091	0.109
$P(\lambda_9\|\lambda_8)$	0.100	0.100	0.105	0.083	0.075	0.089
$P(\lambda_9\|\lambda_1)$	$3 \cdot 10^{-8}$	$2 \cdot 10^{-8}$	$4 \cdot 10^{-9}$	$5 \cdot 10^{-8}$	$1 \cdot 10^{-8}$	$2 \cdot 10^{-7}$
Δ_{KMC}	0.2	0.2	0.2	0.2	0.2	0.2
Δt_{ord}	1	1	1	10	10	10
$P(\lambda_2\|\lambda_1)$	0.112	0.146	0.138	0.122	0.127	0.146
$P(\lambda_3\|\lambda_2)$	0.115	0.097	0.079	0.103	0.081	0.080
$P(\lambda_4\|\lambda_3)$	0.151	0.110	0.110	0.121	0.091	0.116
$P(\lambda_5\|\lambda_4)$	0.209	0.189	0.173	0.121	0.073	0.150
$P(\lambda_6\|\lambda_5)$	0.274	0.151	0.189	0.189	0.121	0.187
$P(\lambda_7\|\lambda_6)$	0.121	0.052	0.092	0.169	0.077	0.064
$P(\lambda_8\|\lambda_7)$	0.119	0.077	0.126	0.132	0.087	0.064
$P(\lambda_9\|\lambda_8)$	0.101	0.081	0.129	0.101	0.109	0.068
$P(\lambda_9\|\lambda_1)$	$2 \cdot 10^{-7}$	$1 \cdot 10^{-8}$	$6 \cdot 10^{-8}$	$8 \cdot 10^{-8}$	$6 \cdot 10^{-9}$	$1 \cdot 10^{-8}$

Table 6.5: Probabilities $P(\lambda_{i+1}|\lambda_i)$ for the first 8 interfaces at a pressure of $\beta p\sigma^3 = 15$ where the KMC simulations step size (Δ_{KMC}) and the number of MC steps between measuring the order parameter Δt_{ord} are varied. The following interfaces were used: $\lambda_2 = 20$, $\lambda_3 = 26$, $\lambda_4 = 32$, $\lambda_5 = 38$, $\lambda_6 = 44$, $\lambda_7 = 54$, $\lambda_8 = 65$, and $\lambda_9 = 78$. In all cases, 100 configurations were started in the fluid and reached the first interface, and at each interface, $C_i = 10$ copies of each successful configuration were used.

the difference is too small to see within our error bars.

6.6.2 Simulation details and results

All simulations were performed with 3000 particle in a cubic box with periodic boundary conditions. Initial configurations were produced using NPT MC simulations of a liquid phase with a packing fraction of $\eta \approx 0.4$ and then simulated at a reduced pressure of $\beta p\sigma^3 = 1000$. The simulations were stopped when the packing fraction associated with the pressure of interest was reached. In this way the system volume decreased rapidly to the target density. This initial configuration was then relaxed using an NPT simulation at the pressure of interest ($\beta p\sigma^3 = 15, 16, 17$). The relaxation consisted of at least 10,000 MC cycles, after which the simulation continued until a measurement of the order parameter found no crystalline particles in the system.

In order to determine the flux and the probabilities, 100 trajectories were started in the liquid and terminated when $n(\mathbf{r}^N) = \lambda_1$. These trajectories were produced using

$\beta p\sigma^3$	λ_1	$\tilde{\Phi}_{A\lambda_1}/6D_l$	$P(\lambda_B\|\lambda_1)$	$R/6D_l$
17	27	$2.66 \cdot 10^{-5}$	$7.6 \cdot 10^{-3}$	$2.0 \cdot 10^{-7}$
17	27	$2.68 \cdot 10^{-5}$	$1.4 \cdot 10^{-2}$	$3.7 \cdot 10^{-7}$
16	20	$8.57 \cdot 10^{-6}$	$3.1 \cdot 10^{-7}$	$2.6 \cdot 10^{-12}$
16	20	$8.57 \cdot 10^{-6}$	$2.1 \cdot 10^{-7}$	$1.8 \cdot 10^{-12}$
15	15	$8.72 \cdot 10^{-6}$	$1.9 \cdot 10^{-15}$	$1.6 \cdot 10^{-20}$

Table 6.6: Nucleation rates predicted using forward flux sampling in long-time diffusion coefficient units (D_l). The probabilities $P(\lambda_B|\lambda_1)$, number of steps between the order parameter measurements Δ_{ord}, and kinetic MC step size are as in Tables 6.7, 6.8, and 6.9. At each interface, C_i copies of each successful configuration were used.

		trial 1		trial 2	
i	λ_i	C_{i-1}	$P(\lambda_i\|\lambda_{i-1})$	C_{i-1}	$P(\lambda_i\|\lambda_{i-1})$
2	43	10	0.137	10	0.157
3	60	10	0.272	10	0.312
4	90	10	0.350	10	0.414
5	150	2	0.594	2	0.691
6	250	2	0.988	2	0.988

Table 6.7: Probabilities $P(\lambda_{i+1}|\lambda_i)$ for the interfaces used in calculating the nucleation rate for pressure $\beta p\sigma^3 = 17$ with step size $\Delta_{\text{KMC}} = 0.1\sigma$ and measuring the order parameter every $\Delta t_{\text{ord}} = 5$ MC cycles.

		trial 1		trial 2	
i	λ_i	C_{i-1}	$P(\lambda_i\|\lambda_{i-1})$	C_{i-1}	$P(\lambda_i\|\lambda_{i-1})$
2	28	10	0.105	10	0.110
3	38	10	0.075	10	0.077
4	50	10	0.070	10	0.089
5	70	10	0.114	10	0.089
6	90	10	0.095	10	0.101
7	110	10	0.339	10	0.278
8	250	10	0.152	10	0.112
9	350	1	1.000	1	1.000

Table 6.8: Same as Table 6.7 but for $\beta p\sigma^3 = 16$.

i	λ_i	C_{i-1}	$P(\lambda_i\|\lambda_{i-1})$
2	20	10	0.101
3	26	10	0.104
4	32	10	0.116
5	38	10	0.156
6	44	10	0.225
7	54	10	0.128
8	65	10	0.109
9	78	10	0.083
10	92	10	0.101
11	110	10	0.085
12	135	10	0.062
13	160	10	0.131
14	190	10	0.131
15	230	10	0.134
16	400	10	0.058

Table 6.9: Same as Table 6.7 but for $\beta p\sigma^3 = 15$ and with $\Delta t_{\rm ord} = 2$.

KMC simulations. The probability $P(\lambda_2|\lambda_1)$ was then found by making C_1 copies of the configurations that reached λ_1, and following these configurations until they either reached λ_2 or returned to the fluid. By taking different random number seeds, the various copies of the same configurations follow different trajectories. The fraction of successful trajectories corresponds to the required probability. The successful trajectories were then copied C_2 times to determine $P(\lambda_3|\lambda_2)$. The remaining $P(\lambda_{i+1}|\lambda_i)$'s are calculated similarly.

To study the effect of the two KMC parameters, namely $\Delta_{\rm KMC}$ and $\Delta t_{\rm ord}$, on the nucleation rates, we have examined the first 8 FFS windows for $\beta p\sigma^3 = 15$ for various values of the number of MC steps between the order parameter measurements $\Delta t_{\rm ord}$ and the maximum displacement $\Delta_{\rm KMC}$ for the KMC simulations. The results are shown in Table 6.5. As shown in this table we do not find a significant effect on the rate from either parameter. Thus for numerical efficiency, unless otherwise indicated, the rates in this section come from $\Delta t_{\rm ord} = 5$ MC cycles and $\Delta_{\rm KMC} = 0.2\sigma$.

For pressures $\beta p\sigma^3 = 16$ and 17 we have performed two separate FFS calculations to determine the nucleation rates, and for pressure $\beta p\sigma^3 = 15$ we have the result from a single FFS simulation. A summary of the results are given in Table 6.6. A complete summary of the results for $P(\lambda_{i+1}|\lambda_i)$ for each simulation is given in Tables 6.7, 6.8, and 6.9.

6.7 Summary and discussion

6.7.1 Nucleation rates

In this section we examine hard-sphere nucleation rates predicted using US simulations, MD simulations and FFS simulations together with the experimental results of Harland

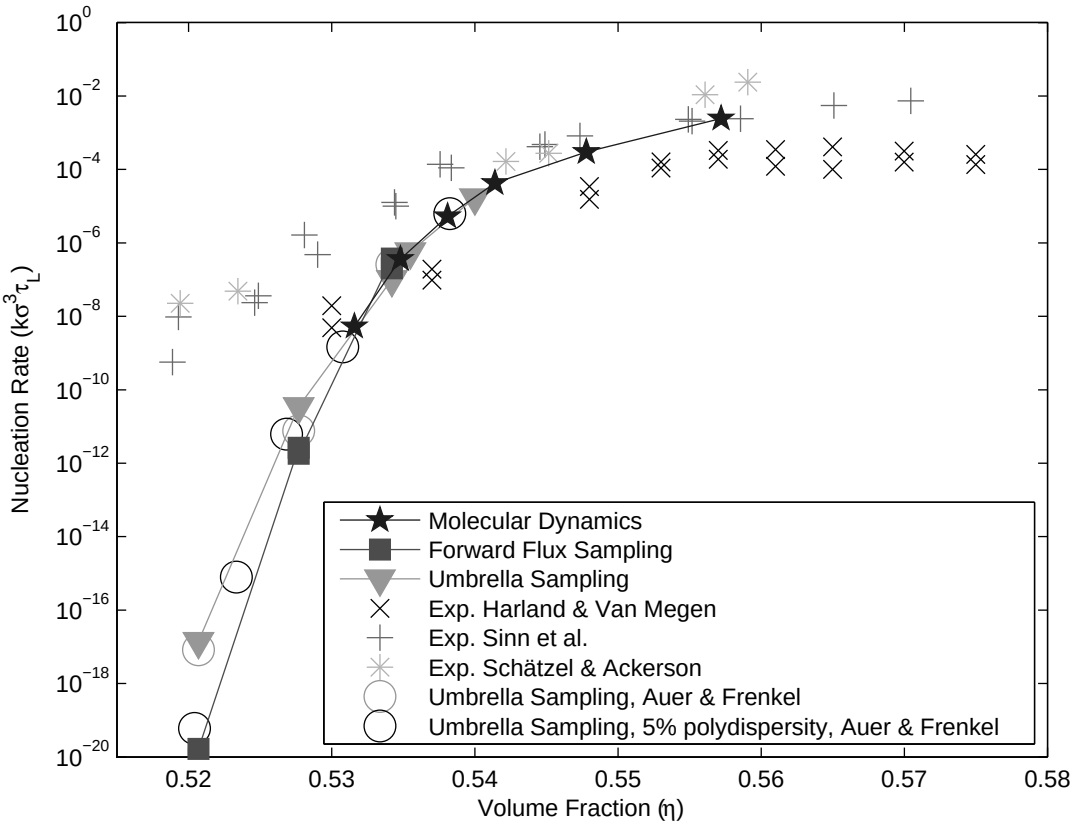

Figure 6.11: A comparison of the crystal nucleation rates of hard spheres as determined by the three methods described in this chapter FFS, US, and MD with the experimental results from Refs. [100–102] and previous theoretical results from Ref. [103]. Note that error bars have not been included in this plot. In general, the error bars of the simulated nucleation rates are largest for lower supersaturations (i.e. lower volume fractions), as the barrier height is higher. For the FFS and US simulations, the error for $\beta p\sigma^3 = 15$ ($\eta = 0.5214$) is between 2 and 3 orders of magnitude, and for $\beta p\sigma^3 = 17$ ($\eta = 0.5352$) is approximately one to two orders of magnitude. The MD results are quite accurate around $\beta p\sigma^3 = 17$, however the error bars are larger for the higher pressure MD results. Within these estimated error bars, the simulated nucleation rates are all in agreement, while the experimentally obtained rates show a markedly different behaviour, particularly for low supersaturations where the difference between the simulations and experiments can be as large as 12 orders of magnitude.

and Van Megen, [100] Sinn *et al.* [101] and Schätzel and Ackerson [102] and the US simulations of monodisperse and 5% polydisperse hard-spheres mixtures examined by Auer and Frenkel [103]. The experimental volume fractions have been scaled to yield the coexistence densities of monodisperse hard spheres [110]. Similarly, we have scaled the polydisperse results of Auer and Frenkel with the coexistence densities determined in Ref. [129]. Inspired by the recent work of Pusey *et al.* [110], we plot the nucleation rates in units of the long-time diffusion coefficient. In experiments with colloidal particles, the influence of the solvent on the dynamics cannot be ignored. Specifically, the system slows down due to hydrodynamic interactions when the density is increased. However, by

presenting the nucleation rates in terms of the long-time diffusion coefficient, we expect our simulated nucleation rates from the hard sphere model without an explicit solvent to be in agreement with the experimental rates with a solvent. The time in experiments is typically measured in units of D_0, the free diffusion at low density. We convert the short-time diffusion coefficient D_0 to long-time diffusion coefficient D_l using

$$\frac{D_l(\eta)}{D_0} = \left(1 - \frac{\eta}{0.58}\right)^{\delta}. \tag{6.22}$$

Harland and Van Megen [100] claim that $\delta = 2.6$ gives a good fit to their system and Sinn *et al.* [101] use $\delta = 2.58$. Since the system Schätzel and Ackerson [102] examine is very similar to the other two, we use $\delta = 2.6$ to convert their nucleation rates to long-time units. We note that both $\delta = 2.58$ and $\delta = 2.6$ give very similar results. The results for both the theoretical and experimental rates in long time units are shown in Figure 6.11. Note that for clarity reasons the error bars have not been included in this plot. In general, the error bars of the simulated nucleation rates are largest for lower supersaturations (i.e. lower volume fractions), as the barrier height is higher. For the FFS and US simulations, the error for $\beta p\sigma^3 = 15$ ($\eta = 0.5214$) is between 2 and 3 orders of magnitude, and for $\beta p\sigma^3 = 17$ ($\eta = 0.5352$) is approximately one to two orders of magnitude. The MD results are quite accurate around $\beta p\sigma^3 = 17$, however the error bars are larger for the higher pressure MD results.

In Ref. [110], Pusey *et al.* showed that the nucleation rates for various polydispersities (0 to 6%) of hard-sphere mixtures collapsed onto the same curve when the rates were plotted in units of the long-time diffusion coefficient. We find similar results here. Both the monodisperse and polydisperse US results of Auer and Frenkel [103], in addition to our own US predictions of the nucleation rate, agree well within the expected measurement error. Additionally, we find that the simulation results of the US, FFS, and MD all agree. Whereas the simulation results agree well with the experimental results for the nucleation rate at high supersaturation there is still a significant difference at low supersaturations. Unfortunately, the origin of this discrepancy remains unsolved.

However, on the experimental side, the nucleation rates of Harland and Van Megen [100] are approximately one to two orders of magnitude below the experiments of Sinn *et al.* [101] and Schätzel and Ackerson [102]. This is unexpected due to the similarity between the experimental systems. The main difference between these experiments is the polydispersity of the particle mixtures: 5% in the case of Harland and Van Megen [100], 2.5% in the case of Sinn *et al.* [101], and $< 5\%$ for Schätzel and Ackerson [102]. However, as demonstrated by Pusey *et al.* [110], and now also in Figure 6.11, the nucleation rate when measured in long-time diffusion coefficient units should not be effected by the polydispersity. Thus, this seems unlikely as an explanation.

6.7.2 Nuclei

To examine whether the structure and shape of the critical clusters from US simulations depended on the precise threshold values used for the crystalline order parameters, we compared and analysed the critical clusters obtained when three different crystalline order parameters were used to bias the US simulations, namely, $\xi_c = 5, 7$ and 9. Subsequently we

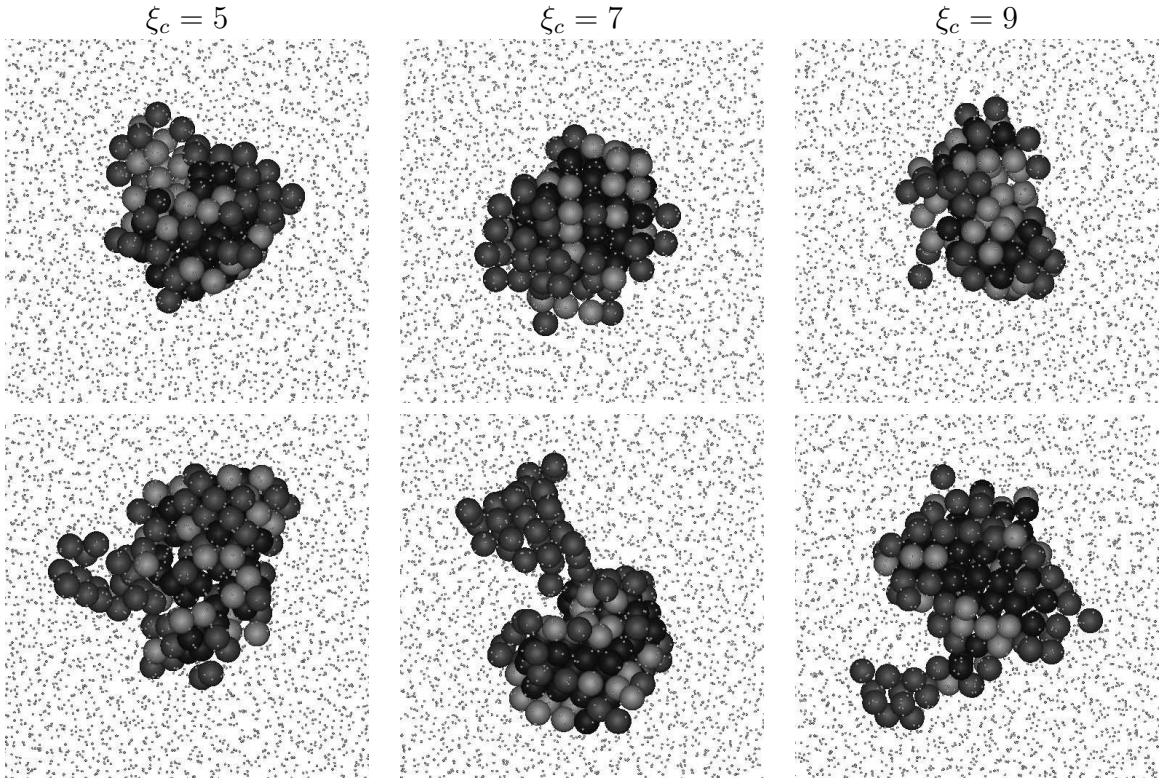

Figure 6.12: Colour version on page 128. Two typical snapshots (top and bottom) of the critical nuclei as obtained with US at a volume fraction $\eta = 0.5355$ using different values of the critical number of crystalline bonds $\xi_c = 5$ (left), 7 (middle) and 9 (right) in the biasing potential. The clusters are analyzed with three different crystalline order parameters. The blue particles are found by all three cluster criteria, the green particles have $\xi = 7$ or 8 crystalline bonds and the red particles have only $\xi = 5$ or 6 crystalline bonds.

analyzed these critical clusters using the three different order parameters. In Figure 6.12, two typical critical clusters from different biasing order parameters are shown on the top and bottom rows. The nucleus of the cluster, shown in blue, was identified by all three cluster criteria ($\xi_c = 5, 7$ and 9). The main difference between the criteria is the location of the fluid-solid interface as shown by the green and red particles. The strictest order parameter finds only the more ordered center whereas the loosest version detects the more disordered particles at the interface as well. In Figure 6.13 we show some of the nuclei obtained from MD simulations. These snapshots were taken just before the nuclei grew out so they are not necessarily precisely at the top of the nucleation barrier. They appear very similar in roughness and aspect ratio to those obtained from US simulations. We note here that this is not meant to be a thorough study of the critical clusters, but rather just a rough comparison to demonstrate that to a first approximation the clusters formed by the three simulation techniques are the same. A more thorough examination of the structure of the nuclei for high supersaturations can be found in Ref. [130].

To further examine whether the choice of method influenced the resulting clusters, particularly the presence of the biasing potential in the US simulations and the choice of reaction coordinate and interfaces in FFS, we calculated the radius of gyration tensor

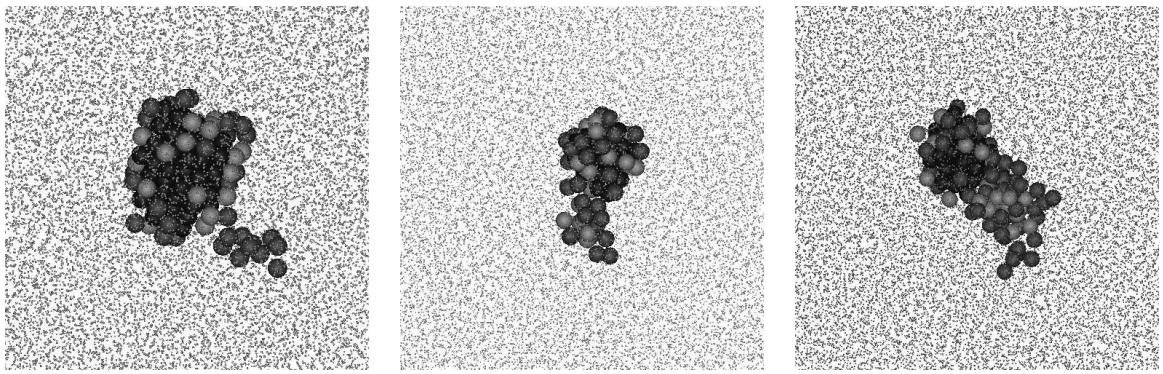

Figure 6.13: Colour version on page 128. Snapshots of spontaneously formed nuclei during an MD simulation at a volume fraction of $\eta = 0.537$. The snapshots were taken just before the nuclei grew. The colour coding of the particles is the same as in Figure 6.12.

for each of the methods for pressure $\beta p\sigma^3 = 17$ as a function of cluster size (see Figure 6.14). There is no indication that the clusters in any of the simulation methods differed substantially.

Additionally, we examined whether the simulation technique influenced the type of pre-critical nuclei that formed in the simulations, i.e. face-centered-cubic (FCC), and hexagonal-close-packed (HCP). To do this we used the order parameter introduced by Ref. [131] which allows us to identify each particle in the cluster as either FCC-like or HCP-like. The results for a wide range in nucleus size is shown in Figure 6.15. We find complete agreement between the three simulation techniques. Specifically, in all cases we find that the nucleus is composed of approximately 80% FCC-like particles. This was unexpected as the free-energy difference between the bulk FCC and HCP phases is about $0.001 k_B T$ per particle at melting [53] and hence random-hexagonal-close-packing order in the nuclei would be expected [132]. Note that using our order parameter this would appear as an approximately 50% occurrence of FCC- and HCP-like particles in the nucleus. We speculate that this predominance of FCC-like particles in the nuclei arises from surface effects.

6.8 Conclusions

In this chapter we have examined in detail three independent simulation techniques for studying nucleation processes and predicting nucleation rates, namely forward flux sampling, umbrella sampling and molecular dynamics. We have shown that the three simulation techniques are completely consistent in their prediction of the nucleation rates for hard spheres over the large range of volume fractions studied, despite the fact that they treat the dynamics differently. Additionally, in agreement with the recent work of Pusey *et al.* [110], we find that by measuring the nucleation rates in terms of the long-time diffusion constant and scaling to the coexistence density of monodisperse hard spheres, the 5% polydisperse results of Auer and Frenkel [103] also agree. On examining the critical clusters, we also do not find a difference in the nuclei formed using the three simulation techniques. Hence we conclude that the original prediction of Auer and Frenkel [103] for

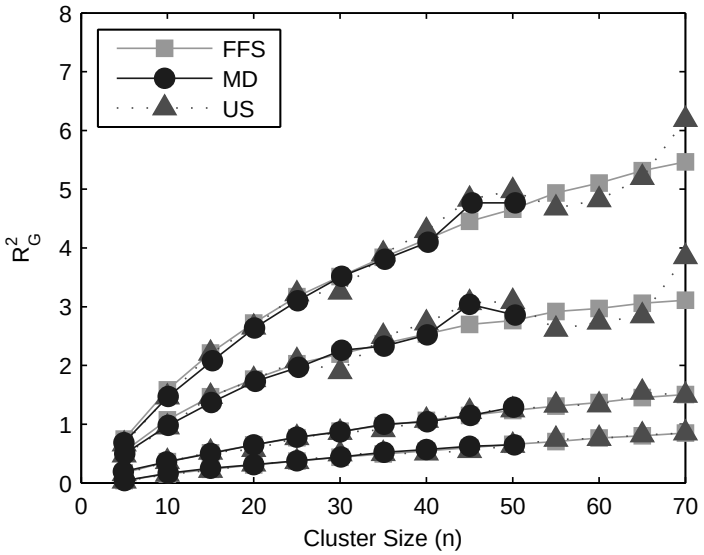

Figure 6.14: A comparison of the three components of the radius of gyration tensor as a function of cluster size n, as well as the sum of the three components, for clusters produced using FFS, MD, and US simulations.

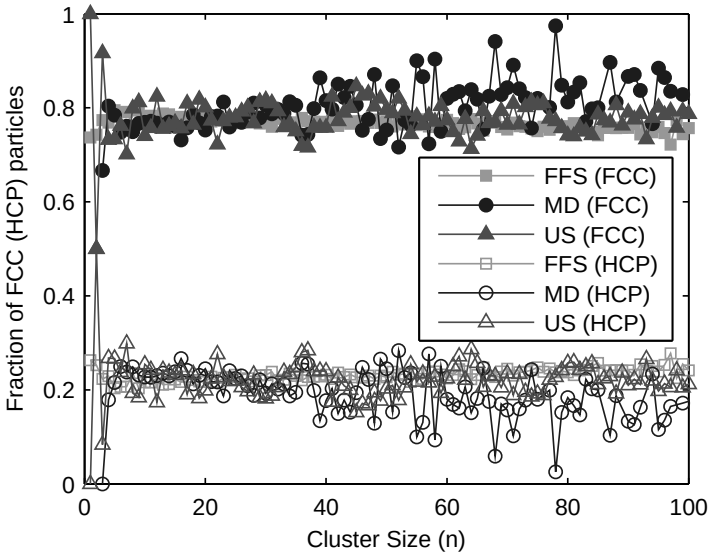

Figure 6.15: Fraction of particles identified as either FCC or HCP respectively in the clusters produced via molecular dynamics (MD), forward flux sampling (FFS), and umbrella sampling (US) simulations as a function of cluster size n. All three methods agree and find the pre-critial clusters prodominately FCC.

the nucleation rates in hard sphere systems was indeed robust.

We have also compared our nucleation rates with previous experimental data, specifically, the nucleation rates predicted by Harland and Van Megen [100], Sinn *et al.* [101] and Schätzel and Ackerson [102]. As was found first by Auer and Frenkel [103], while the simulation results agree well with the experimental results for high supersaturations, there is a significant difference between the simulations and experiments for smaller volume fractions. The agreement between the three theoretical methods examined in this chapter, namely molecular dynamics, umbrella sampling, and forward flux sampling, seems to indicate that either there is a fundamental difference between the simulations and theory which we are not taking into account, such as some form of collective hydrodynamics which are included in the experiments but not considered in the theory or some difficulty in interpreting the experimental data. In either case, the origin of the huge discrepancy in the theoretical and experimental nucleation rates remains a mystery.

6.9 Acknowledgements

I would like to thank Ran Ni and Michiel Hermes for their calculation of the nucleation rates from umbrella sampling and Michiel Hermes for his molecular dynamics rate calculations. Additionally, I like to thank Frank Smallenburg, Matthieu Marechal, Eduardo Sanz and Chantal Valeriani for many useful discussions.

7

Forward flux sampling in the presence of measurement error

In this chapter we apply a one dimensional toy model to examine in detail forward flux sampling as it applies to colloidal nucleation. In Chapter 6 we applied forward flux sampling to one of the simplest colloidal model systems, namely hard-sphere nucleation. We found that in order to apply forward flux sampling to such a colloidal system some small changes to the algorithm were necessary. Additionally, we claimed in Chapter 6 that forward flux sampling was not strongly sensitive to i) how frequently we measured the order parameter and ii) measurement errors in the order parameter. In this chapter we examine these points in more detail.

7.1 Introduction

The term "rare event" typically refers to fluctuation-driven events which occur infrequently. They occur in a wide variety of systems including, e.g., nucleation (such as the hard-sphere crystal nucleation studied in Chapter 6), protein folding, and activated chemical reactions. However, while rare events are often associated with important physical processes, their infrequency leads to extreme difficulty when trying to examine such events using computer simulations. More specifically, brute force simulation techniques such as molecular dynamics and Brownian dynamics are often rendered useless as the rare event time scales exceed reasonable simulation times.

To address this problem, a number of theoretical and simulation techniques have been introduced. In particular, umbrella sampling, "Bennett-Chandler" theory, transition path sampling, transition interface sampling (TIS), milestoning, and forward flux sampling (FFS). The majority of these techniques are based on (quasi-) equilibrium simulations, i.e. they can be applied to systems whose dynamics obey detailed balance. The one notable exception to this rule is forward flux sampling which was developed for the purpose of examining nonequilibrium systems.

As described in Chapter 6, in FFS the transition rate between states A and B is given by

$$k = \Phi_{A0} P\left(\lambda_B | \lambda_0\right) \tag{7.1}$$

where Φ_{A0} is the effective flux of trajectories leaving state A through interface λ_0 and $P\left(\lambda_B|\lambda_0\right)$ is the probability that a trajectory which leaves state A (by crossing λ_0) arrives in state B before returning to A. We should point out here that FFS is not the only rare event technique to make use of Eq. 7.1 to calculate the nucleation rate, TIS does as well. In a typical FFS simulation (or TIS simulation), the flux is determined by running a simulation (i.e. BD, MD, or kinetic Monte Carlo (KMC)) for a time T. The number of times (N) the simulated trajectory crosses the A state boundary, ie. λ_0, is measured. The flux is then given by

$$\Phi_{A0} = \frac{N}{T}. \tag{7.2}$$

A cartoon of this is shown in Figure 6.7. In forward flux sampling, the probability $P\left(\lambda_B|\lambda_0\right)$ is re-written as

$$P\left(\lambda_B|\lambda_0\right) = \prod_{i=0}^{n-1} P\left(\lambda_{i+1}|\lambda_i\right) \tag{7.3}$$

where λ_i are a set of interfaces subdividing the transition path from state A to B. A cartoon of this is depicted in Figure 6.8.

One of the fundamental assumptions of this technique is that the value of the order parameter is known at all times, and that it is exact. However, for the hard-sphere system examined in Chapter 6, this was not possible due to the computational time required for measuring the order parameter. In particular, in applying the FFS technique to hard spheres in Chapter 6, we noted two separate sources of error: i) error associated with our inability to know the value of the reaction coordinate at all times, and ii) an error in measuring the number of particles in a cluster for a given configuration. To deal with this problem we introduced a slightly different implementation of FFS in Chapter 6. In

Δt_{ord}	1	2	5	10	50
	$1.272 \cdot 10^{-12}$	$1.059 \cdot 10^{-12}$	$1.807 \cdot 10^{-12}$	$1.545 \cdot 10^{-12}$	$1.384 \cdot 10^{-12}$
	$1.378 \cdot 10^{-12}$	$1.722 \cdot 10^{-12}$	$1.331 \cdot 10^{-12}$	$1.446 \cdot 10^{-12}$	$1.067 \cdot 10^{-12}$
	$1.236 \cdot 10^{-12}$	$1.292 \cdot 10^{-12}$	$1.485 \cdot 10^{-12}$	$1.148 \cdot 10^{-12}$	$1.613 \cdot 10^{-12}$
	$1.694 \cdot 10^{-12}$	$1.642 \cdot 10^{-12}$	$1.948 \cdot 10^{-12}$	$1.438 \cdot 10^{-12}$	$1.755 \cdot 10^{-12}$
	$1.266 \cdot 10^{-12}$	$1.234 \cdot 10^{-12}$	$1.569 \cdot 10^{-12}$	$1.606 \cdot 10^{-12}$	$1.291 \cdot 10^{-12}$
	$1.692 \cdot 10^{-12}$	$1.353 \cdot 10^{-12}$	$1.624 \cdot 10^{-12}$	$1.624 \cdot 10^{-12}$	$1.401 \cdot 10^{-12}$
	$1.465 \cdot 10^{-12}$	$1.179 \cdot 10^{-12}$	$1.693 \cdot 10^{-12}$	$1.019 \cdot 10^{-12}$	$1.340 \cdot 10^{-12}$
	$1.681 \cdot 10^{-12}$	$1.586 \cdot 10^{-12}$	$1.190 \cdot 10^{-12}$	$1.623 \cdot 10^{-12}$	$1.058 \cdot 10^{-12}$
	$1.460 \cdot 10^{-12}$	$1.702 \cdot 10^{-12}$	$1.319 \cdot 10^{-12}$	$1.385 \cdot 10^{-12}$	$2.373 \cdot 10^{-12}$
	$1.746 \cdot 10^{-12}$	$1.915 \cdot 10^{-12}$	$1.564 \cdot 10^{-12}$	$1.238 \cdot 10^{-12}$	$1.269 \cdot 10^{-12}$
Avg. Rate	$1.5 \cdot 10^{-12}$	$1.5 \cdot 10^{-12}$	$1.6 \cdot 10^{-12}$	$1.4 \cdot 10^{-12}$	$1.5 \cdot 10^{-12}$
Std. Error	$6.0 \cdot 10^{-14}$	$8.4 \cdot 10^{-14}$	$7.0 \cdot 10^{-14}$	$6.3 \cdot 10^{-14}$	$1.2 \cdot 10^{-13}$

Table 7.1: Nucleation rates for the one-dimensional potential given by Eq. 7.4 and shown in Fig. 7.1 for Δt_{ord} as indicated. For each Δt_{ord} , we performed 10 independent FFS simulations. The average rate and associated standard deviation are also as indicated. In all cases, 100 configurations were started in the fluid, and at each interface $C_i = 10$ copies of the successful configurations were used to calculate the proceeding probabilities. The interfaces were placed at $\lambda_0 = 0$, $\lambda_1 = 1.5$, $\lambda_2 = 1.7$, $\lambda_3 = 1.9$, $\lambda_4 = 2.2$, $\lambda_5 = 2.6$, $\lambda_6 = 3.3$, and $\lambda_7 = 4.0$.

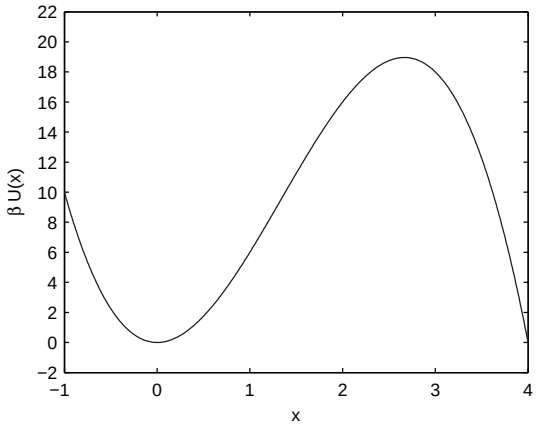

Figure 7.1: Toy model potential used to study forward flux sampling in the presence of various types of measurement error.

this chapter, we use this new implementation to examine the two types of measurement error listed above.

7.2 Model

A simple analogue for the crystal nucleation in hard spheres consists of a random walk over the Gibbs free-energy barrier. Hence, to examine in more detail FFS as applied to crystal nucleation, we study the transition rate for a single Brownian particle to surmount

σ_{Gauss}	0.02	0.04	0.06	0.08	0.1
	$1.862 \cdot 10^{-12}$	$1.728 \cdot 10^{-12}$	$1.263 \cdot 10^{-12}$	$1.063 \cdot 10^{-12}$	$1.916 \cdot 10^{-12}$
	$1.763 \cdot 10^{-12}$	$1.609 \cdot 10^{-12}$	$1.640 \cdot 10^{-12}$	$1.566 \cdot 10^{-12}$	$1.879 \cdot 10^{-12}$
	$9.980 \cdot 10^{-13}$	$1.630 \cdot 10^{-12}$	$1.580 \cdot 10^{-12}$	$1.694 \cdot 10^{-12}$	$1.494 \cdot 10^{-12}$
	$1.374 \cdot 10^{-12}$	$1.226 \cdot 10^{-12}$	$1.830 \cdot 10^{-12}$	$1.773 \cdot 10^{-12}$	$1.114 \cdot 10^{-12}$
	$1.692 \cdot 10^{-12}$	$1.805 \cdot 10^{-12}$	$1.619 \cdot 10^{-12}$	$1.894 \cdot 10^{-12}$	$1.040 \cdot 10^{-12}$
	$1.184 \cdot 10^{-12}$	$1.334 \cdot 10^{-12}$	$1.328 \cdot 10^{-12}$	$1.404 \cdot 10^{-12}$	$7.073 \cdot 10^{-13}$
	$1.529 \cdot 10^{-12}$	$8.686 \cdot 10^{-13}$	$1.313 \cdot 10^{-12}$	$2.711 \cdot 10^{-12}$	$2.471 \cdot 10^{-12}$
	$1.892 \cdot 10^{-12}$	$1.433 \cdot 10^{-12}$	$1.320 \cdot 10^{-12}$	$1.379 \cdot 10^{-12}$	$1.629 \cdot 10^{-12}$
	$1.314 \cdot 10^{-12}$	$1.228 \cdot 10^{-12}$	$1.046 \cdot 10^{-12}$	$1.719 \cdot 10^{-12}$	$1.376 \cdot 10^{-12}$
	$1.665 \cdot 10^{-12}$	$1.124 \cdot 10^{-12}$	$1.257 \cdot 10^{-12}$	$1.963 \cdot 10^{-12}$	$1.898 \cdot 10^{-12}$
Avg. Rate	$1.5 \cdot 10^{-12}$	$1.4 \cdot 10^{-12}$	$1.4 \cdot 10^{-12}$	$1.7 \cdot 10^{-12}$	$1.6 \cdot 10^{-12}$
Std. Error	$9.5 \cdot 10^{-14}$	$9.4 \cdot 10^{-14}$	$7.5 \cdot 10^{-14}$	$1.4 \cdot 10^{-13}$	$1.6 \cdot 10^{-13}$

Table 7.2: Nucleation rates for the one-dimensional potential given by Eq. 7.4 and shown in Fig. 7.1 where the order parameter is given by Eq. 7.6 and σ_{Gauss} is as indicated. For each σ_{Gauss}, we performed 10 independent FFS simulations. The average rate and associated standard deviation is also as indicated. In all cases, 100 configurations were started in the fluid, and at each interface $C_i = 10$ copies of the successful configurations were used to calculate the proceeding probabilities. The interfaces were placed at $\lambda_0 = 0$, $\lambda_1 = 1.5$, $\lambda_2 = 1.7$, $\lambda_3 = 1.9$, $\lambda_4 = 2.2$, $\lambda_5 = 2.6$, $\lambda_6 = 3.3$, and $\lambda_7 = 4.0$.

a one dimensional potential energy barrier given by

$$\beta U(x) = 8x^2 - 2x^3. \tag{7.4}$$

A plot of the barrier is shown in Fig. 7.1. For this potential, we consider the 'liquid' state to be near $x = 0$ and the 'solid' phase to be near $x = 4$.

7.3 Exact nucleation rate

We determine the 'exact' nucleation rate using spontaneous simulations. To do this we perform a random walk starting at $x = 0$ and determine the time it takes the random walk to surmount the barrier. The rate is then given by

$$R = 1/\langle t \rangle . \tag{7.5}$$

Performing 40 such random walks we find the nucleation rate to be $1.3 \cdot 10^{-12}$. In all the calculations in this section, we set the maximum step size equal to $\Delta = 0.025$.

7.4 Forward flux sampling

In this section we explore the effect on the nucleation rate of not knowing the value of the order parameter at all times. For this purpose we have performed FFS simulations when the order parameter was measured every $\Delta t_{\text{ord}} = 1, 2, 5, 10$ and 50 steps. The results are

shown in Table 7.1. The average nucleation rates predicted for all values of Δt_{ord} clearly are the same within error. Similarly, the standard errors associated with $\Delta t_{\text{ord}} = 1, 2, 5, 10$ are approximately the same, and the standard error for $\Delta t_{\text{ord}} = 50$ is only marginally larger. Hence we conclude that the frequency of measuring the order parameter does not significantly affect the predicted nucleation rate. Additionally, these nucleation rates agree with the nucleation rate obtained from the exact simulations indicating that applying FFS as outlined in Section 6.6 predicts the correct nucleation rates.

Finally, we examine the effect that measurement error in the cluster size has on the nucleation rate. For this purpose, we apply a noise term to our order parameter such that

$$x_m = x_{\text{true}} + \delta, \tag{7.6}$$

where x_m is the value of the order parameter used in the FFS simulation, x_{true} is the true value of the order parameter, and δ is taken from a Gaussian distribution with a mean of 0 and a standard deviation σ_{Gauss}. In Table 7.2 we demonstrate the effect on the predicted nucleation rate for various choices of σ_{Gauss}. The resulting nucleation rates are in good agreement with the spontaneous results. For larger σ_{Gauss}, eg. $\sigma_{\text{Gauss}} = 0.08$ and 0.1, the standard error in the results is slightly larger, however, the predicted nucleation rates are still correct.

7.5 Conclusion

In summary, we have examined the effect of measurement error in the order parameter and the measurement frequency Δt_{ord} of the order parameter. We do not find a significant effect on the predicted nucleation rates. Thus we conclude that FFS should be robust to the types of error we are introducing when we apply the technique to hard spheres.

7.6 Acknowledgements

I would like to thank Frank Smallenburg for many useful discussions.

8

Crystal nucleation of the WCA model with $\beta\epsilon = 40$

In this chapter we examine the equilibrium phase behaviour and nucleation of the Weeks-Chandler-Andersen (WCA) potential with $\beta\epsilon = 40$. Using Monte Carlo simulations in combination with common tangent constructions, we determine the melting and freezing number densities. Additionally, we use computer simulations to examine the crystal nucleation. We use Brownian dynamics, forward flux sampling, and a Bennett-Chandler type theory where the nucleation barrier is determined using umbrella sampling simulations to predict the nucleation rates for a variety of supersaturations. We compare our results to a previous simulation study of this model by Kawasaki and Tanaka [T. Kawasaki and H. Tanaka, PNAS **107** 14036 (2010)] and to hard-sphere nucleation rates predicted in simulations and those found with light scattering experiments. After mapping to the freezing number density of hard spheres, we find that our predicted nucleation rates are in good agreement with those predicted for the hard-sphere model, but disagree strongly at low supersaturation to those found experimentally for hard spheres. Strangely, our results also disagree with the nucleation rates predicted by Kawasaki and Tanaka [T. Kawasaki and H. Tanaka, PNAS **107** 14036 (2010)] using Brownian dynamics simulations.

8.1 Introduction

Colloidal solutions consist of small particles, which can be in a gas, liquid or solid phase, suspended in another medium. Colloidal systems are typically characterized by the dynamics of these suspended particles, i.e., colloidal particles exhibit Brownian motion. As a result, Brownian dynamics simulations (BD) are the natural choice to use when examining dynamical properties of colloidal systems, such as crystal nucleation. Brownian dynamics are based on a simplified version of Langevin dynamics and correspond to the "overdamped" limit. Specifically, in BD we assume that the particles' inertia is completely damped out by frictional forces. As a result, the motion of the particles is completely determined by the instantaneous forces acting on the colloid plus a stochastic, diffusive displacement. However, unlike molecular dynamics simulations (MD) where an event driven formalism exists which allows one to apply MD to systems with hard-core interactions (see Chapter 6), no such formalism exists to apply BD to hard particles. Hence, when Brownian dynamics are applied to hard-core interactions, the hard core is typically approximated.

A number of different approximations have been applied to mimic the hard-core interaction [112, 133]. In general they consist simply of a very short range, strongly repulsive interaction. One such approximation is the Weeks-Chandler-Andersen (WCA) potential. The WCA potential [134] is given by

$$\beta V_{\mathrm{WCA}}(r) = \begin{cases} 4\beta\epsilon\left(\left(\frac{\sigma}{r}\right)^{12} - \left(\frac{\sigma}{r}\right)^{6} + 0.25\right) & r \leq 2^{1/6} \\ 0 & r > 2^{1/6} \end{cases} \tag{8.1}$$

where σ is a length scale and ϵ is the energy scale. Note that the WCA potential is simply the Lennard-Jones potential where the cutoff is chosen such that only the repulsive part remains and the potential is shifted upwards so that the minimum occurs at zero. A plot of this potential is shown in Figure 8.1.

In a recent set of articles [113, 133, 135], Tanaka and others have approximated the hard-sphere potential by a WCA potential where they set $\beta\epsilon = 40$. They applied this approximation to determine, via brute force Brownian dynamics simulations, the nucleation rates in hard spheres. However, as we will show in section 8.4, the results they find are markedly different from those we found in Chapter 6. In this chapter we examine in detail the phase behaviour and crystal nucleation of the WCA model with $\beta\epsilon = 40$ and compare our results to those of Kawasaki and Tanaka.

This chapter is organized as follows: in section 8.2 we calculate the phase diagram for this model, in section 8.3 we describe the nucleation rates, in section 8.4 we compare our results to those of Kawasaki and Tanaka [113] and the hard-sphere nucleation rates presented in Chapter 6 and discuss the role of softness in the crystal nucleation rates, and our conclusions are found in section 8.5.

8.2 Phase diagram

The phase diagram for the WCA potential with $\beta\epsilon = 40$ has been examined previously [113, 136]. Kawasaki and Tanaka [113] find the freezing number density to be $\sigma^3\rho_F^{K_{\min}} =$

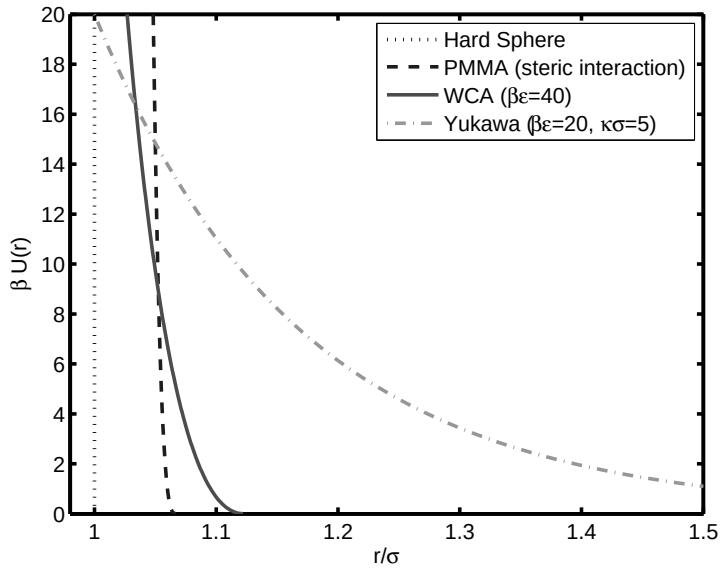

Figure 8.1: An overview of four pair potentials $\beta U(r)$ as a function of the center-to-center distance r including a hard-sphere potential with a diameter σ, an approximation for the interaction between two PMMA coated particles with radius $R/\sigma = 0.5$, mean distance between attachment points of the ligand chains $s/\sigma = 0.00498$, capping layer extension $L/\sigma = 0.0336$ and $\alpha = 0.025$, the WCA potential given in Eq. 8.1 with $\beta\epsilon = 40$ and a hard-core Yukawa potential with the prefactor $\beta\epsilon = 20$ and screening length $\kappa\sigma = 5$.

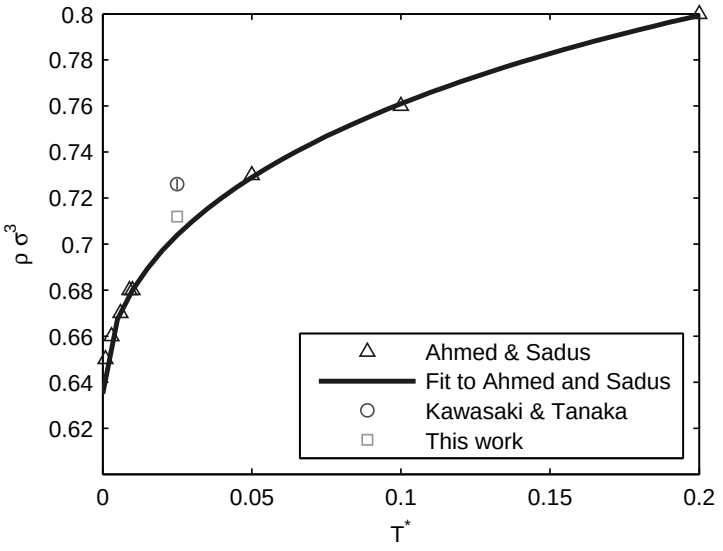

Figure 8.2: The *triangles* correspond to the freezing number density (ρ_F^A) from Ahmed and Sadus [136] as a function of T^* where $T^* = k_BT/\epsilon$. The fit corresponds to $\rho_F = 0.635 + 0.473(T^*)^{1/2} - 0.236T^*$. The *square* corresponds to the freezing number density (ρ_F^*) determined using full free energy calculations described in this chapter. The *circle* corresponds to the freezing number density range determined by Kawasaki and Tanaka [113].

0.726 ± 0.002. Additionally, the phase behaviour of the WCA potential was examined by Ahmed and Sadus [136] for a range of $T^* = 1/\beta\epsilon$. Their results are plotted in Figure 8.2. We find that their results for the freezing number density ρ_F as a function of $\beta\epsilon$ fits well to $\rho_F\sigma^3 = 0.635 + 0.473(T^*)^{1/2} - 0.236T^*$. From this fit we approximate a freezing number density of $\rho_F^A\sigma^3 = 0.704$. Hence, the two values found in literature for the WCA potential with $\beta\epsilon = 40$ differ by $\Delta\rho\sigma^3 = 0.022$.

A difference of $\Delta\rho\sigma^3 = 0.02$ can be significant in terms of nucleation rates, thus we have re-calculated the phase diagram. To calculate the coexistence densities for the WCA potential, we used full free-energy calculations in combination with common tangent constructions. For the crystal phase, the excess free energy F_{ex}, was calculated using Einstein integration [20, 21, 61] at a density of $\rho\sigma^3 = 0.8$ for systems of $N = 500, 864, 1372$ and 2048 particles. Note that the excess free energy is defined by $F_{ex} = F_{tot} - F_{id}$ where F_{tot} is the total free energy and F_{id} is the ideal gas free energy. Following Ref. [61], we plotted $\beta F_{ex}/N + \log N/N$ as a function of $1/N$ and extrapolated to an infinite system yielding a free energy of $\beta F_{tot}/N = 4.8975$. The free energy at other densities was determined using thermodynamic integration over the equation of state [20]. The equation of state was determined with a system containing $N = 4000$ particles. Note that no significant difference was found in the coexistence densities for equations of state determined using $N = 1372$ and $N = 4000$. To test our Einstein integration and integration over the equation of state, we determined the free energy at $\rho\sigma^3 = 0.9$ for $N = 1372$ and integrated over the equation of state calculated for $N = 1372$. The free energies agreed within 0.00046 k_BT per particle. The fluid chemical potential was determined using the Widom insertion technique [20] at $\rho\sigma^3 = 0.4$ with $N = 4000$ and was found to be $\beta\mu = 3.3173$; for $N = 1372$ we find $\beta\mu = 3.3194$. Again integration over the equation of state was used to determine the free energy as a function of density. To test the Widom insertion calculations, and our integration over the equation of state, we also calculated the chemical potential at $\rho\sigma^3 = 0.3$ for $N = 1372$. The difference in the free energy at $\rho = 0.3$ associated with the Widom insertions and integration over the equation of state results in a free energy difference of 0.00075 k_BT per particle, and hence we concluded that the Widom insertions and integration over the equation of state were correct. Using these free energies and common tangent constructions we find freezing and melting coexistence densities $\rho_F^*\sigma^3 = 0.712$ and $\rho_M^*\sigma^3 = 0.784$ respectively. All theoretically predicted freezing number densities ρ_F are plotted Figure 8.2.

8.3 Nucleation rates

In this section we apply Brownian dynamics, umbrella sampling and forward flux sampling to study the crystal nucleation of the WCA model. The methods for predicting nucleation rates have been discussed in detail in Chapter 6, and thus in this chapter we will only focus on the results. In all of these methods an order parameter is required to identify crystalline particles and to determine which cluster they belong to. The order parameter we use here is the same as that described in Chapter 6. We note that this order parameter depends on four parameters, namely the nearest neighbour cutoff defined as r_c, the dot-product cutoff defined as d_c,the minimum number of solid-like neighbours required for a

ρ	M	$t\sigma^2/6D_0$	$k\sigma^5/D_0$
0.79228	5	82.8	$1.4 \cdot 10^{-5}$
0.78507	5	954	$1.2 \cdot 10^{-6}$
0.78153	9	1560	$7.3 \cdot 10^{-7}$

Table 8.1: The average nucleation time, obtained from BD simulations, to form a critical cluster that grew out and filled the box. The last column contains the rate (k) in units of D_0/σ^5 where D_0 is the short-time diffusion coefficient. M is the number of separate simulations used to calculate the rate. Each simulation consisted of 4096 particles.

particle to be identified as crystalline denoted ξ_c, and the symmetry index for the bond orientational order parameter l. Similar to the hard-sphere case, the nucleus is expected to have random hexagonal order and thus we set $l = 6$. Additionally, as in the hard-sphere case we used $d_c = 0.7$. The value of ξ is set to 8 and r_c is always either 1.5 or 1.6 and will be explicitly indicated in each section.

8.3.1 Brownian dynamics

The nucleation rate from BD simulations can be determined in the same manner as the nucleation rate from molecular dynamics simulations. Starting with configurations in the metastable fluid, we ran a number of BD simulations and determined the average time ($< t >$) before the largest cluster in our system exceeded the critical size. The nucleation rate k is then

$$k = \frac{1}{< t > V}, \tag{8.2}$$

where V is the volume of the system.

The results from our BD simulations are shown in Table 8.1. Note that we also tried to calculate the nucleation rates for a number density of $\rho = 0.774$ using BD, however, after 5 simulations, corresponding to a total simulation length $12000\sigma^2/6D_0$, a critical nucleus had still not formed.

8.3.2 Umbrella sampling

In this section, we use umbrella sampling to determine the Gibbs free-energy barriers, and then calculate the crystal nucleation rates from these barriers. The method for predicting the Gibbs free-energy barriers and extracting crystal nucleation rates from such barriers is described in detail in Chapter 6.5. For pressures $\beta p\sigma^3 = 12$ and 13, the free energy barriers are shown in Figure 8.3 and the nucleation rates are listed in Table 8.2.

8.3.3 Forward flux sampling

We use forward flux sampling to determine the nucleation rates for pressures $\beta p\sigma^3 = 12, 13$ and 14. The method is the same as the one used in Chapter 6 in determining the crystal nucleation rates for hard spheres. For a complete description of the method see Chapter 6.6. The dynamics in the forward flux sampling simulations were approximated using

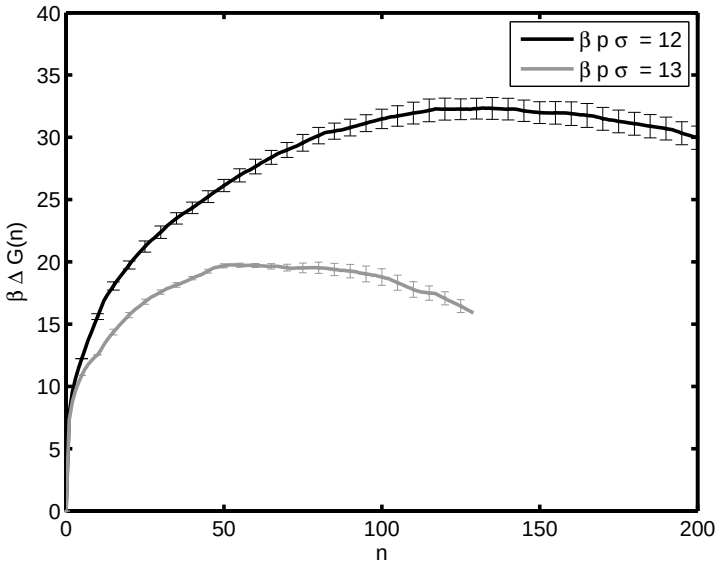

Figure 8.3: Gibbs free-energy barriers $\beta\Delta G(n)$ as a function of cluster size n as obtained from umbrella sampling MC simulations at reduced pressures $\beta p\sigma^3 = 12$ and 13 as labelled. The neighbour cutoff is $r_c = 1.5$.

$\beta p\sigma^3$	f_{n^*}/D_0	$\Delta G(n^*)$	$\Delta G''(n^*)$	$k\sigma^5/D_0$
12	586.17	32.5	0.0014622	$4.8767 \cdot 10^{-14}$
13	319.05	20	0.0016641	$8.3208 \cdot 10^{-9}$

Table 8.2: Nucleation rates k in units of D_0/σ^5 with D_0 the short-time diffusion coefficient as a function of reduced pressure ($\beta p\sigma^3$) as predicted by umbrella sampling. $G''(n^*)$ is the second order derivative of the Gibbs free energy at the critical nucleus size n^* and f_{n^*}/D_0 is the attachment rate.

kinetic Monte Carlo simulations with a step size of $\Delta_{\mathrm{KMC}} = 0.05\sigma$ and measuring the order parameter every $\Delta t_{\mathrm{ord}} = 2$ MC cycles. The nearest neighbour cutoff for the order parameter is $r_c = 1.5$. The probabilities $P(\lambda_i|\lambda_{i-1})$ of going from interface λ_{i-1} to λ_i required in the forward flux sampling rate calculation for pressures $\beta p\sigma^3 = 12, 13$ and 14 are given in Tables 8.3, 8.4 and 8.5 respectively. The resulting rates in units of the short-time diffusion coefficient D_0 are given in Table 8.6 .

8.4 Discussion

In Figure 8.4 we show our predicted WCA crystal nucleation rates and compare them with those found in Ref. [113]. We note that the nucleation rates found in Ref. [113], have been plotted as a function of an "effective" packing fraction ϕ_K^{eff} where the effective particle diameter was taken to be the solution to $\beta U(\sigma_{\mathrm{eff}}) = 1$, i.e. $\sigma_{\mathrm{eff}} = 1.09\sigma$. Hence, we have rescaled their rates to be in units of number density $\rho\sigma^3$. We note that the uncertainty in the BD results is approximately one order of magnitude and the uncertainty in the US and FFS results is approximately two orders of magnitude. Strangely, while our BD,

i	λ_i	$P(\lambda_i\|\lambda_{i-1})$
2	20	0.133
3	26	0.132
4	34	0.107
5	45	0.068
6	60	0.066
7	80	0.041
8	110	0.036
9	150	0.130
10	200	0.317
11	250	0.842

Table 8.3: Probabilities $P(\lambda_{i+1}|\lambda_i)$ for the interfaces used in calculating the nucleation rate for pressure $\beta p\sigma^3 = 12$.

i	λ_i	$P(\lambda_i\|\lambda_{i-1})$
2	20	0.132
3	30	0.124
4	40	0.193
5	60	0.132
6	100	0.166
7	150	0.633

Table 8.4: Probabilities $P(\lambda_{i+1}|\lambda_i)$ for the interfaces used in calculating the nucleation rate for pressure $\beta p\sigma^3 = 13$.

i	λ_i	$P(\lambda_i\|\lambda_{i-1})$
2	40	0.164
3	70	0.453
4	100	0.847

Table 8.5: Probabilities $P(\lambda_{i+1}|\lambda_i)$ for the interfaces used in calculating the nucleation rate for pressure $\beta p\sigma^3 = 14$.

$\beta p\sigma^3$	$\Phi_{A\lambda_1}\sigma^5/D_0$	$P(\lambda_B\|\lambda_1)$	$k\sigma^5/D_0$
12	$2.96 \cdot 10^{-6}$	$4.32 \cdot 10^{-10}$	$1.27 \cdot 10^{-15}$
13	$1.10 \cdot 10^{-5}$	$4.38 \cdot 10^{-5}$	$4.80 \cdot 10^{-10}$
14	$1.06 \cdot 10^{-5}$	$6.29 \cdot 10^{-2}$	$6.69 \cdot 10^{-7}$

Table 8.6: Nucleation rate $k\sigma^5/D_0$, flux $\Phi_{A\lambda_1}$, and $P(\lambda_B|\lambda_1)$ as a function of pressure predicted by forward flux sampling.

$\beta p\sigma^3$	$\beta \lvert\Delta\mu\rvert$	ρ_{liq}	ρ_{sol}	ϕ_K^{eff}
12.0	0.42	0.762	0.844	0.524
12.5	0.48	0.769	0.851	0.529
13.0	0.54	0.775	0.858	0.533
13.5	0.61	0.780	0.864	0.537
14.0	0.66	0.786	0.870	0.541
14.6	0.73	0.794	0.876	0.546

Table 8.7: Reduced pressure ($\beta p\sigma^3$), reduced chemical potential difference between the fluid and solid phases($\beta \lvert\Delta\mu\rvert$), reduced number density of the metastable liquid ρ_{liq}, reduced number density of the solid phase ρ_{sol}, and the effective packing fraction ϕ_K^{eff} as defined in Ref. [113] for the state points studied in this chapter.

US, and FFS rates all agree with the uncertainty, we do not find agreement between our BD results and the BD results of Ref. [113]. At the time this thesis was written, this discrepancy was still not understood. Note that an overview of the nucleation parameters for the state points discussed in this section is found in Table 8.7.

We further compare our WCA results with those of the hard-sphere system examined in Chapter 6. To do this, we scale our WCA results in terms of an effective packing fraction in the same manner as is done experimentally. Specifically, we scale the freezing number density of the WCA model ($\rho_F\sigma^3 = 0.712$) to the freezing packing fraction of hard spheres. Note that in literature there is a range of freezing packing fractions for hard spheres, namely $0.491 \leq \phi_F^{HS} \leq 0.494$ (see, e.g. [12, 20, 137]). Here we follow Frenkel and Smit [20] which we believe to be the most accurate. In their work, finite size effects are taken into consideration when calculating the free energy of the face-centered-cubic (FCC) crystal, i.e. they use the result from Ref. [61]. They use the Speedy equations of state for the solid and fluid [60, 111]. The resulting freezing packing fraction is found to be $\phi_F^{HS} = 0.492$ [20]. The WCA nucleation rates scaled to $\phi_F^{HS} = 0.492$ are compared to the hard-sphere results in Figure 8.5. We would like to point out here that any error in the freezing coexistence points results in a horizontal shift in the nucleation rates. Hence, in addition to an uncertainty of approximately 2 orders of magnitude in the nucleation rates, there is an additional uncertainty of approximately $\Delta\phi_{\text{error}} = \pm 0.005$ in the effective packing fractions. Thus, within these error bars, we find good agreement between our predicted hard-sphere and WCA crystal nucleation rates.

Additionally, we use the free energies for the hard-sphere model and the WCA model to determine the associated supersaturations $\beta\Delta\mu$. The nucleation rates as a function of supersaturation are shown in Figure 8.6. Also included in this plot are the crystal nucleation rates associated with two other models plotted in Figure 8.1, namely an effective

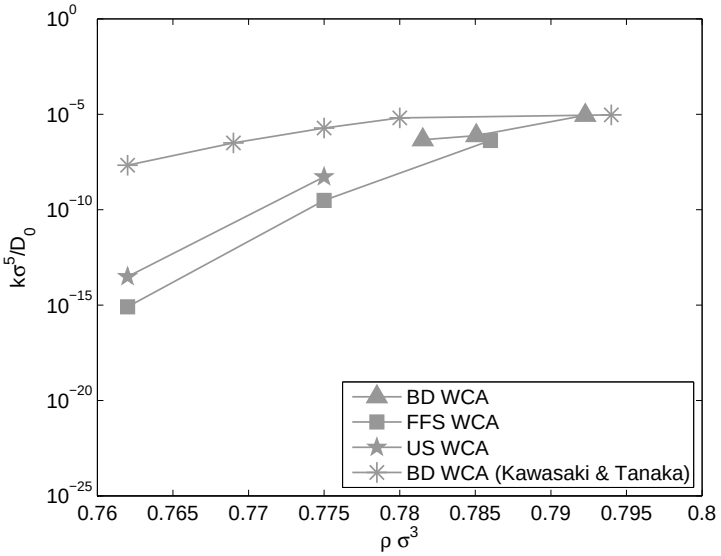

Figure 8.4: Crystal nucleation rates $k\sigma^5/D_0$ as a function of number density $\rho\sigma^3$ where D_0 is the short-time diffusion coefficient. While we have not included error bars in this plot, note that the uncertainty in the US and FFS nucleation rates is approximately 2 orders of magnitude while the uncertainty in the BD results is approximately 1 order of magnitude.

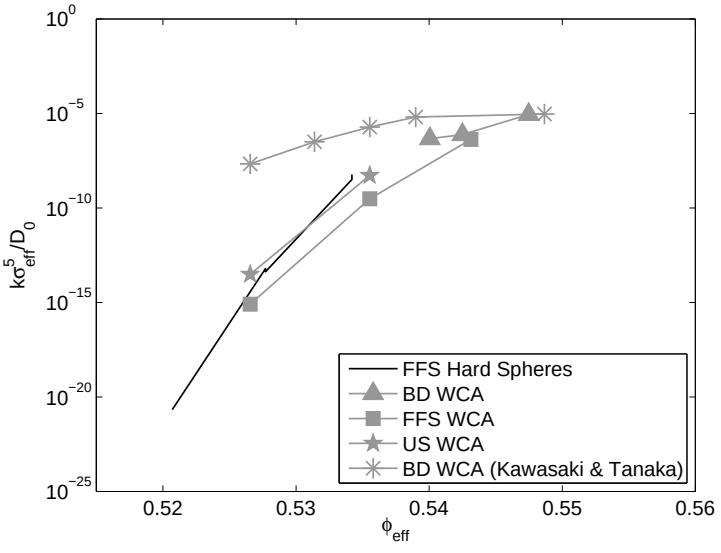

Figure 8.5: Crystal nucleation rates $k\sigma_{\text{eff}}^5/D_0$ as a function of effective packing fraction ϕ_{eff} where D_0 is the short-time diffusion coefficient. Note that σ_{eff} is the size of a hard-sphere particle which has the same freezing number density as the WCA model. The hard-sphere nucleation rates are taken from Chapter 6.

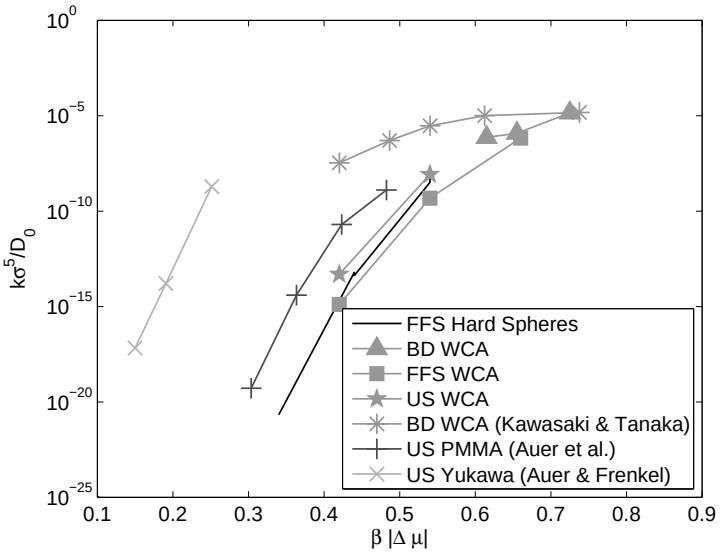

Figure 8.6: Crystal nucleation rates $k\sigma_{\text{eff}}^5/D_0$ for particles interacting via the WCA potential, as well as the other potentials plotted in Figure 8.1, as a function of supersaturation $|\beta\Delta\mu|$ where D_0 is the short-time diffusion coefficient. The hard-sphere crystal nucleation rates are taken from Chapter 6, and the PMMA and Yukawa results are taken from Refs. [114] and [115] respectively.

model for PHSA coated PMMA colloids *, and the hard-core Yukawa potential †. The rates for these two models are taken from Refs. [114] and [115] respectively. Note that in Refs. [114] and [115] the authors have attempted to correct for hydrodynamics by writing the nucleation rates in terms of the short-time self-diffusion coefficient D_S which they relate to the short-time diffusion coefficient D_0 by $D_S/D_0 = (1 - \phi_{\text{eff}}/0.64)^{1.17}$. In this expression ϕ_{eff} is a scaled packing fraction determined by setting the freezing packing fraction equal to that of hard spheres. Unfortunately, we do not know the exact values of ϕ_{eff} that were used to scale the nucleation rates, however, in the range of interest, D_S/D_0

*The steric interaction between PHSA coated PMMA colloids is approximated using the Alexander-de Gennes model [138]. This model approximates the interaction between plates with an absorbed polymer layer in a good solvent with a high coverage of the polymer capping molecules. To transform this interaction between plates to an interaction between spheres of diameter σ the Derjaguin approximation [138] is used. The resulting interaction between the spheres is given by

$$\beta V_{\text{steric}}(r) = \begin{cases} \infty & r < \sigma \\ \frac{16\pi\alpha\sigma L^2}{70 s^3}\left[28(x^{-1/4} - 1) + \frac{20}{11}(1 - x^{11/4}) + 12(x - 1)\right] & \sigma \leq r < \sigma + 2L \\ 0 & \text{otherwise} \end{cases}$$

where $x = (r - \sigma)/(2L)$, s is the mean distance between attachment points of the capping ligands and L is the thickness of the capping layer.

†The hard-core Yukawa potential is given by

$$\beta V_{\text{yukawa}}(r) = \begin{cases} \beta\epsilon \frac{\exp(-\kappa(r/\sigma - 1))}{r/\sigma} & r \geq \sigma \\ \infty & r < \sigma \end{cases} \tag{8.3}$$

where κ is the screening length and ϵ is the contact value of the potential.

is always on the order of 0.1. Thus, in order to plot the results of Refs. [114] and [115] in units of D_0 we un-scale the results using the approximation that $D_0/D_S = 10$. Note that the nucleation rates of the hard spheres, the WCA model and the PHSA-coated PMMA particles are all within a few orders of magnitude. In contrast, the nucleation rates for the much softer Yukawa potential start to drop off at much lower supersaturations.

8.5 Conclusions

In conclusion, we have examined the crystal nucleation of particles interacting with the WCA potential with $\beta\epsilon = 40$ using Brownian dynamics, umbrella sampling and forward flux sampling. As in Chapter 6, we find good agreement between the nucleation rates predicted using these different methods. Additionally, we find that the nucleation rates predicted for the WCA model agree well with those of hard spheres both as a function of the supersaturation as well as effective packing fraction. Note that we have defined the effective packing fraction such that the effective packing fraction at freezing matches that of hard spheres. Our Brownian dynamics rates, however, differ significantly from those by Kawasaki and Tanaka [113], a point which was still not understood when this thesis was written.

8.6 Acknowledgements

I would like to thank Ran Ni for his work on the umbrella sampling and Brownian dynamics nucleation rates. I would also like to thank Matthieu Marechal for use of his Brownian dynamics code, and Frank Smallenburg and Daan Frenkel for many useful discussions.

Colour figures

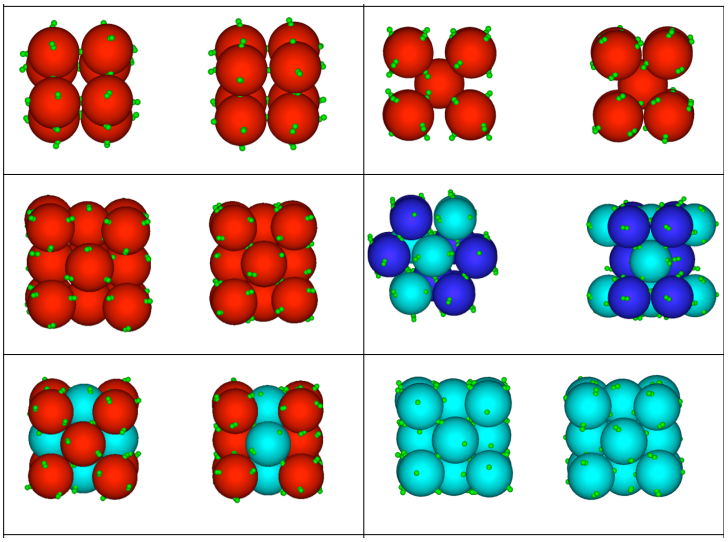

Figure 4.6: The figure shows the unit cells of (from left to right, from up to down): the fully bonded SC crystal, the fully bonded BCT c rystal, the fully bonded FCC crystal (all of them with energy per particle e=-3), the HCP unit cell whose average energy per particle is $e = -2.25$, and two partially bonded FCC crystals, with average energy respectively $e = -2.5$ and $e = -2.0$. Note that the number of bonds per particle is indicated by the colour, red for 6 bonds, blue for 5 bonds and turquoise for 4 bonds.

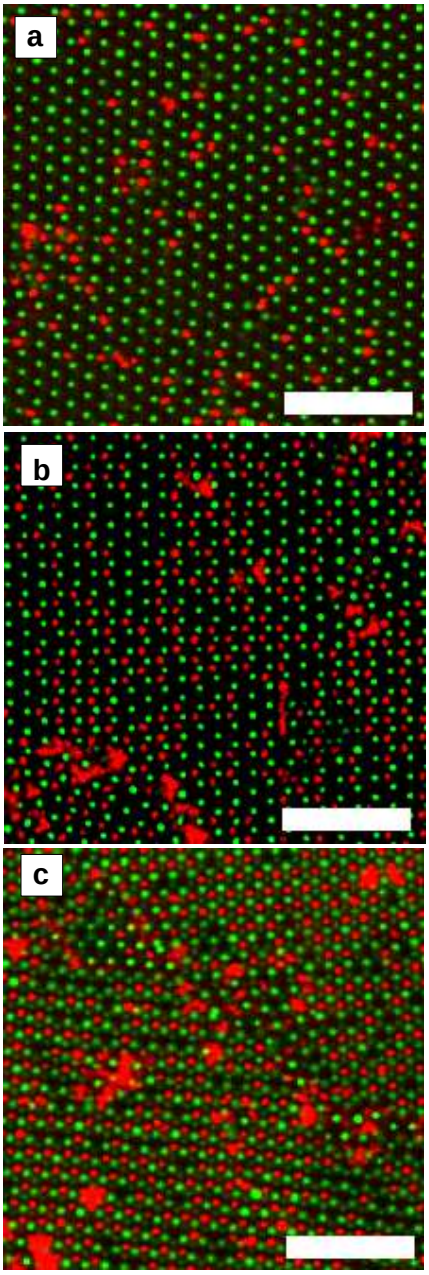

Figure 5.14: Confocal images of an interstitial solid solution with size ratio $q = 0.3$ for various stoichometries. The labels **a**, **b**, and **c** correspond to confocal images of the ISS with $n \simeq 0.1$, 0.3 and 0.8, respectively. In these images two (111) planes of the crystal, one consisting of mostly small (red) particles with the other consisting of mostly large (green) particles have been overlayed in order to be viewable in the same figure. The larger and darker red regions correspond to defects, such as vacancies, in the underlying lattice of green particles which have been filled by many small (red) particles. Scalebars are 10 μm.

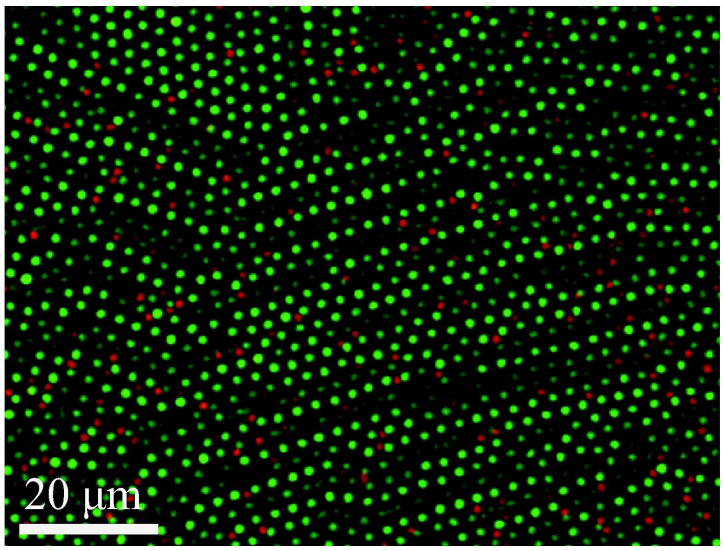

Figure 5.16: Typical confocal image of the ISS structure found in a binary system of oppositely charged PMMA particles with size ratio σ_S/σ_L=0.73 dispersed in a mixture of 23.7 wt% cis-decahydron aphthalene and 76.3 w% cyclohexylbromide. The large (green) and small (red) particles have a diameter 1.88 μm (polydispersity 3 %) and 1.37 μm (polydispersity 5 %) respectively. The overall packing fraction was $\eta = 0.2$. The large particles mutually repel each other and formed a crystal lattice. The small particles were found on random positions in between the lattice. See Figure 5.17 for more details.

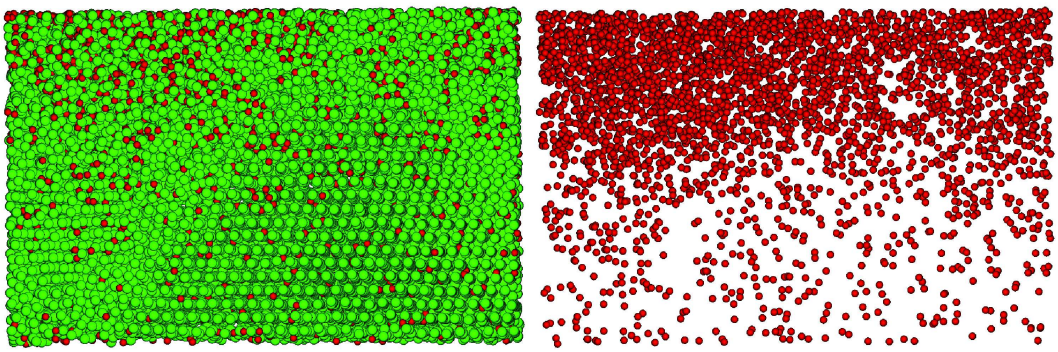

Figure 5.17: 3-D reconstruction of an interstitial solid solution in a binary mixture of oppositely charged colloids. Left: Rendered 3-D reconstruction from a stack of 244 confocal images with a spacing of 0.25 μm between them corresponding to the system described in Figure 5.16. We identified a face-centred-cubic lattice of the mutually repelling large particles with a lattice parameter for the cubic unit cell of $a \approx 3.8$ μm. In the lower part of the sample an ISS was formed with a fluid on top of it. Whereas the large particles do not touch each other, the small particles were found to stick to one or more large particles in the lattice. This, in addition to the observation that the small particles do not appear to occupy a position on the lattice of the large particles demonstrates that the large and small particles were oppositely charged. Right: The same 3-D reconstruction showing only the small particles in the fluid (top) and the ISS (below). We note that in sequential confocal images, some of the small particles were observed hopping from one interstitial site to another.

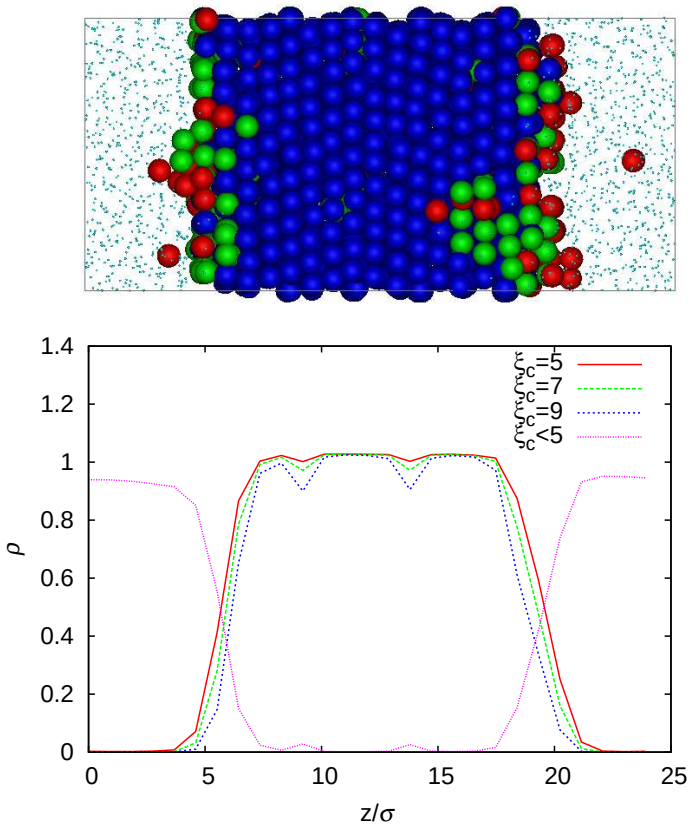

Figure 6.1: Top: A typical configuration of an equilibrated random-hexagonal-close-packed (RHCP) crystal in coexistence with an equilibrated fluid. The crystalline particles are labelled according to three different crystallinity criteria: the red particles have between $\xi = 5$ and 6 crystalline bonds, the green particles have between $\xi = 7$ and 8 crystalline bonds and the blue particles have $\xi \geq 9$ or more crystalline bonds. The fluid-like particles ($\xi < 5$) are denoted by dots. Bottom: The density profile of particles with a minimum number of neighbours ξ as labelled. Note that the dips in the density profile correspond to HCP stacked layers. This implies that near the interface, the order parameter is slightly more sensitive to FCC ordered particles than to HCP ordered particles.

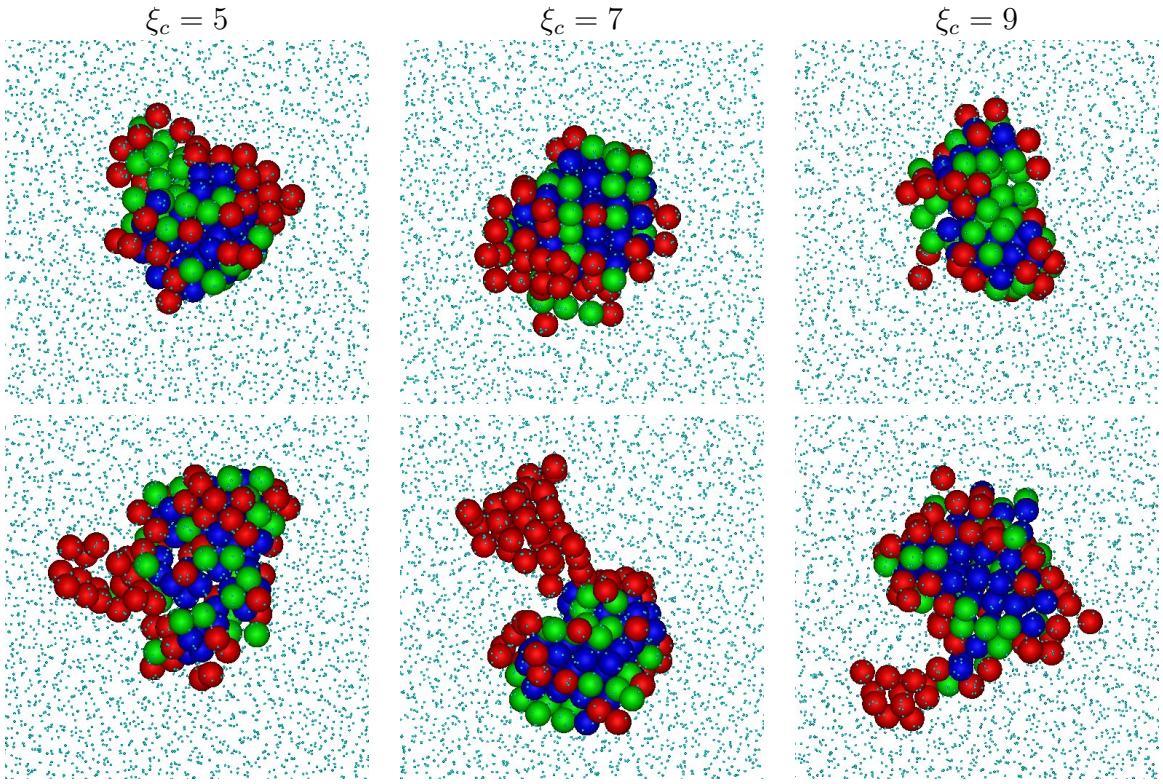

Figure 6.12: Two typical snapshots (top and bottom) of the critical nuclei as obtained with US at a volume fraction $\eta = 0.5355$ using different values of the critical number of crystalline bonds $\xi_c = 5$ (left), 7 (middle) and 9 (right) in the biasing potential. The clusters are analyzed with three different crystalline order parameters. The blue particles are found by all three cluster criteria, the green particles have $\xi = 7$ or 8 crystalline bonds and the red particles have only $\xi = 5$ or 6 crystalline bonds.

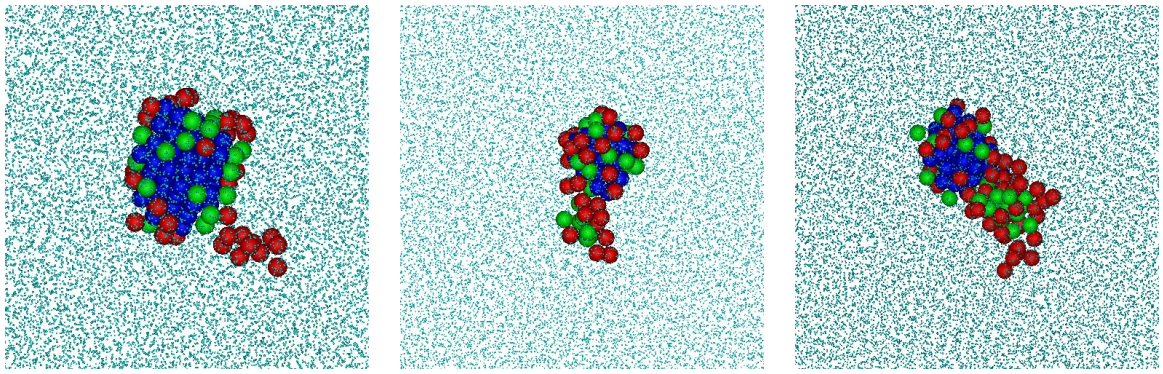

Figure 6.13: Snapshots of spontaneously formed nuclei during an MD simulation at a volume fraction of $\eta = 0.537$. The snapshots were taken just before the nuclei grew. The colour coding of the particles is the same as in Figure 6.12.

References

[1] A. Einstein, *Über die von der molekularkinetischen theorie der wärme geforferte bewegung von in ruhenden flüssigkeiten suspendierten teilchen.* Ann. Phys. (Leipz.), 17:549, 1905.

[2] W. Sutherland, *A dynamical theory of diffusion for non-electrolytes and the molecular mass of albumin.* Phil. Mag., 9:781, 1905.

[3] Y. A. Vlasov, X. Bo, J. C. Sturm, and D. J. Norris, *On-chip natural assembly of silicon photonic bandgap crystals.* Nature, 414:289–293, 2001.

[4] E. A. Kamenetzky, L. G. Magliocco, and H. P. Panzer, *Structure of solidified colloidal array laser filters studied by cryogenic transmission electron microscopy.* Science, 263:207–210, 1994.

[5] J. G. C. Veinot, H. Yan, S. M. Smith, J. Cui, Q. Huang, and T. J. Marks, *Fabrication and properties of organic Light-Emitting "Nanodiode" arrays.* Nano Letters, 2:333–335, 2002.

[6] M. J. Murray and J. V. Sanders, *Close-packed structures of spheres of two different sizes II. The packing densities of likely arrangements.* Philosophical Magazine A, 42:721, 1980.

[7] J. V. Sanders, *Close-packed structures of spheres of two different sizes I. observations on natural opal.* Philosophical Magazine A,, 42:705, 1980.

[8] S. C. Glotzer and M. J. Solomon, *Anisotropy of building blocks and their assembly into complex structures.* Nat. Mater., 6:557, 2007.

[9] A. Yethiraj and A. van Blaaderen, *A colloidal model system with an interaction tunable from hard sphere to soft and dipolar.* Nature, 421:513, 2003.

[10] W. W. Wood and J. D. Jacobson, *Preliminary results from a recalculation of the monte carlo equation of state of hard spheres.* J. Chem. Phys., 27:1207, 1957.

[11] B. J. Alder and T. E. Wainwright, *Phase transition for a hard sphere system.* J. Chem. Phys, 27:1208, 1957.

[12] W. G. Hoover and F. H. Ree, *Melting transition and communal entropy for hard spheres.* J. Chem. Phys., 49:3609, 1968.

[13] E. Parthé, *Space filling of crystal structures: A contribution to the graphical presentation of geometrical relationships in simple crystal structures.* Zeitschrift für Kristallographie, 115:52, 1961.

[14] M. Dijkstra, R. van Roij, and R. Evans, *Phase diagram of highly asymmetric binary hard-sphere mixtures.* Phys. Rev. E, 59:5744, 1999.

[15] E. Trizac, M. D. Eldridge, and P. A. Madden, *Stability of the AB crystal for asymmetric binary hard sphere mixtures.* Mol. Phy., 90:675, 1997.

[16] M. D. Eldridge, P. A. Madden, P. N. Pusey, and P. Bartlett, *Binary hard-sphere mixtures: a comparison between computer simulation and experiment.* Mol. Phys., 84:395–420, 1995.

[17] M. D. Eldridge, P. A. Madden, and D. Frenkel, *Entropy-driven formation of a superlattice in a hard-sphere binary mixture.* Nature, 365:35, 1993.

[18] A. Hynninen, L. Filion, and M. Dijkstra, *Stability of LS and LS_2 crystal structures in binary mixtures of hard and charged spheres.* J. Chem. Phys., 131:064902, 2009.

[19] W. G. T. Kranendonk and D. Frenkel, *Computer simulation of solid-liquid coexistence in binary hard sphere mixtures.* Mol. Phys., 72:679, 1991.

[20] D. Frenkel and B. Smit. *Understanding Molecular Simulation: From Algorithms to Applications.* Academic Press, California, USA, 2002.

[21] D. Frenkel and A. J. C. Ladd, *New monte carlo method to compute the free energy of arbitrary solids. application to the fcc and hcp phases of hard spheres.* J. Chem. Phys., 81:3188, 1984.

[22] R. van Roij. *Lecture notes: Soft condensed matter theory*, 2007.

[23] T. C. Hales, *A proof of the Kepler conjecture.* Annals of Mathematics, 162:1065, 2005.

[24] F. X. Redl, K. Cho, C. B. Murray, and S. O'Brien, *Three-dimensional binary superlattices of magnetic nanocrystals and semiconductor quantum dots.* Nature, 423:968, 2003.

[25] Z. Chen and S. O'Brien, *Structure direction of II-VI semiconductor quantum dot binary nanoparticle superlattices by tuning radius ratio.* ACS Nano, 2:1219, 2008.

[26] K. P. Velikov, C. G. Christova, R. P. A. Dullens, and A. van Blaaderen, *Layer-by-Layer growth of binary colloidal crystals.* Science, 296:106, 2002.

[27] M. E. Leunissen, C. G. Christova, A.-P. Hynninen, C. P. Royall, A. I. Campbell, A. Imhof, M. Dijkstra, R. van Roij, and A. van Blaaderen, *Ionic colloidal crystals of oppositely charged particles.* Nature, 437:235, 2005.

[28] N. Hunt, R. Jardine, and P. Bartlett, *Superlattice formation in mixtures of hard-sphere colloids.* Phys. Rev. E, 62:900, 2000.

[29] A. B. Schofield, P. N. Pusey, and P. Radcliffe, *Stability of the binary colloidal crystals AB_2 and AB_{13}.* Phys. Rev. E, 72:031407, 2005.

[30] P. Bartlett, R. H. Ottewill, and P. N. Pusey, *Superlattice formation in binary mixtures of hard-sphere colloids.* Phys. Rev. Letts., 68:3801, 1992.

[31] S. Abbas and T. P. Lodge, *Superlattice formation in binary mixtures of block copolymer micelles.* Langmuir, 24:6247, 2008.

[32] J. H. Holland. *Adaption in Natural and Artifical Systems.* MIT Press/ Bradford Books Editions, Cambridge, MA, 1992.

[33] B. Hartke, *Global Geometry Optimization of Clusters Using Genetic Algorithms.* J. Phys. Chem., 97:9973, 1993.

[34] Y. Xiao and D. E. Williams, *Genetic algorithm: a new approach to the prediction of the structure of molecular clusters.* Chem. Phys. Letts., 215:17, 1993.

[35] D. M. Deaven and K. M. Ho, *Molecular Geometry Optimization with a Genetic Algorithm.* Phys. Rev. Letts., 75:288, 1995.

[36] A. R. Oganov and C. W. Glass, *Crystal structure prediction using ab initio evolutionary techniques: Principles and applications.* J. Chem. Phys., 124:244704, 2006.

[37] N. L. Abraham and M. I. J. Probert, *A periodic genetic algorithm with real-space representation for crystal structure and polymorph prediction.* Phys. Rev. B, 73:224104, 2006.

[38] D. Gottwald, G. Kahl, and C. N. Likos, *Predicting equilibrium structures in freezing processes.* J. Chem. Phys., 122:204503, 2005.

[39] D. P. Stucke and V. H. Crespi, *Predictions of New Crystalline States for Assemblies of Nanoparticles: Perovskite Analogues and 3-D Arrays of Self-Assembled Nanowires.* Nanoletters, 3:1183, 2003.

[40] H. T. Stokes, D. M. Hatch, and B. J. Campbell. *ISOTROPY.* stokes.byu.edu/isotropy.html, 2007.

[41] J. N. R. H. Byrd, P. Lu and C. Zhu, *A limited memory algorithm for bound constrained optimization.* SIAM J. Scientific Computing, 16:1190, 1995.

[42] D. E. Goldberg. *Genetic Algorithms in Search Optimization and Machine Learning.* Addison-Wesley Publishing, Reading, MA, 1989.

[43] C. N. Likos and C. Henley, *Complex alloy phases for binary hard-disc mixtures.* Philos. Mag. B, 68:85, 1993.

[44] J. K. Kummerfeld, T. S. Hudson, and P. Harrowell, *The densest packing of AB binary Hard-Sphere homogeneous compounds across all size ratios.* J. Phys. Chem. B, 112:10773, 2008.

[45] A. Hynninen, J. H. J. Thijssen, E. C. M. Vermolen, M. Dijkstra, and A. van Blaaderen, *Self-assembly route for photonic crystals with a bandgap in the visible region.* Nature Materials, 6:202, 2007.

[46] A. R. Denton and N. W. Ashcroft, *Weighted-density-functional theory of nonuniform fluid mixtures: Application to freezing of binary hard-sphere mixtures.* Phys. Rev. A, 42:7312, 1990.

[47] M. D. Eldridge, P. A. Madden, and D. Frenkel, *The stability of the AB_{13} crystal in a binary hard sphere system.* Mol. Phys., 79:105, 1993.

[48] K. Overgaag, W. Evers, B. de Nijs, R. Koole, J. Meeldijk, and D. Vanmaekelbergh, *Binary superlattices of PbSe and CdSe nanocrystals.* J. Am. Chem. Soc., 130:7833, 2008.

[49] A. B. Schofield, *Binary hard-sphere crystals with the cesium chloride structure.* Phys. Rev. E, 64:051403, 2001.

[50] S. Yoshimura and S. Hachisu, *Order formation in binary mixtures of monodisperse latices.* Progress in Colloid and Polymer Science, 68:59, 1983.

[51] E. C. M. Vermolen, A. Kuijk, L. C. Filion, M. Hermes, J. H. J. Thijssen, M. Dijkstra, and A. van Blaaderen, *Fabrication of large binary colloidal crystals with a NaCl structure.* Proc. National Academy of Sciences, 106:16063, 2009.

[52] F. Laves. *Theory of Alloy Phases.* American Society for Metals, Metals Park, OH, 1956.

[53] P. G. Bolhuis, D. Frenkel, S. Mau, and D. A. Huse, *Entropy difference between crystal phases.* Nature, 388:235, 1997.

[54] P. Bartlett, R. H. Ottewill, and P. N. Pusey, *Freezing of binary mixtures of colloidal hard spheres.* J. Chem. Phys., 93:1299, 1990.

[55] X. Cottin and P. A. Monson, *A cell theory for solid solutions: Application to hard sphere mixtures.* J. Chem. Phys., 99:8914, 1993.

[56] X. Cottin and P. A. Monson, *Substitutionally ordered solid solutions of hard spheres.* J. Chem. Phys., 102:3354, 1995.

[57] W. G. T. Kranendonk and D. Frenkel, *Free energy calculations for solid solutions by computer simulations.* Mol. Phys., 72:699, 1991.

[58] W. G. T. Kranendonk and D. Frenkel, *Thermodynamic properties of binary hard sphere mixtures.* Mol. Phys., 72:715, 1991.

[59] G. A. Mansoori, N. F. Carnahan, K. E. Starling, and J. Leland, *Equilibrium thermodynamic properties of the mixture of hard spheres.* J. Chem. Phys., 54:1523, 1971.

[60] R. J. Speedy, *Pressure and entropy of hard-sphere crystals.* J. Phys.: Condensed. Matter, 10:4387, 1998.

[61] J. M. Polson, E. Trizac, S. Pronk, and D. Frenkel, *Finite-size corrections to the free energies of crystalline solids.* J. Chem. Phys., 112:5339, 2000.

[62] M. Abramowitz and I. Stegun. *Handbook of Mathematical Functions.* Dover, New York, 1970.

[63] S. M. Woodley and R. Catlow, *Crystal structure prediction from first principles.* Nat Mater, 7:937, 2008.

[64] J. Pannetier, J. Bassas-Alsina, J. Rodriguez-Carvajal, and V. Caignaert, *Prediction of crystal structures from crystal chemistry rules by simulated annealing.* Nature, 346:343, 1990.

[65] H. R. Karfunkel and R. J. Gdanitz, *Ab initio prediction of possible crystal structures for general organic molecules.* J. Comput. Chem., 13:1171, 1992.

[66] S. Torquato and Y. Jiao, *Dense packings of the platonic and archimedean solids.* Nature, 460:876, 2009.

[67] V. Buch, R. Martoňák, and M. Parrinello, *Exploration of NVE classical trajectories as a tool for molecular crystal structure prediction, with tests on ice polymorphs.* J. Chem. Phys., 124:204705, 2006.

[68] M. Parrinello and A. Rahman, *Crystal structure and pair potentials: A Molecular-Dynamics study.* Phys. Rev. Letts., 45:1196, 1980.

[69] R. Najafabadi and S. Yip, *Observation of finite-temperature bain transformation (f.c.c. –>r b.c.c.) in monte carlo simulation of iron.* Scripta Metall., 17:1199, 1983.

[70] D. J. Wales and H. A. Scheraga, *Global optimization of clusters, crystals, and biomolecules.* Science, 285:1368, 1999.

[71] V. N. Manoharan, M. T. Elsesser, and D. J. Pine, *Dense packing and symmetry in small clusters of microspheres.* Science, 301:483, 2003.

[72] D. J. Kraft, W. S. Vlug, C. M. van Kats, A. van Blaaderen, A. Imhof, and W. K. Kegel, *Self-assembly of colloids with liquid protrusions.* J. Am. Chem. Soc., 131:1182, 2009.

[73] P. Bartlett and A. I. Campbell, *Three-dimensional binary superlattices of oppositely charged colloids.* Phys. Rev. Letts., 95:128302, 2005.

[74] E. V. Shevchenko, D. V. Talapin, C. B. Murray, and S. O'Brien, *Structural characterization of Self-Assembled multifunctional binary nanoparticle superlattices.* J. Am. Chem. Soc., 128:3620, 2006.

[75] J. C. Schon, Z. P. CanCarevic, A. Hannemann, and M. Jansen, *Free enthalpy landscape of sro.* J. Chem. Phys., 128:194712, 2008.

[76] L. Filion and M. Dijkstra, *Prediction of binary hard-sphere crystal structures.* Phys. Rev. E, 79:046714, 2009.

[77] A. Hynninen and M. Dijkstra, *Phase diagram of dipolar hard and soft spheres: Manipulation of colloidal crystal structures by an external field.* Phys. Rev. Letts., 94:138303, 2005.

[78] S. Toxvaerd, U. R. Pedersen, T. B. Schrøder, and J. C. Dyre, *Stability of supercooled binary liquid mixtures.* J. Chem. Phys., 130:224501, 2009.

[79] D. Gottwald, C. N. Likos, G. Kahl, and H. Löwen, *Ionic microgels as model systems for colloids with an ultrasoft electrosteric repulsion: Structure and thermodynamics.* J. Chem. Phys., 122:074903, 2005.

[80] M. Watzlawek, C. N. Likos, and H. Löwen, *Phase diagram of star polymer solutions.* Phys. Rev. Letts., 82:5289, 1999.

[81] M. Marechal, R. J. Kortschot, A. F. Demirörs, A. Imhof, and M. Dijkstra, *Phase behavior and structure of a new colloidal model system of Bowl-Shaped particles.* Nano Letters, 10:1907, 2010.

[82] E. Bianchi, J. Largo, P. Tartaglia, E. Zaccarelli, and F. Sciortino, *Phase diagram of patchy colloids: towards empty liquids.* Phys. Rev. Lett., 97:168301, 2006.

[83] M. Wojcik and K. E. Gubbins, *Thermodynamics and structure of hard oblate spherocylinder fluids.* Mol. Phys., 53:397, 1984.

[84] A. Cuetos and B. Martínez-Haya, *Columnar phases of discotic spherocylinders.* J. Chem. Phys., 129:214706, 2008.

[85] J. A. C. Veerman and D. Frenkel, *Phase behavior of disklike hard-core mesogens.* Phys. Rev. A, 45:5632, 1992.

[86] M. Marechal. *Anisotropic colloids: bulk behaviour and equilibrium sedimentation.* PhD thesis, Utrecht University, 2009.

[87] M. A. Bates and D. Frenkel, *Infinitely thin disks exhibit a first order nematic-columnar phase transition.* Phys. Rev. E, 57:4824, 1998.

[88] B. Sakintuna, F. Lamari-Darkrim, and M. Hirscher, *Metal hydride materials for solid hydrogen storage: A review.* International Journal of Hydrogen Energy, 32:1121, 2007.

[89] A. Vrij, *Polymers at interfaces and the interactions in colloidal dispersions.* Pure and Applied Chemistry, 48:471, 1976.

[90] P. N. Pusey and W. van Megen, *Phase behaviour of concentrated suspensions of nearly hard colloidal spheres.* Nature, 320:340, 1986.

[91] B. J. Alder and T. E. Wainwright, *Studies in molecular dynamics. i. general method.* J. Chem. Phys., 31:459, 1959.

[92] B. Götzelmann, R. Evans, and S. Dietrich, *Depletion forces in fluids.* Phys. Rev. E, 57:6785, 1998.

[93] M. P. Lettinga and E. Grelet, *Self-Diffusion of rodlike viruses through smectic layers.* Phys. Rev. Lett., 99:197802, 2007.

[94] R. Piazza, T. Bellini, and V. Degiorgio, *Equilibrium sedimentation profiles of screened charged colloids: A test of the hard-sphere equation of state.* Phys. Rev. Lett., 71:4267, 1993.

[95] M. A. Rutgers, J. H. Dunsmuir, J. Xue, W. B. Russel, and P. M. Chaikin, *Measurement of the hard-sphere equation of state using screened charged polystyrene colloids.* Phys. Rev. B, 53:5043, 1996.

[96] J. P. Hoogenboom, P. Vergeer, and A. van Blaaderen, *A real-space analysis of colloidal crystallization in a gravitational field at a flat bottom wall.* J. Chem. Phys., 119:3371, 2003.

[97] O. L. Pursiainen, J. J. Baumberg, H. Winkler, B. Viel, P. Spahn, and T. Ruhl, *Nanoparticle-tuned structural color from polymer opals.* Optics Express, 15:9553, 2007.

[98] A. D. Dinsmore, E. R. Weeks, V. Prasad, A. C. Levitt, and D. A. Weitz, *Three-dimensional confocal microscopy of colloids.* Appl. Optics, 40:4152, 2001.

[99] S. Lee, Y. Roichman, G. Yi, S. Kim, S. Yang, A. van Blaaderen, P. van Oostrum, and D. G. Grier, *Characterizing and tracking single colloidal particles with video holographic microscopy.* Opt. Express, 15:18275, 2007.

[100] J. L. Harland and W. van Megen, *Crystallization kinetics of suspensions of hard colloidal spheres.* Phys. Rev. E, 55:3054, 1997.

[101] C. Sinn, A. Heymann, A. Stipp, and T. Palberg, *Solidification kinetics of hard-sphere colloidal suspensions.* Prog. Colloid Polym. Sci., 118:266, 2001.

[102] K. Schätzel and B. J. Ackerson, *Density fluctuations during crystallization of colloids.* Phys. Rev. E, 48:3766, 1993.

[103] S. Auer and D. Frenkel, *Prediction of absolute crystal-nucleation rate in hard-sphere colloids.* Nature, 409:1020, 2001.

[104] G. M. Torrie and J. P. Valleau, *Monte carlo free energy estimates using non-Boltzmann sampling: Application to the sub-critical Lennard-Jones fluid.* Chem. Phys. Lett., 28:578, 1974.

[105] J. S. van Duijneveldt and D. Frenkel, *Computer simulation study of free energy barriers in crystal nucleation.* J. Chem. Phys., 96:4655, 1992.

[106] R. Ni, S. Belli, R. van Roij, and M. Dijkstra, *Glassy dynamics, spinodal fluctuations, and the kinetic limit of nucleation in suspensions of colloidal hard rods.* Phys. Rev. Letts., 105:088302, 2010.

[107] R. J. Allen, P. B. Warren, and P. R. ten Wolde, *Sampling rare switching events in biochemical networks.* Phys. Rev. Lett, 94:018104, 2005.

[108] R. J. Allen, D. Frenkel, and P. R. ten Wolde, *Simulating rare events in equilibrium or nonequilibrium stochastic systems.* J. Chem. Phys., 124:024102, 2006.

[109] R. J. Allen, D. Frenkel, and P. R. ten Wolde, *Forward flux sampling-type schemes for simulating rare events: Efficiency analysis.* J. Chem. Phys., 124:194111, 2006.

[110] P. N. Pusey, E. Zaccarelli, C. Valeriani, E. Sanz, W. C. K. Poon, and M. E. Cates, *Hard spheres: crystallization and glass formation.* Philos. T. Roy. Soc. A, 367:4993–5011, 2009.

[111] R. J. Speedy, *Pressure of the metastable hard-sphere fluid.* J. Phys.: Condensed. Matter, 9:8591–8599, 1997.

[112] J. T. Padding and A. A. Louis, *Interplay between hydrodynamic and brownian fluctuations in sedimenting colloidal suspensions.* Phys. Rev. E, 77:011402, 2008.

[113] T. Kawasaki and H. Tanaka, *Formation of a crystal nucleus from liquid.* Proceedings of the National Academy of Sciences, 107:14036, 2010.

[114] S. Auer, W. C. K. Poon, and D. Frenkel, *Phase behavior and crystallization kinetics of poly-12-hydroxystearic-coated polymethylmethacrylate colloids.* Phys. Rev. E, 67:020401, 2003.

[115] S. Auer and D. Frenkel, *Crystallization of weakly charged colloidal spheres: a numerical study.* J. Phys.: Cond. Matter, 14:7667, 2002.

[116] P. ten Wolde, M. J. Ruiz-Montero, and D. Frenkel, *Simulation of homogeneous crystal nucleation close to coexistence.* Faraday Discuss., 104:93, 1996.

[117] P. R. ten Wolde. *Numerical Study of the Pathways for Homogeneous Nucleation.* PhD thesis, University of Amsterdam, 1998.

[118] E. Zaccarelli, C. Valeriani, E. Sanz, W. C. K. Poon, M. E. Cates, and P. N. Pusey, *Crystallization of Hard-Sphere glasses.* Phys. Rev. Lett., 103:135704, 2009.

[119] P. R. ten Wolde, M. J. Ruiz-Montero, and D. Frenkel, *Numerical calculation of the rate of crystal nucleation in a Lennard-Jones system at moderate undercooling.* J. Chem. Phys., 104:9932, 1996.

[120] S. Auer and D. Frenkel, *Numerical prediction of absolute crystallization rates in hard-sphere colloids.* J. Chem. Phys., 120:3015, 2004.

[121] R. L. Davidchack, J. R. Morris, and B. B. Laird, *The anisotropic hard-sphere crystal-melt interfacial free energy from fluctuations.* J. Chem. Phys., 125:094710, 2006.

[122] S. Ryu and W. Cai, *Validity of classical nucleation theory for ising models.* Phys. Rev. E, 81:030601, 2010.

[123] I. J. Ford, *Nucleation theorems, the statistical mechanics of molecular clusters, and a revision of classical nucleation theory.* Phys. Rev. E, 56:5615, 1997.

[124] B. B. Laird, *The solid-liquid interfacial free energy of close-packed metals: Hard-spheres and the turnbull coefficient.* J. Chem. Phys., 115:2887, 2001.

[125] A. Cacciuto, S. Auer, and D. Frenkel, *Solid-liquid interfacial free energy of small colloidal hard-sphere crystals.* J. Chem. Phys., 119:7467, 2003.

[126] S. Auer. *Quantitative prediction of crystal nucleation rates for spherical colloids: a computational study.* PhD thesis, University of Amsterdam, 2002.

[127] R. J. Allen, C. Valeriani, and P. R. ten Wolde, *Forward flux sampling for rare event simulations.* J. Phys.: Cond. Matter, 21:463102, 2009.

[128] F. A. Escobedo, E. E. Borrero, and J. C. Araque, *Transition path sampling and forward flux sampling. applications to biological systems.* J. Phys.: Cond. Matter, 21:333101, 2009.

[129] M. Fasolo and P. Sollich, *Fractionation effects in phase equilibria of polydisperse hard-sphere colloids.* Phys. Rev. E, 70:041410, 2004.

[130] T. Schilling, H. J. Schöpe, M. Oettel, G. Opletal, and I. Snook, *Precursor-Mediated crystallization process in suspensions of hard spheres.* Phys. Rev. Letts., 105:025701, 2010.

[131] W. Lechner and C. Dellago, *Accurate determination of crystal structures based on averaged local bond order parameters.* J. Chem. Phys., 129:114707, 2008.

[132] S. Pronk and D. Frenkel, *Can stacking faults in hard-sphere crystals anneal out spontaneously?* J. Chem. Phys., 110:4589, 1999.

[133] H. Tanaka, T. Kawasaki, H. Shintani, and K. Watanabe, *Critical-like behaviour of glass-forming liquids.* Nat. Mater., 9:324–331, 2010.

[134] J. D. Weeks, D. Chandler, and H. C. Andersen, *Role of repulsive forces in determining the equilibrium structure of simple liquids.* J. Chem. Phys., 54:5237, 1971.

[135] T. Kawasaki and H. Tanaka, *Structural origin of dynamic heterogeneity in three-dimensional colloidal glass formers and its link to crystal nucleation.* J. Phys.: Condens. Matter, 22(23):232102, 2010.

[136] A. Ahmed and R. J. Sadus, *Phase diagram of the Weeks-Chandler-Andersen potential from very low to high temperatures and pressures.* Phys. Rev. E, 80(6):061101, 2009.

[137] R. L. Davidchack and B. B. Laird, *Simulation of the hard-sphere crystal-melt interface.* J. Chem. Phys., 108(22):9452, 1998.

[138] J. Israelachvili. *Intermolecular and Surface Forces.* Academic Press, London, 1992.

Summary

In this thesis we examined the phase behaviour and nucleation in colloidal systems. A colloidal system consists of gas bubbles, fluid droplets or solid particles of any shape suspended in another medium. The defining feature of a colloidal system relates to the motion of the suspended particles: they exhibit Brownian motion. The requirement that the particles be able to diffuse in a Brownian manner imposes a length scale on the particles. Specifically, in general for the particles to be able to display Brownian motion they have at least one dimension between 1 μm and 1nm.

One of the simplest, and frequently studied colloidal systems consists of polymethylmethacrylate (PMMA) or silica particles coated with a polymer. The interaction between these particles can be quite complex, consisting of van der Waals forces between the cores, a steric interaction between the polymer coatings which helps to prevent the particles from sticking together, and charges both on and in the particles and in the solvent. However, to a first approximation, such particles can frequently be modelled as hard spheres.

In this thesis we explored primarily the self-assembly of solid phases occurring in mixtures of hard spheres. The chapters of this thesis can be divided into three main categories, chapters which addressed the question of predicting possible crystal structures, chapters focused mainly on predicting the equilibrium phase behaviour for a given system, and chapters focused on the nucleation of colloidal particles.

One of the main difficulties in predicting the phase behaviour in colloidal, atomic and nanoparticle systems is in determining the stable phases, and in particular, the stable crystalline phases. In a recent nature materials review article, Scott Woodly and Richard Catlow argued that the "prediction of structure at the atomic level is one of the most fundamental challenges in condensed matter science". This statement also holds for colloidal and nanoparticle systems. To date, this remains a two-fold problem. To begin with we must identify possible stable crystal phases, and secondly we must determine whether these predicted candidate phases are themselves stable. Ideally we would be able to accomplish these tasks in a single step, but currently this is not possible.

With respect to predicting candidate crystal phases a number of techniques have been introduced which partially address this question, including, but by no means limited to, simulated annealing, basin hopping, and genetic algorithms. In general, these algorithms attempt to minimize the potential energy of the system. They make the underlying assumption that the system can be approximated by the zero temperature limit and hence the free energy can be approximated by the potential energy contribution. While this is often the case for atomic systems, for colloidal and nanoparticles systems the situation is frequently more complicated since the entropic contribution to the free energy is often significant. For instance, in hard-sphere mixtures, such as those examined in this thesis, the potential energy is always either 0 (corresponding to a configuration without overlapping particles) or infinity (corresponding to a configuration with an overlap between particles) and thus does not contribute to the free energy. As a result, the free energy consists of solely the entropic contribution. Hence, to predict the stable crystal structures, one needs to predict which crystal structures will have the largest entropy. However, predicting

which structures have to largest entropy is much more difficult since it is not possible to determine the entropy of a specific configuration, and more advanced techniques, such as Einstein integration, must be used to determine the entropic contribution to the free energy for a specific structure. Such techniques are computationally expensive, and as such are not practical to use in combination with minimization techniques. Hence, other approximations (or techniques) must be used to predict candidate crystal structures in such systems.

One such approximation relies on a "cell theory"-like picture of a crystal. In such a picture, the entropy is associated with the free volume per particle in the associated cell. Following this logic, crystal structures which pack well are expected to have large free volumes per particle and thus have large entropic contributions to the free energy. The argument clearly holds in the case of monodisperse hard spheres. As argued by Kepler approximately 400 years ago, the closest packed arrangement of monodisperse hard spheres corresponds to face-centered-cubic (FCC), hexagonal-close-packed (HCP), and random-hexagonal-close-packed crystal structures (rHCP). All of these have a packing fraction of 0.74, and the free-energy differences are very small (on the order of $0.001K_BT$ per particle). Most importantly, the crystal phase which is stable for monodisperse hard spheres is FCC and hence one of the best packed crystal structures corresponds to the most stable. Keeping this in mind, in Chapter 2 we attempted to predict the best packed crystal structures for binary hard-sphere mixtures. In particular we examined systems where the size ratio between the diameters of the small and large spheres were 0.4 to 0.8. To do this we used a genetic algorithm. In this work, we found a number of structures which are frequently discussed in the context of binary crystal structures, and in particular, binary hard-sphere mixtures, including structures with atomic analogues NaCl, CsCl, and AlB_2. Additionally, we found a number of less well studied crystal structures.

In Chapter 3, we attempted to predict the phase diagrams for hard-sphere mixtures with size ratios between 0.74 and 0.85. To do this we calculated the Gibbs free energy of candidate structures and used common tangent constructions to determine the phase coexistences. For the candidate crystal phases, we used the best packed structures from Chapter 2. Additionally, we examined the stability of a binary fluid, monodisperse FCC phases of the large and small spheres and the binary crystal Laves phases. (Cartoons of these phases are shown in Chapter 2). The Laves phases had previously been examined in the context of binary hard-sphere mixtures and we were interested to see how the best-packed structures compared with the Laves phases. Unexpectedly, the less well packed Laves phases were found to be more stable than the best packed structures, indicating that the "cell-theory"-like picture of the entropic contribution to the free energy was insufficient to explain the phase diagram in this case.

In Chapter 4, we introduced a new method for predicting candidate crystal structures which circumvents the cell-theory like assumption associated with best-packing arguments. The new method is very simple and consists simply of Monte Carlo simulations in very small simulation boxes (2-12 particles) where the box shape is allowed to fluctuate. Simulations are started in the fluid phase, and the pressure is slowly increased until the system crosses the fluid-solid phase boundary. In the case of binary hard-sphere mixtures, we found that this method correctly predicted the Laves phases as the candidate crystal structures. Thus, this method seems to correctly predict entropy stabilized crystal struc-

tures. Additionally, in Chapter 4, we applied this method to a wide variety of systems showing that it also works in the case of attractive interactions, anisotropic particles, and long-range interactions. As such, we expect this method to be widely applicable in the prediction of candidate crystal structures for colloidal systems.

In Chapter 5, we examined the phase behaviour of binary hard sphere mixtures of size ratios 0.3-0.42. This system had been examined in the past, and the phase diagram had been thought to contain only a binary fluid phase, phase separated FCC crystals of the large and small spheres, and a crystal structure analogous to NaCl. However, initial constant pressure Monte Carlo simulations appeared to indicate the existence of another phase, in particular, an interstitial solid solution (ISS). The ISS phase consists of an FCC crystal of the large particles with some of the octahedral holes filled by smaller particles. Using full free-energy calculations in combination with common tangent constructions, we showed that there is a large part of the phase diagram where the ISS phase is stable and that the filling fraction can be tuned from 0 to 100%. Additionally, we examined the diffusive properties of the small particles in the ISS for size ratio 0.3. In contrast to most systems, we found a region where the diffusion increases as a function of the packing fraction.

In Chapter 6, we re-visited a rather old problem in colloidal systems, namely the nucleation rates in monodisperse hard spheres. This problem has been examined previously both experimentally (using light scattering experiments) as well as with umbrella sampling simulations. The main interest in the problem stems from the large disagreement between the simulation and experimental nucleation rates. For low supersaturations (corresponding to low volume fractions), this difference is as large as 12 orders of magnitude. The origin of this difference, however, has never been identified and remains of interest as it indicates a difficulty to match experimental and simulation nucleation rates in, arguably, the simplest colloidal model system. In Chapter 6, we re-examined this problem using a number of different simulation techniques, including umbrella sampling (US), forward flux sampling (FFS), and molecular dynamics (MD) (where possible). In general, MD simulations would be expected to be "exact", however, due to simulation time constraints they can only be used for rather large supersaturations. Umbrella sampling and FFS, however, are techniques designed to study rare events and thus applicable at lower supersaturations. Nonetheless, the two techniques are quite different: US uses a biasing potential to measure the equilibrium distribution of clusters while FFS (like MD) examines the steady state distribution. Despite these differences between simulation methods, we found that all the simulated nucleation rates agreed and that the difference between the simulated and experimental nucleation rates at low supersaturation remains.

Our use of FFS in colloidal crystal nucleation in Chapter 6 was one of the first applications of FFS to such systems. As discussed in Chapter 6, in our simulations we encountered a number of difficulties which prevented us from applying the technique directly, and a few modifications were necessary. In particular, we found that the size of a growing cluster measured by our simulations contained both short-time fluctuations and long time growth. To study the effect of such short-time fluctuations on the FFS method, in Chapter 7 we introduced a one dimensional toy model and examined the effect of measurement error on the toy model. We found FFS to be robust to such measurement error indicating that is should be effective in the study of crystal nucleation in colloidal hard

spheres.

Finally, in Chapter 8, we calculated the phase diagram and examined crystal nucleation of the Weeks-Chandler-Andersen (WCA) model with $\beta\epsilon = 40$. The WCA potential is based on the repulsive part of the Lennard Jones model, and while it is slightly softer than the hard-sphere potential, it is frequently used to approximate hard spheres. One recent study indicated that the crystal nucleation rates predicted using BD simulations of the WCA potential with $\beta\epsilon = 40$ were in agreement with the experimental hard-sphere nucleation rates. This contradicted with our work in Chapter 6, and as such, we re-examined this system using BD, US and FFS. We found that our predicted nucleation rates were all in agreement. Additionally, when scaled such that the freezing point matched that of hard spheres, the nucleation rates were in agreement with our predictions from Chapter 6. Hence, the softness did not appear to have a significant effect on the nucleation rates. Strangely, our BD results differed significantly from those of the previous study. When this thesis was written this difference we still not understood.

Samenvatting

In dit proefschrift bestuderen we het fasegedrag van colloïden en de nucleatie van colloïdale kristallen. Colloïdale oplossingen bestaan uit kleine deeltjes, die zich zowel in een gas, vloeistof, of vaste fase kunnen bevinden, gedispergeerd in een ander medium. De belangrijkste eigenschap van een colloïdaal systeem heeft te maken met de beweging van de deeltjes: ze vertonen Brownse beweging. Om door Brownse bewegingen meetbare diffusie door het systeem te ondergaan, moeten de deeltjes ten minste een grote tussen ongeveer 1 nanometer en 1 micrometer hebben.

Een van de eenvoudigste en meest bestudeerde colloïdale systemen bestaat uit bolvormige deeltjes van polymethylmethacrylaat (PMMA) of silica, bedekt met polymeren. De interacties tussen deze deeltjes kunnen vrij ingewikkeld zijn. Ze worden veroorzaakt door de vanderwaalskrachten tussen de deeltjes zelf, een sterische interactie tussen de coatings die voorkomt dat de deeltjes aan elkaar plakken en lading zowel op de deeltjes als in het oplosmiddel. Toch wordt het gedrag van deze deeltjes als eerste benadering goed beschreven door een model van harde bollen.

In dit proefschrift hebben we vooral gekeken naar de kristalstructuren die worden gevormd door zelforganisatie in mengels van harde bollen. De hoofdstukken kunnen verdeeld worden in drie categorieën: hoofdstukken over het voorspellen van mogelijke kristalstructuren, hoofdstukken waarin het fasegedrag van systemen wordt voorspeld, en hoofdstukken over de nucleatie van colloïdale deeltjes.

Bij het voorspellen van het fasegedrag van colloïdale en atomaire systemen is een van de moeilijkste factoren het voorspellen van de stabiele kristalstructuren. In een recent review article schreven Woodley and Catlow dat "prediction of structure at the atomic level is one of the most fundamental challenges in condensed matter science." Dit is ook van toepassing op colloïdale systemen. Dit probleem bestaat uit twee delen: ten eerste het vinden van mogelijk stabiele kristalstructuren, en ten tweede het vaststellen of deze structuren ook daadwerkelijk stabiel zijn.

Voor het voorspellen van mogelijke kristalstructuren zijn een aantal technieken geïntroduceerd, waaronder simulated annealing, basin hopping en genetic algorithms. In de meeste gevallen worden deze algoritmes gebruikt om de potentiële energie van het systeem te minimaliseren. Hierbij wordt de aanname gemaakt dat de kristalstructuur overeen komt met de structuur die gevormd wordt in de limiet van lage temperaturen, waar de vrije energie benaderd kan worden door alleen de potentiële energie. Hoewel dit vaak werkt voor atomaire systemen, is de situatie in colloïdale systemen ingewikkelder, omdat de entropische bijdrage aan de vrije energie daar ook belangrijk is. Voor mengsels van harde bollen, zoals bestudeerd in dit proefschrift, is de potentiële energie bijvoorbeeld altijd gelijk aan nul (voor configuraties zonder overlappende deeltjes) of oneindig (voor configuraties waarin ten minste twee deeltjes overlappen), zodat deze niet bijdraagt aan de vrije energie. Om de stabiele kristalstructuren te voorspellen moeten we dus de kristalstructuren vinden met de grootste entropie. Voorspellen welke structuren de grootste entropie hebben is echter veel moeilijker, omdat het niet mogelijk is om de entropie van een specifieke configuratie te berekenen. Hoewel er technieken bestaan, zoals Einstein integratie,

om de entropische bijdrage aan de vrije energie in een systeem te berekenen, kosten deze vaak erg veel rekentijd, en zijn daardoor niet geschikt voor gebruik in combinatie met minimalisatietechnieken. Daardoor zijn andere benadering (of technieken) noodzakelijk om mogelijke kristalstructuren in zulke systemen te voorspellen.

Een van de mogelijke benaderingen is gebaseerd op de beschrijving van een kristal binnen de cell theory. In dit beeld is de entropie geassocieerd met het beschikbare volume per deeltje in zijn Wigner-Seitz cel. Volgens deze logica verwachten we dat kristalstructuren met een dichte maximale pakking per deeltje een groot beschikbaar volume hebben bij lagere dichtheden. Dit is zeker waar voor monodisperse harde bollen. Zoals Kepler 400 jaar geleden al voorstelde, komt de ordening van monodisperse bollen met de hoogst mogelijke dichtheid overeen met de face-centered-cubic (FCC), hexagonal-close-packed (HCP) en random-hexagonal-close-packed (rHCP) structuren. Al deze structuren hebben dezelfde maximale volumefractie: 74%, en de verschillen in vrije energie zijn erg klein (in de orde van 0.001 k_BT per deeltje). De kristalstructuur die stabiel is voor monodisperse harde bollen is FCC, en komt dus overeen met een van de structuren met de grootste maximale volumefractie. Met dit idee in gedachten probeerden we in hoofdstuk 2 de structuren met maximale pakking te voorspellen voor binaire mengsels van harde bollen. We keken daarbij naar systemen waarin de verhouding tussen de diameters van de kleine en grote bollen lag tussen de 0.4 en 0.8, en maakten gebruik van genetische algoritmes. We vonden een aantal structuren die vaak voorkomen in studies van binaire kristalstructuren, waaronder de colloïdale equivalenten van NaCl, CsCl en AlB_2. Daarnaast vonden we een aantal minder bestudeerde kristalstructuren.

In hoofdstuk 3 constueerden we fasediagrammen voor mengsels van harde bollen met grootteverhoudingen tussen de 0.74 en 0.85. Hiervoor berekenden we de Gibbs vrije energie van kandidaatfasen en maakten gebruik van 'common tangent' constructies om de fasecoëxistenties te berekenen. Als kandidaten voor de kristalstructuren gebruikten we de dichtstgepakte kristalstructuren uit hoofdstuk 2. Daarnaast bekeken we de stabiliteit van een binaire vloeistof, monodisperse FCC-kristallen van de grote en kleine bollen en de binaire Laves kristalstructuren (plaatjes van deze structuren zijn te vinden in hoofdstuk 2). Er was al eerder bekend dat de Laves-structuren stabiel zijn voor grootteverhouding 0.8, maar veel van de structuren uit hoofdstuk 2 waren niet meegenomen in dit onderzoek. Verrassend genoeg bleken de minder dicht pakkende Laves-structuren stabieler dan de structuren met de maximale volumefractie. Dit laat zien dat de meest dichte kristalstructuur niet zondermeer de hoogste entropie heeft.

In hoofdstuk 4 introduceerden we een nieuwe methode om kandidaatstructuren te voorspellen, waarbij geen gebruik wordt gemaakt van de aanname dat de entropie gerelateerd is aan de maximale volumefractie. De nieuwe methode is erg makkelijk en bestaat uit Monte Carlo simulaties van kleine systemen (2-12 deeltjes), waarbij de vorm van het gesimuleerde volume kan fluctueren. De simulaties beginnen als een vloeistof en de druk neemt langzaam toe tot het systeem kristalliseert. In het geval van mengsels van harde bollen vonden we inderdaad de stabiele Laves-structuren. De methode lijkt dus ook in staat te zijn structuren te voorspellen die gestabiliseerd worden door entropie. In hoofdstuk 4 passen we deze methode ook toe op een aantal zeer verschillende systemen, en laten zien dat ze ook werkt in systemen waarin de deeltjes elkaar aantrekken, de interacties anisotroop zijn, of de interacties over lange afstanden werken. We verwachten dus

dat deze methode ruim toepasbaar is voor het voorspellen van kandidaatstructuren in colloïdale systemen.

In hoofdstuk 5 bekeken we het fasegedrag van binaire mengsels van harde bollen met grootteverhoudingen tussen de 0.3 en 0.42. Deze systemen waren al eerder bestudeerd, en het fasediagram leek enkel te bestaan uit een binaire vloeistof, FCC kristallen van grote of kleine bollen, en een kristalstructuur analoog aan NaCl. Monte Carlo simulaties bij constante druk wezen echter uit dat er nog een fase stabiel zou kunnen zijn, een interstitial solid solution (ISS). De ISS fase bestaat uit een FCC kristal van grote deeltjes, waarin een gedeelte van de gaten, die met de vorm van een octaëder, in het kristal gevuld is met kleine deeltjes. Met behulp van volledige vrije energie berekeningen in combinatie met common tangent constructies toonden we aan dat de ISS fase stabiel is in een groot gedeelte van het fasediagram, waarbij het percentage van de gaten in het kristal dat gevuld is varieert van 0 tot 100%. Daarnaast bekeken we de diffusie van kleine deeltjes door de ISS bij grootteverhouding 0.3. In tegenstelling tot de meeste andere systemen vonden we hier een gebied waar de diffusie toeneemt als functie van de volumefractie.

In hoofdstukken 3 en 5 hebben we de thermodynamische stabiliteit van verschillende kristalstructuren in evenwicht aangetoond, maar om kristallen ook experimenteel waar te nemen, moet het systeem ook in staat zijn de kristalstructuur te vormen. Een van de belangrijkste manieren waarop kristallen worden gevormed is via nucleatie. Bij de nucleatie van een kristal ontstaat een nucleus in een oververzadigde vloeistof door thermische fluctuaties. Een van de interessantste vragen over dit systeem is hoe lang het duurt voordat een nucleus wordt gevormd die groot genoeg is om uit te groeien tot een kristal. Deze tijd wordt gegeven door de nucleation rate. Voor harde bollen, het eenvoudigste modelsysteem voor colloïden, is de nucleation rate al eerder bestudeerd, zowel in experimenten (met behulp van lichtverstrooiing) als in simulaties. Helaas blijkt dat zelfs voor harde bollen de nucleation rates voorspeld door simulaties en die gemeten in experimenten ver uit elkaar liggen: de verschillen liggen in de orde van 10^{12}. De oorzaak van deze verschillen is niet bekend. In hoofdstuk 6 bekeken we dit probleem met behulp van verschillende simulatietechnieken, waaronder umbrella sampling (US), forward flux sampling (FFS), en molecular dynamics (MD). We verwachten dat de resultaten uit MD simulaties exact zijn, maar omdat deze simulaties erg lang kunnen duren kan deze techniek alleen gebruikt worden bij vrij hoge oververzadiging. Umbrella sampling en FFS zijn echter ontwikkeld om rare events te bestuderen, en zijn dus ook toepasbaar bij lage oververzadiging. De technieken verschillen sterk: US maakt gebruik van een biasing potential om de evenwichtsverdeling van clusters te meten, terwijl met FFS en MD de steady state verdeling wordt bekeken. Ondanks deze verschillen zagen we dat de resultaten van alle simulatiemethoden met elkaar overeenkomen, en dat de verschillen tussen de simulaties en experimenten blijven bestaan.

Onze toepassing van FFS op nucleatie in hoofdstuk 6 was een van de eerste keren dat deze techniek werd toegepast op de nucleatie van colloïdale kristallen. Zoals beschreven in hoofdstuk 6 ondervonden we een aantal problemen in onze simulaties, die ervoor zorgden dat een aantal wijzigingen in de methode nodig waren voor deze toegepast kon worden. We zagen dat de grootte van een groeiende cluster wordt beïnvloed door fluctuaties op zowel korte als lange tijdsschalen. Om het effect van de fluctuaties op korte tijdsschalen op de simulaties te bepalen, gebruikten we in hoofdstuk 7 een eenvoudig eendimensionaal

model, en bekeken daarin de effecten van een meetfout op de gemeten nucleation rate. Het effect van een dergelijke meetfout op FFS bleek klein te zijn. Dit suggereert dat de methode goed toepasbaar zou moeten zijn voor het meten van de nucleation rate in colloïdale harde bollen.

Uiteindelijk berekenden we in hoofdstuk 8 het fasediagram van het Weeks-Chandler-Andersen (WCA) model met $\beta\epsilon = 40$, en bestudeerden we de nucleatie van een kristal in hetzelfde systeem. De WCA potentiaal is gebaseerd op het repulsieve deel van het Lennard-Jones model, en is zachter dan de potentiaal voor harde bollen. Toch wordt dit model regelmatig gebruikt om harde bollen te benaderen. Een recent onderzoek liet zien dat de nucleation rates in dit model, gemeten met behulp van Brownian Dynamics (BD), overeenkwamen met de experimenteel gemeten nucleation rates voor harde bollen. Aangezien dit in tegenspraak is met onze resultaten uit hoofdstuk 6, onderzochten we dit systeem nogmaals met zowel BD, US als FFS. Onze nucleation rates kwamen overeen voor alle drie de methoden. Daarnaast konden de resultaten in overeenstemming gebracht worden met de resultaten voor harde bollen uit hoofdstuk 6, door de dichtheden zo te schalen dat de vriespunten van de twee systemen overeen komen. De zachtere interacties lijken dus geen sterke invloed te hebben op de nucleatie. Vreemd genoeg verschilden onze BD resultaten sterk van die uit het eerdere onderzoek. Op het moment dat dit proefschrift werd geschreven hadden we nog geen verklaring voor dit verschil.

Dankwoord

It's been almost four years since I first arrived in the Netherlands and took a train from the airport to my new home in Utrecht. I'll never forget that train ride, sitting on the train and watching the strange fields go by, trying to make some sense out of the vast number of huge ditches which divided the farm land. Arriving in Utrecht, stumbling into the streets after 14 hours of travelling, and trying not to get run over by a bike I made my way to a B&B where I stayed for my first two days in this new city, this new country. Wondering around the Utrecht, I immediately fell in love with it, even in the dreary month of February. Utrecht is truly a beautiful city.

However, as amazing as a city may be, for me it is not the place that's most important, but the people. And in this way, it's hard to have imagined making a better choice. The Soft Matter Group in Utrecht has been an amazing group to work in. One of the main reasons has been my supervisor, Marjolein Dijkstra, who is always interested in what we are working on, and whose office door was always open. Marjolein, I would like to thank you very much for accepting me as a PhD student and giving me the opportunity to work in this group, and for all your help over the last four years. I could not have asked for a better supervisor.

I would like to thank Alfons van Blaaderen, Arnout Imof and Rene van Roij for many useful discussions, and feedback during the whole of my PhD. I would also like to thank Daniël Vanmaekelbergh and Wiel Evers for their interesting discussions and collaborations on binary nanoparticle superlattices.

One of the projects briefly mentioned in Chapter 4 of my thesis was the crystal structure appearing in patchy particles. Although this project may not have gone exactly as we hoped, I learned a lot and enjoyed it. Thanks Emanuela, for introducing me to the world of patchy particles! :D

A special thanks also goes out to my office mates over the years: Frank, Eduardo, Alessandro, Ran and Emanuela. I will miss the lively office discussions. The addition of the chalk board during the last year has found good use and I've thoroughly enjoyed the inter-office debates!

Michiel, and Matthieu, thanks for all your help over the years both for research as well as keeping my computer going! Michiel, a special thanks for allowing me to use your opengl colloidal graphics program - it's the best I've seen yet! The vast majority of snapshots shown in this thesis were produced with it.

I would acknowledge the great group of collogues I've had to work with over the last four years. I won't try and name you all here for fear I would forget someone, but my time in Utrecht would not have been the same without you all. I've learned a lot chatting with many of you, through the Friday work discussions, not to mention the coffee breaks! I must admit, I don't think I am likely to forget the wide variety of subjects we covered at those coffee breaks! :P

Living in a new country frequently comes with an added challenge, the language of that country. I arrived four years ago not knowing a single dutch word. I would like to thank the many people who have helped me *attempt* to learn the language. In particular,

Esther, Peter (although some more sympathy at the beginning may have been nice! :P), Michiel, Frank, and Johan - thanks for all your help! Also, a special thanks to the group who I went to Sweden with (and in particular, Anke and Michiel) who helped me to learn the correct pronunciation of “water”. What would my life be without the dutch “aa”!

Speaking of Sweden, group “outings” and trips with some of the group members have been a highlight during my time in Utrecht. The trip to Sweden was great! Thanks Peter and Esther, for organizing the Wadlopen group trip and the many skating trips over the last few years. Also, a big thanks to Teun, Niels and Bas for a fabulous road trip to Spain (and for getting me there in one piece!).

Sports have always been a big part of my life, and I think giving up ice hockey was one of the biggest sacrifices I made in moving to the Netherlands. Hence, a big thanks to all those who helped me fill my time with squash and climbing instead. In particular, to Peter, Teun, Matthieu, Anke, and John Kelly: Thanks!

In order to get a PhD, one first needs to obtain a Masters.... I completed my Masters degree in Hamilton, Ontario. I enjoyed thoroughly my time there, and it was mostly due to the wonderful people I worked and socialized with. Here’s a huge thanks to the old MAC crew, Marie-Josee, Nadi, Robi, Muoi, Soko, Rastko, Paulo, Pamela, Marie-Angela, Jose, Kiri, and many others. Hamilton would not have been Hamilton without you!

I’d also like to thank my “paranimfs”, Marie Josee and Emanuela. Thank you for coming to Utrecht to help me with my defence and to celebrate my time here.

On a more serious note, I think we all meet people in our lives who cannot help but change us. One of my roommates during my undergrad was one such person. In fact, I think she changed (for the better) pretty much everyone who had the pleasure of knowing her. Although blind, there was nothing she was not willing to try - including dancing, horseback riding and parachuting! She died last year in an accident, only 31. Holly, you demonstrated with every day of your life that anything was possible if you were willing to work at it and try. Thanks for all the fun we had and for inspiring all around you with your love of life.

Finally, a very special thanks goes out to my family, and particularly my parents. To my mother, I wish you could have been around to read this, but you will always be in my heart. And, to my father, "Merci".

List of publications

This thesis is based on the following publications

- L. Filion, M. Hermes, R. Ni, E.C.M. Vermolen, A. van Blaaderen, and M. Dijkstra, *Self-assembly of a colloidal interstitial solid solution with a tunable sublattice doping*, submitted. (Chapter 5)
- L. Filion, M. Hermes, R. Ni, M. Dijkstra, *Crystal Nucleation of hard spheres using molecular dynamics, umbrella sampling, and forward flux sampling: A comparison of simulation techniques*, J. Chem. Phys. **133**, 244115 (2010) (Chapter 6 and 7)
- L. Filion, M. Marechal, B. van Oorschot, D. Pelt, F. Smallenburg, and M. Dijkstra, *Efficient Method for Predicting Crystal Structures at Finite Temperature: Variable Box Shape Simulations*, Phys. Rev. Letts. **103**, 188302 (2009). (Chapter 4)
- L. Filion and M. Dijkstra, *Prediction of binary hard-sphere crystal structures*, Phys. Rev. E **79**, 046714 (2009). (Chapter 2)
- A. P. Hynninen, L. Filion, and M. Dijkstra, *Stability of LS and LS_2 crystal structures in binary mixtures of hard and charged spheres*, J. Chem. Phys. **131**, 064902 (2009). (Chapter 3)

Other publications by the author:

- R. Ni, F. Smallenburg, **L. Filion**, M. Dijkstra, *Crystal Nucleation in binary hard-sphere mixtures: The effect of order parameter on the cluster composition*, accepted to Mol. Phys.
- W.H. Evers, B. De Nijs, **L. Filion**, S. Castillo, M. Dijkstra, and D. Vanmaekelbergh, *Entropy-driven formation of binary semiconductor-nanocrystal superlattices*, Nanoletts. **10** 4235 (2010) .
- E. C. M. Vermolen, A. Kuijk, **L. Filion**, M. Hermes, J. H. J. Thijssen, M. Dijkstra, and A. van Blaaderen, *Fabrication of large binary colloidal crystals with a NaCl structure*, P. Natl. Acad. Sci. USA **106**, 16063 (2009)
- W. H. Evers, H. Friedrich, **L. Filion**, M. Dijkstra, and D. Vanmaekelbergh, *Observation of a ternary nanocrystal superlattice and its structural characterization by electron tomography*, Angew. Chem. Int. Edit. **48**, 9655-9657 (2009)
- D.A. Pink, C.B. Hanna, B.E. Quinn, V. Levadny, G.L. Ryan, **L. Filion**, and A.T. Paulsond *Modelling electrostatic interactions in complex soft systems*, Food Res. Int. **39** 1031-1045 (2006)
- M. J. Lewis, B. D. Gaulin, **L. Filion**, C. Kallin, A. J. Berlinsky, H. A. Dabkowska, Y. Qiu, and J. R. D. Copley *Ordering and spin waves in $NaNiOi_2$: A stacked quantum ferromagnet*, Phys. Rev. B **72**, 014408 (2005)

- R. J. van den Hoogen and **L. Filion** *Stability analysis of multiple scalar field cosmologies with matter*, Class. Quantum Grav. **17**, 1815 (2000)